# Course Reader: Computational Modeling in the Cardiovascular System

Alison L. Marsden
Bioengineering and Pediatrics
Institute for Computational and Mathematical Engineering
Stanford University

Fall 2024

# Contents

# Chapter 1

# Introduction to the Cardiovascular System

## 1.1 The Function of the Cardiovascular System

The circulatory system is the primary means of transport for oxygen, nutrients, enzymes, hormones, and heat in organisms. These transport processes inherently link the respiratory, digestive, endocrine, excretory and nervous systems of the body, from cellular to organ scales. Far from a static system, the cardiovascular system continually changes and adapts to meet the demands of the organism in healthy and diseased states. Hemodynamic (blood fluid mechanic) factors including flow rate, shear stress, and pressure forces provide the stimuli for many acute and chronic biologic adaptations. Hemodynamic, physiological, and mechanobiological processes can be modeled over a range of scales using mathematical and computational tools to assess their impact on disease diagnosis and progression, and clinical treatment planning.

The key elements of all closed circulatory systems are a circulating fluid (blood), a pumping mechanism (heart), a distribution system (arteries), an exchange system (capillaries), and a collection system (veins). Note that some animals, notably insects, and many mollusks, eject a blood-like fluid

directly into their body cavities. This open circulatory system, operating under low pressures and small velocities, is a relatively inefficient transport system, which poses great difficulties for the organism in achieving a differential distribution of blood flow to various organs and tissues [34]. In the chapters to follow, we focus our attention on mammalian circulatory systems. The interested reader is referred to the books by [34] and [33] for further discussion of circulatory systems in other animals.

Blood is a suspension of cells in plasma. The concentration of cells, termed hematocrit, is approximately 50% by volume, but may vary in diseased states or with age. We can distinguish three major types of cells on the basis of their function in the circulation: erythrocytes, leukocytes, and thrombocytes. Erythrocytes or red blood cells are the most abundant cells in the blood stream (and the body) and are the primary transport vessels for oxygen and carbon dioxide. It is estimated that of the approximately 100 trillion cells in the body, fully one-fourth are erythrocytes! Mammalian erythrocytes are disk shaped (due to the absence of a nucleus) with a diameter of approximately 8 $\mu$m and a thickness of 2 $\mu$m. Leukocytes or white blood cells represent less than 1% of blood cells, but have a critical role in producing antibodies and identifying and disposing of foreign substances. Monocytes and lymphocytes are two particular types of leukocytes that have been implicated in the early stages of atherosclerosis and support the current view of atherosclerosis as a chronic inflammatory disease [57]. The third major category of blood cells, thrombocytes or platelets, represents approximately 5% of blood cells. Thrombocytes interact with the protein fibrinogen to form fibrin, a mesh that traps cells to aid in blood clotting and healing processes. Finally, the plasma consists of approximately 90% water, 8% plasma proteins, 1% inorganic substances, and 1% emulsified fat. Blood plasma comprises approximately 20% of the entire extracellular fluid of the body.

The heart provides the driving force to propel blood through the systemic and pulmonary arteries, and receives the venous return from the systemic and pulmonary circulations. In the normal heart, during the diastolic phase of the cardiac cycle, blood entering the atria flows into the ventricles as the ventricles relax and pressures fall below atrial pressures. Blood flowing from the right atria passes through the tricuspid valve into the right ventricle, while blood travels from the left atria to the left ventricle through the mitral valve. During the systolic phase of the cardiac cycle, the rising pressure

in the contracting left ventricle exceeds aortic pressure and blood is ejected from the left ventricle through the aortic valve into the ascending aorta. Simultaneously, once the rising right ventricular pressure exceeds the main pulmonary artery pressure, blood flows through the pulmonary valve into the pulmonary arteries. Blood fills the right atria from the superior and inferior vena cava and the left atria from the pulmonary veins as the blood exiting the atria during diastole reduces atrial pressure relative to the venous filling pressure. The cardiac cycle, once complete, repeats itself again as it will another 35 million times each year for the average adult.

## 1.2 Importance of Biomechanics in Cardiovascular Disease

Local hemodynamic factors often act as stimuli to trigger changes in cardiac output and downstream vascular resistance that are essential in responding to acute changes in organ demand. For example, during exercise, the blood flow rate established to meet the metabolic demands of resting conditions is insufficient for the active muscles. These muscles release metabolic products that cause the local vessels to dilate resulting in a decrease in the local vascular resistance and an increase in muscle blood flow by shunting blood from other tissues and organs. The blood vessels upstream of those in the working muscle in turn dilate because of increased flow. This mechanism is hypothesized to be modulated by increased shear stress triggering the release of nitric oxide from the endothelial cells lining the inner surface of blood vessels experiencing increased flow. Ultimately, the dilation of the vascular bed supplying the working muscles reduces the overall vascular resistance felt by the heart and would reduce systemic blood pressure if the cardiac output remained constant. Instead, baroreceptors, specialized pressure-sensing cells in the aorta and carotid arteries, provide feedback to the nervous system to increase heart rate and cardiac output to maintain blood pressure. While blood flow rate can increase several-fold during exercise conditions, mean blood pressure typically changes by less than 10–20%. The hemodynamic variables of flow rate, shear stress, and blood pressure all play a role in the response of the cardiovascular system to acute changes in end-organ demand. Quantifying these variables under a range of physiologic conditions is one of

the important applications of computational methods applied to model blood flow.

The cardiovascular system also adapts to long-term anatomic and physiologic changes of the organism as occurs during growth, aging, injury, increased or decreased physical activity levels, and the onset of disease. Again, hemodynamic conditions play important roles in vascular adaptation in health and disease. Changes in blood velocity and pressure fields, sensed at a cellular level, initiate a cascade of biochemical signals leading to hierarchical reorganization across molecular, cellular, tissue, and system scales. For example, blood vessels enlarge in response to chronic increases in blood flow through a mechanism thought to be modulated by increased shear stress acting on the endothelial cells[32, 74]. In contrast to vascular enlargement in response to increased flow, blood vessels reduce in caliber in response to reductions in blood flow [21]. In addition to shear-modulated changes in the diameter of blood vessels due to changes in blood flow, the walls of blood vessels get thinner as a result of decreased pressure, and thicken in response to increased pressure through a mechanism hypothesized to be modulated by changes in tensile stress[46]. These adaptive processes are part of a growing body of research on vascular growth and remodeling.[27, 65]

Acquired cardiovascular disease became the leading cause of death in the industrialized world in the early twentieth century and contributes to roughly a third of global deaths. The most predominant form of acquired cardiovascular disease, atherosclerosis, results from the chronic buildup of fatty material in the inner layer of the arteries supplying the heart, brain, kidneys, digestive system, and lower extremities. Interestingly, the upper extremity vessels are typically spared of atherosclerosis. Risk factors for atherosclerosis including smoking, high cholesterol diet, physical inactivity, and obesity affect all the arteries of the body, but notably, the disease is localized at branches and bends of the arterial tree. The observation that atherosclerosis occurs only in localized regions of the body has led to the hypothesis that hemodynamic factors play a critical role in its development[8, 20, 73]. This has motivated the application of experimental and computational methods to quantify hemodynamics and vessel wall biomechanics in human arteries.

In contrast to occlusive diseases such as atherosclerosis that results in vessel narrowing, aneurysmal disease results in vessel enlargement and in some

cases rupture. As in the case of atherosclerosis, despite risk factors that are diffuse throughout the body, aneurysmal disease is highly localized and occurs predominantly in the aorta, and the iliac, popliteal, carotid, and cerebral arteries. Unlike atherosclerosis, aneurysms are uncommon in the coronary arteries. The localization of aneurysmal disease is hypothesized to be influenced by hemodynamic conditions including flow stagnation and pressure wave amplification. For example, one of the most common sites of aneurysmal disease, the infrarenal abdominal aorta, is a location where blood flow is particularly complex and recirculating as a result of the multiple branches that deliver blood to the organs in the abdomen[31, 30, 63, 62]. The resulting flow stagnation in the infrarenal abdominal aorta may enhance inflammatory processes hypothesized to contribute to the degradation of the vessel wall. In addition, because of the reduction of cross-sectional area and progressive stiffening of the aorta from the heart to the pelvis, as well as pressure reflections from downstream vessels, the pressure pulse increases in magnitude and contributes to a greater load on the wall of the abdominal aorta. Once again, the quantification of blood flow velocity and pressure fields may contribute to investigations into the pathogenesis of aneurysmal disease.

Congenital cardiovascular diseases arise from structural abnormalities of the heart and blood vessels including septal defects (holes between the atria or ventricles), obstructions of the valves of the heart or major arteries leaving the heart, transposition of the major arteries exiting the heart, and inadequate development of the right or left ventricles. In some cases, multiple defects are present or one defect can precipitate another, as occurs when obstruction of the tricuspid valve (between the right atrium and ventricle) interferes with the normal development of the right ventricle. As in the case of the normal adaptation of blood vessels in response to changes in shear or tensile stress, hemodynamic factors play an important role in the development and progression of congenital cardiovascular disease. Further, since reconstructive surgeries or catheter-based interventions used to repair congenital malformations alter the hemodynamic conditions, methods to model blood flow, coupled to cardiovascular physiology, have increasing application in clinical decision-making in pediatric cardiology and surgery.

Finally, in clinical medicine, the quantification of blood flow velocity and pressure fields is becoming increasingly important in the diagnosis, treatment planning, and subsequent management of patients with congenital and

acquired cardiovascular diseases. Risk stratification may be enabled by using computational modeling to augment clinical imaging studies, providing hemodynamic data that may be otherwise unattainable. Medical, interventional, and surgical therapies used to increase or restore blood flow to compromised organs and tissues or isolate aneurysmal regions from pressure forces may benefit from quantitative data provided by computational methods.

## 1.3 Perspective on Cardiovascular Modeling

Computational methods have been widely applied to the quantification of hemodynamic and biomechanical factors in relation to the genesis, progression, and clinical consequences of congenital and acquired cardiovascular disease. Cardiovascular blood flow simulations offer a means to augment current medical imaging modalities and physician experience to potentially improve treatment outcomes for a range of cardiovascular diseases. Perhaps more importantly, simulations offer predictive capabilities to test new surgical concepts, medical devices, and post-operative surgical outcomes. Recent advances in computing technology and efficient algorithms have led to increasingly realistic and accurate simulations, which now capture physiologic levels of blood pressure, detailed anatomy, feedback mechanisms of the circulatory system, and vessel wall deformations.

Early work in fluid mechanics of blood flow produced analytical solutions of the Navier-Stokes equations for pulsatile flow in rigid and elastic tubes.[71] These solutions were derived by J.R. Womersley in the 1950s and are now widely used, in particular as boundary conditions for large-scale flow simulations. Womersley theory provides analytical solutions for pulsatile flow in rigid and elastic tubes, revealing interesting oscillatory flow behavior at the vessel wall, and providing a basis for describing wave propagation phenomena.

Following this, starting in the 1960s, lumped parameter (zero-dimensional) models of the circulatory system were developed by analogy to electrical circuits.[70, 69] These models have the advantage that they are governed by ordinary differential equations and can be readily solved in near real time on a desktop computer. While they do not provide spatial information, they can

be quite complex, providing a surprisingly realistic representation of circulatory and cardiac dynamics. A useful description of the relationship between ventricular pressure and flow during the cardiac cycle is the pressure–volume loop. Clearly, changes in left ventricular volume during ejection directly correspond to the aortic flow. The area inside the left ventricular pressure–volume loop corresponds to the work performed by the ventricle on the blood. Lumped parameter models of the heart are often developed with the aim of replicating the pressure–volume loop under a range of physiologic states, providing insight into cardiac workload and function.

The one-dimensional equations of blood flow (introduced by Hughes and others in the 1970s) also offer an attractive means to obtain near real-time solutions of circulatory flow dynamics, and can be coupled to 3D solvers as boundary conditions.[26] Because they account for vessel wall elasticity, they reveal wave propagation phenomenon that cannot be captured with lumped parameter models.

The advent of patient specific modeling in the 1990s paved the way for increasingly detailed flow and pressure information to be solved on an individualized basis. Starting from patient image data (typically MRI or CT) a three dimensional model is constructed to represent a portion of the anatomy, often including a diseased region of interest. Since only a portion of a patients anatomy can be included in the 3D model, both due to computational expense and limits of image resolution, boundary conditions must be applied at inlets and outlets of the model to accurately represent the vascular network outside. Patient specific modeling has been applied to a wide range of cardiovascular disease applications, including abdominal aortic aneurysms, cerebral aneurysms, coronary artery disease, heart valves, and congenital heart disease. In the chapters to follow, outline procedures for patient specific modeling and available methods for flow simulations. We then outline the basic mathematical formulations for boundary conditions and multiscale modeling methods used in computational fluid dynamics simulations of blood flow.

Taking a global view of the above modeling methods, we observe a trade-off in computational cost vs. local resolution, as illustrated in Figure **??**. In particular, 0D methods offer only global flow and pressure waveforms with no spatial information, but can be solved with extremely low computational

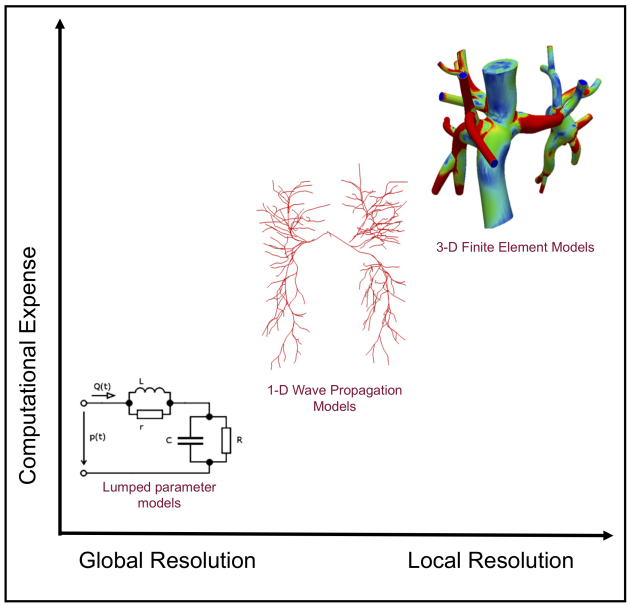


Figure 1.1: Levels of complexity and computational cost for common cardiovascular modeling methods. 0D models offer no spatial information but extremely low computational cost. 1D models offer one spatial dimension at modest computational cost. 3D models offer detailed local hemodynamics at substantial computational cost.

cost. Increasing in both resolution and cost, 1D models provide one spatial dimension and modest computational cost. Three-dimensional models offer detailed spatially and temporally-resolved velocity and pressure information but at substantial computational cost.

# Chapter 2

# Mathematical Preliminaries

## 2.1 Introduction

To perform meaningful simulations of blood flow and vascular tissues in the cardiovascular system, we must first establish some fundamental principles governing the laws of fluid motion and solid mechanics based on conservation of mass, momentum and energy. In this text we will present several modeling approaches for the cardiovascular system, increasing in complexity from reduced order models to detailed temporally and spatially resolved hemodynamic solutions. Before we attempt derivations of these different types of models, it is essential to review some fundamental principles and derive the governing fluid and solid mechanics equations.

## 2.2 Basic Theorems

**Theorem 2.2.1** ***Leibnitz Integral Rule*** *tells us how to take the derivative of an integral,*

$$\frac{d}{dt}\int_{a(t)}^{b(t)} f(x,t)dx = f(b(t),t)\dot{b}(t) - f(a(t),t)\dot{a}(t) + \int_{a(t)}^{b(t)} \frac{\partial f(x,t)}{\partial t}dx \ . \quad (2.1)$$

*This holds if $f$ is $C^1$.*

**Theorem 2.2.2** ***Gauss Divergence Theorem*** *tells us that the flux of fluid to/from a region is related to the divergence of the velocity field in that region,*

$$\int_{\partial V} (\mathrm{v} \cdot \hat{n}) dA = \int_{V} (\nabla \cdot \mathrm{v}) dV \ , \tag{2.2}$$

*where $\partial V$ denotes the closed boundary of the compact subset $V \in \mathbb{R}^n$, and $\hat{n}$ is the outward unit normal to $\partial V$.*

You should convince yourself that indeed the left-hand side of Eq. (2.2) is by definition the flux from region $V$. Additionally, since $\hat{n}$ is the *outward* normal, an outflow is positive and inflow negative. Therefore, positive divergence would correspond to expansion, or a source. Whereas negative divergence would correspond to compression, or a sink.

**Theorem 2.2.3** ***Reynolds Transport Theorem*** *tells us how to compute the rate of change of a property $B$ over a control volume $V$ that is transported by the flow.*

$$\frac{d}{dt} \int_{V(t)} b(x,t)\rho(x,t) dV = \tag{2.3}$$

$$\int_{V(t)} \frac{\partial \rho(x,t) b(x,t)}{\partial t} dV + \int_{\partial V(t)} \rho(x,t) b(x,t) \mathrm{v}(x,t) \cdot \hat{n} dA \tag{2.4}$$

*where $b$ is $B$ per unit mass.*

**Proof.** For brevity, the dependence on $x$ and $t$ of the variables in the proof

is implied but not written.

$$\begin{aligned}
\frac{dB}{dt} &= \frac{d}{dt}\int_{V(t)} b\rho dV \\
\text{(Change of Variables Theorem)} &= \frac{d}{dt}\int_{V(0)} b\rho J dV \\
\text{(Leibnitz Integration Rule)} &= \int_{V(0)} \frac{\partial}{\partial t}[b\rho J] dV \\
\text{(Leibnitz Product Rule)} &= \int_{V(0)} \left[\frac{\partial \rho b}{\partial t} J + \rho b \frac{\partial J}{\partial t}\right] dV \\
\text{(Property of Jacobian, cf. §1.1 of [10])} &= \int_{V(0)} \left[\frac{\partial \rho b}{\partial t} J + \rho b \nabla \cdot \mathrm{v} J\right] dV \\
\text{(Change of Variables Theorem)} &= \int_{V(t)} \left[\frac{\partial \rho b}{\partial t} + \rho b \nabla \cdot \mathrm{v}\right] dV \\
\text{(Gauss Divergence Theorem)} &= \int_{V(t)} \frac{\partial \rho b}{\partial t} dV + \int_{\partial V(t)} \rho b \mathrm{v} \cdot \hat{n} dA
\end{aligned} \tag{2.5}$$

where $J$ denotes the Jacobian determinant, $|\nabla F|$, where $F : V(0) \mapsto V(t)$ is the flow map. □

## 2.3 Conservation Laws

**Conservation of mass** The mass conservation law states that mass can neither be created or destroyed. That is, consider the fluid enclosed by some arbitrary volume $V(0)$ at time $t = 0$. Over time, this fluid deforms into the volume $V(t)$, but due to conservation of mass, the mass of $V(t)$ must remain fixed. Stated mathematically,

$$\frac{dM}{dt} = \frac{d}{dt}\int_{V(t)} \rho(x,t) dV = 0 \,. \tag{2.6}$$

Letting $B = m$, and hence $b = 1$, in Eq. (2.3), from the proof of Thm. 2.2.3 we can restate conservation of mass as

$$\int_{V(t)} \left[\frac{\partial \rho(x,t)}{\partial t} + \rho(x,t) \nabla \cdot \mathrm{v}(x,t)\right] dV = 0 \,. \tag{2.7}$$

Since this integral must hold for all $V(t)$), the integrand must be zero,

$$\frac{\partial \rho(x,t)}{\partial t} + \rho(x,t)\nabla \cdot \mathrm{v}(x,t) = 0 \; . \tag{2.8}$$

If the fluid's density is constant, then this reduces to

$$\nabla \cdot \mathrm{v}(x,t) = 0 \; . \tag{2.9}$$

**Momentum balance** Newton's second law states

$$\frac{dm\mathrm{v}}{dt} = \sum F \tag{2.10}$$

For continuums, Newton's second law is typically applied to a infinitesimal volume. Assuming density is constant, we can write Eq. (2.10) as

$$\rho \frac{d\mathrm{v}}{dt} = \frac{\sum F}{\delta x \delta y \delta z} \tag{2.11}$$

Forces are typically broken into body forces $B$ and surface forces $R$.

Any surface force can be broken into components perpendicular and tangent to the surface. Let $\tau_{ij}$ be the surface force per unit area in the $j$ direction acting on the plane with normal $n$ in the $i$ direction, also called the stress tensor. Therefore

$$\sum F_i = \left[ \frac{\partial \tau_{xi}}{\partial x} + \frac{\partial \tau_{yi}}{\partial y} + \frac{\partial \tau_{zi}}{\partial z} \right] \delta x \delta y \delta z$$

Letting the *stress tensor* be

$$\tau = \begin{bmatrix} \tau_{xx} & \tau_{yx} & \tau_{zx} \\ \tau_{xy} & \tau_{yy} & \tau_{zy} \\ \tau_{xz} & \tau_{yz} & \tau_{zz} \end{bmatrix} \tag{2.12}$$

Newton's second law becomes

$$\rho \frac{d\mathrm{v}}{dt} = \rho g + \nabla \cdot \tau \tag{2.13}$$

where we have assumed that weight is the only body force, $B = g\rho\delta x\delta y\delta z$. This equation, expressing conservation of momentum for a continuum, is often called Cauchy's equation of motion. This equation relates fluid-particle acceleration to the body and surfaces forces on the particle. It holds in any continuum, fluid or solid.

## 2.4 Equations of Fluid Mechanics

### 2.4.1 Navier-Stokes Equations

The total or material derivative for a scalar quantity $F$ is

$$\frac{DF}{Dt} = \frac{dF}{dt} = \frac{\partial F}{\partial t} + \mathrm{v} \cdot \nabla F$$

Replacing $F$ with the fluid velocity vector v, as in Equation 2.13 we arrive at the unsteady and advective terms

$$\frac{D\mathrm{v}}{Dt} = \frac{d\mathrm{v}}{dt} = \frac{\partial \mathrm{v}}{\partial t} + (\mathrm{v} \cdot \nabla)\mathrm{v}$$

The stress tensor $\tau_{ij}$ is described in terms of static ($p$) and dynamic ($\sigma_{ij}$) components as

$$\tau_{ij} = -p\delta_{ij} + \sigma_{ij} \tag{2.14}$$

For incompressible and Newtonian fluids, in which the relationship between stress and strain rate is linear, the stress tensor becomes

$$\tau_{ij} = -p\delta_{ij} + 2\mu S_{ij}$$

where

$$S_{ij} = \frac{1}{2}\left(\frac{\partial \mathrm{v}_i}{\partial x_j} + \frac{\partial \mathrm{v}_j}{\partial x_i}\right)$$

is the strain rate tensor.

Substituting into Cauchy's equations, we arrive at the equation of conservation of momentum for a Newtonian incompressible fluid

$$\rho\frac{D\mathrm{v}}{Dt} = -\nabla p + \rho g + \mu\nabla^2\mathrm{v} \tag{2.15}$$

which, together with the conservation of mass, forms the Navier-Stokes equations governing conservation of mass and momentum

$$\begin{aligned} \frac{\partial \mathrm{v}}{\partial t} + (\mathrm{v} \cdot \nabla)\mathrm{v} &= -\nabla p + \rho g + \mu\nabla^2\mathrm{v} && (2.16) \\ \nabla \cdot \mathrm{v} &= 0. && (2.17) \end{aligned}$$

## 2.5 Equations of Solid Mechanics

### 2.5.1 Linear Elasticity

Next, we consider the equations of linear elasticity, which model how solid objects stress and deform in response to prescribed loading.

We solve for the $(x, y, z)$ displacements, which is a vector quantity. Thus, all of the following equations apply to all components. If we are solving linear elasticity in $n_{sd} = 3$ dimensions, we will have three sets of equations to solve for each of the three components of displacement.

Consider a domain $\Omega \in \mathbb{R}^n$, where $n = 2$ or 3 is the number of spatial dimensions. The boundary $\Gamma$ of this domain $\Omega$ is decomposed into $\Gamma_g$ and $\Gamma_h$ such that $\Gamma = \Gamma_g \cup \Gamma_h$ and $\emptyset = \Gamma_g \cap \Gamma_h$. The linear elasticity equation is given by:

$$\begin{aligned} \rho \frac{\partial^2 \vec{u}(\vec{x}, t)}{\partial t^2} + \nabla \cdot \underline{\sigma}(\vec{x}, t) + \vec{f}(\vec{x}, t) = 0, \quad & in\ \Omega \\ \vec{u}(\vec{x}, t) = \vec{g}(\vec{x}, t), \quad & on\ \Gamma_g \\ \underline{\sigma}(\vec{x}, t) \cdot \hat{n} = \vec{h}, \quad & on\ \Gamma_h \end{aligned} \tag{2.18}$$

Here, $\vec{u}(\vec{x}, t) = (u_x, u_y, u_z)$ represents the displacement vector, $\underline{\sigma}$ is the Cauchy stress tensor, $\rho$ is the density of your material, $\vec{f}$ is a prescribed body force per unit volume, $\vec{g}(\vec{x}, t)$ are prescribed displacements on the Dirichlet boundary $\Gamma_g$, and $\vec{h}$ are prescibed tractions on the Neumann boundary $\Gamma_h$. Here, we assume the material is linear and isotropic, so the Cauchy stress tensor $\underline{\sigma}$ is related to the displacements $\vec{u}$ through a generalized Hooke's Law:

$$\underline{\sigma} = \underline{D}\vec{\epsilon}(\vec{u}) \tag{2.19}$$

Here, $\vec{\epsilon}(\vec{u})$ is the vector form of the strain tensor, whose components are given by:

$$\begin{aligned}\vec{\epsilon}(\vec{u}) &= \left(\frac{\partial u_x}{\partial x}, \frac{\partial u_y}{\partial y}, \frac{\partial u_x}{\partial y} + \frac{\partial u_y}{\partial x}\right), \quad for\ n_{sd} = 2 \\ \vec{\epsilon}(\vec{u}) &= \left(\frac{\partial u_x}{\partial x}, \frac{\partial u_y}{\partial y}, \frac{\partial u_z}{\partial z}, \frac{\partial u_y}{\partial z} + \frac{\partial u_z}{\partial y}, \frac{\partial u_x}{\partial z} + \frac{\partial u_z}{\partial x}, \frac{\partial u_x}{\partial y} + \frac{\partial u_y}{\partial x}\right), \quad for\ n_{sd} = 3\end{aligned} \tag{2.20}$$

$\underline{D}$ represents the matrix of material constants. For a linear, isotropic material $\underline{D}$ is given by:

$$\begin{aligned}\underline{D} &= \begin{bmatrix} \lambda + 2\mu & \lambda & 0 \\ \lambda & \lambda + 2\mu & 0 \\ 0 & 0 & \mu \end{bmatrix}, \quad for\ n_{sd} = 2 \\ \underline{D} &= \begin{bmatrix} \lambda + 2\mu & \lambda & \lambda & 0 & 0 & 0 \\ \lambda & \lambda + 2\mu & \lambda & 0 & 0 & 0 \\ \lambda & \lambda & \lambda + 2\mu & 0 & 0 & 0 \\ 0 & 0 & 0 & \mu & 0 & 0 \\ 0 & 0 & 0 & 0 & \mu & 0 \\ 0 & 0 & 0 & 0 & 0 & \mu \end{bmatrix}, \quad for\ n_{sd} = 3\end{aligned} \tag{2.21}$$

Here, $\lambda$ and $\mu$ are known as the **Lamé parameters**. These are often defined in terms of the Young's modulus $E$ and Poisson's ratio $\nu$:

$$\begin{aligned}\lambda &= \frac{\nu E}{(1+\nu)(1-2\nu)} \\ \mu &= \frac{E}{2(1+\nu)}\end{aligned} \tag{2.22}$$

When solving the linear elastic equation numerically, one typically specifies the Young's modulus and Poisson's ratio of the solid.

## 2.6 Vector quantities in cylindrical coordinates

For completeness, we recall the following definitions for the gradient and divergence operators in cylindrical coordinates.

**Gradient**

$$\nabla f = \frac{\partial f}{\partial r} e_r + \frac{1}{r} \frac{\partial f}{\partial \theta} e_\theta + \frac{\partial f}{\partial z} e_z \tag{2.23}$$

**Divergence**

$$\nabla \cdot \mathrm{v} = \frac{1}{r} \left[ \frac{\partial}{\partial r}(r v_r) + \frac{\partial v_\theta}{\partial \theta} + \frac{\partial}{\partial z}(r v_z) \right] \tag{2.24}$$

# Chapter 3

# Steady flow in rigid vessels

## 3.1 Introduction

At the simplest level, blood flow in the vascular system can be thought of as flow of an incompressible fluid through a system of pipe-shaped vessels, the veins and arteries. We therefore begin by examining the analytical solution of the Navier Stokes equations for steady flow in a rigid pipe. In subsequent chapters, we will extend our considerations to include more realistic cases of pulsatile flow, deformable vessel walls, and complex geometries. However, the steady pipe flow example has many practical uses. The most important of these, from the perspective of blood flow, is the estimation of resistance of a segment of vessel. In this chapter, we will use this solution to derive Murray's law, an analytical relationship describing the branching structure of vascualr networks. Murray's law is widely applicable to branched networks in the human vasculature, including the pulmonary and coronary circulations, and can even be generalized to describe branching patterns in plants and other bifurcating fluidic transport networks.

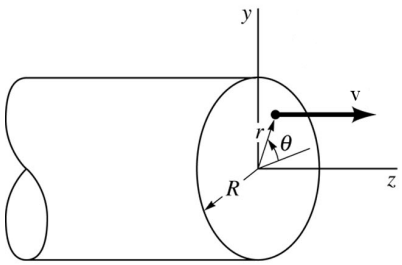


Figure 3.1: Coordinates used to derive Poisseulle flow.

## 3.2 Hagen-Poiseuille solution

The Poiseulle solution is perhaps the most famous analytic solution to the Navier Stokes equations. Our aim is to determine the velocity profile in a rigid, straight pipe with circular cross section, as a function of the radial distance (Fig. 3.1). The major assumptions used to reduce the Navier Stokes equations to a solvable form are that the flow is axial, axisymmetric, Newtonian, incompressible and steady.

Our starting point is the Navier Stokes equations, which are the governing equations for conservation of mass (continuity)

$$\rho\left[\frac{\partial \mathrm{v}}{\partial t} + \mathrm{v}\cdot\nabla\mathrm{v}\right] = -\nabla p + \mu\nabla\cdot\nabla\mathrm{v} \tag{3.1}$$

and conservation of momentum

$$\nabla\cdot\mathrm{v} = 0. \tag{3.2}$$

The continuity equation (Eq. 3.2) in cylindrical coordinates (Eq. 2.24) is given by

$$\frac{1}{r}\frac{\partial}{\partial r}\left(rv_r\right) + \frac{1}{r}\frac{\partial}{\partial\theta}\left(v_\theta\right) + \frac{\partial}{\partial z}\left(v_z\right) = 0. \tag{3.3}$$

The assumption of strictly axial flow implies

$$\mathrm{v} = (v_r, v_\theta, v_z) = (0, 0, v_z) \tag{3.4}$$

and the continuity equation therefore simplifies to

$$\frac{\partial v_z}{\partial z} = 0, \tag{3.5}$$

so that,

$$v_z = v_z(r, \theta). \tag{3.6}$$

Since flow is assumed to be axisymmetric, changes in the azimuthal direction are negligible, $\frac{\partial}{\partial \theta} = 0$, and hence

$$v_z = v_z(r). \tag{3.7}$$

Now let us turn to the momentum equation (Eq. 3.1). The three components of the momentum equation written in cylindrical coordinates are:
$r$-component:

$$\begin{aligned}&\frac{\partial v_r}{\partial t} + v_r\frac{\partial v_r}{\partial r} + \frac{v_\theta}{r}\frac{\partial v_r}{\partial \theta} - \frac{v_\theta^2}{r} + v_z\frac{\partial v_r}{\partial z}\\ &= -\frac{1}{\rho}\frac{\partial p}{\partial r} + g_r + \nu\left(\frac{1}{r}\frac{\partial}{\partial r}\left(r\frac{\partial v_r}{\partial r}\right) - \frac{v_r}{r^2} + \frac{1}{r^2}\frac{\partial^2 v_r}{\partial \theta^2} - \frac{2}{r^2}\frac{\partial v_\theta}{\partial \theta} + \frac{\partial^2 v_r}{\partial z^2}\right)\end{aligned} \tag{3.8}$$

$\theta$-component:

$$\begin{aligned}&\frac{\partial v_\theta}{\partial t} + v_r\frac{\partial v_\theta}{\partial r} + \frac{v_\theta}{r}\frac{\partial v_\theta}{\partial \theta} + \frac{v_r v_\theta}{r} + v_z\frac{\partial v_\theta}{\partial z}\\ &= -\frac{1}{\rho}\frac{\partial p}{\partial \theta} + g_\theta + \nu\left(\frac{1}{r}\frac{\partial}{\partial r}\left(r\frac{\partial v_\theta}{\partial r}\right) - \frac{v_\theta}{r^2} + \frac{1}{r^2}\frac{\partial^2 v_\theta}{\partial \theta^2} + \frac{2}{r^2}\frac{\partial v_r}{\partial \theta} + \frac{\partial^2 v_\theta}{\partial z^2}\right)\end{aligned} \tag{3.9}$$

$z$-component:

$$\begin{aligned}&\frac{\partial v_z}{\partial t} + v_r\frac{\partial v_z}{\partial r} + \frac{v_\theta}{r}\frac{\partial v_z}{\partial \theta} + v_z\frac{\partial v_z}{\partial z}\\ &\qquad = -\frac{1}{\rho}\frac{\partial p}{\partial z} + g_z + \nu\left(\frac{1}{r}\frac{\partial}{\partial r}\left(r\frac{\partial v_z}{\partial r}\right) + \frac{1}{r^2}\frac{\partial^2 v_z}{\partial \theta^2} + \frac{\partial^2 v_z}{\partial z^2}\right).\end{aligned} \tag{3.10}$$

Since flow is assumed steady,

$$\frac{\partial \mathrm{v}}{\partial t} = 0 \tag{3.11}$$

and since $v_z$ is not a function of $z$ from Eq.(3.5), there is no convective acceleration so that

$$\mathrm{v} \cdot \nabla \mathrm{v} = 0. \tag{3.12}$$

Therefore, the acceleration terms comprising the left hand side of Eq. (3.1) and thus also Eqs. 3.8-3.10 are zero.

Now consider the viscous force term $\mu \nabla \cdot \nabla \mathrm{v}$. Note

$$\nabla \cdot \nabla \mathrm{v} = \begin{bmatrix} 0 \\ 0 \\ \nabla \cdot \nabla v_z \end{bmatrix}. \tag{3.13}$$

From Eq. (3.7), it is clear that only a velocity gradient in the radial direction is permissible so that

$$\nabla v_z = \frac{\partial v_z}{\partial r} e_r. \tag{3.14}$$

Applying this assumption to Eqs. 3.8-3.10, the momentum equation, in component form, becomes

$$0 = -\frac{\partial p}{\partial r} \tag{3.15}$$

$$0 = -\frac{1}{r}\frac{\partial p}{\partial \theta} \tag{3.16}$$

$$0 = -\frac{\partial p}{\partial z} + \mu \frac{1}{r}\frac{d}{dr}\left(r \frac{dv_z}{dr}\right), \tag{3.17}$$

where we have used the fact that

$$\frac{\partial v_z}{\partial r} = \frac{dv_z}{dr}$$

since $v_z$ is only a function of $r$. The first and second equations imply $p$ is only a function of $z$, and the last equation implies that $\frac{\partial p}{\partial z}$ is only a function of $r$. These conditions can only be satisfied if

$$p = K_1 + K_2 z, \tag{3.18}$$

where $K_1$ and $K_2$ are constants. Therefore, pressure varies linearly down the length of the pipe; or alternatively, *the pressure gradient is constant.* Integrating Eq. (3.17) once (using $\frac{\partial p}{\partial z} = \frac{dp}{dz} =$ constant) yields,

$$r \frac{dv_z}{dr} = \frac{1}{2\mu} r^2 \frac{dp}{dz} + C_1 \tag{3.19}$$

and a second time gives,

$$v_z = \frac{1}{4\mu} r^2 \frac{dp}{dz} + C_1 \ln r + C_2. \tag{3.20}$$

To obtain a physical solution, we require $v_z(0) < \infty$ and thus $C_1 = 0$. To find $C_2$ we use the no-slip boundary condition such that velocity is zero at the wall, $v_z(R) = 0$, to obtain

$$C_2 = -\frac{1}{4\mu} R^2 \frac{dp}{dz}.$$

Finally, the axial velocity profile is given by

$$v_z(r) = \frac{1}{4\mu} \frac{dp}{dz} (r^2 - R^2). \tag{3.21}$$

This is the famous Hagen-Poiseuille solution of the Navier Stokes equations for steady flow in a cylindrical pipe. The solution shows that the velocity profile in the pipe is parabolic (Fig. 3.2).

As expected, $r^2 - R^2 \leq 0$ implies that flow is opposite the direction of the pressure gradient $\frac{dp}{dz}$, and $v_z$ is maximum at the center of the pipe when $r = 0$. Note,

$$v_{z,\max} = -\frac{1}{4\mu} \frac{\partial p}{\partial z} R^2$$

and therefore, we can rewrite $v_z$ as

$$v_z = v_{z,\max} \left( 1 - \frac{r^2}{R^2} \right).$$

Lastly, recall that Eq. (3.1) is just a form of Newton's 2nd Law, $\Sigma F = ma$. We showed that $a = 0$ and thus $\Sigma F = 0$; the pressure forces balance the viscous forces. As we make analogies with electrical circuits in the following chapters, it will be useful to think about the resistance as a ratio of pressure drop to flow rate, where pressure drop is caused by viscous losses.

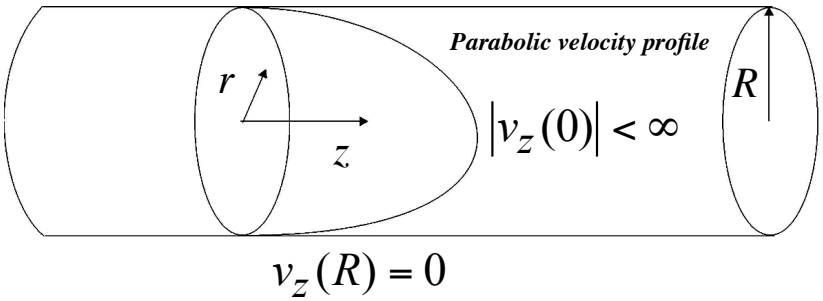


Figure 3.2: Parabolic flow profile in a straight circular pipe

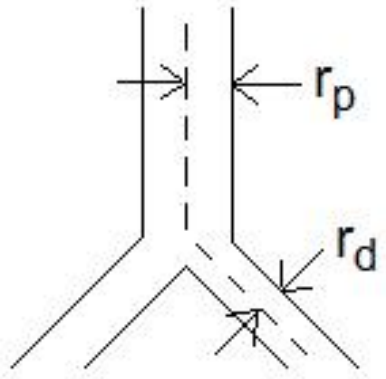


Figure 3.3: Bifurcation of parent vessel into two daughter vessels

## 3.3 Murray's Law for blood vessel bifurcations

Cecil D. Murray's original 1926 study was intended to determine the optimal relationshiop between blood vessel radii in a bifurcating tree that would require the minimum expenditure of energy by an organism[52]. Murray's analysis predicts the optimal ratio between parent vessel radius, $r_p$, and daughter vessel radius, $r_d$, at a bifurcation, and hence the branching structure of the vascular tree. Murray's analysis considers two competing factors in the optimization of blood vessel radii:

1. As the vessel radius decreases, the work required to drive the flow goes up due to increased viscous resistance.

2. As the vessel radius increases, the blood volume goes up and so does the "metabolic maintenance" cost to the body.

For our analysis we will assume blood flow has the steady, parabolic profile derived above in § 3.2

$$v_z(r) = -\frac{dp}{dz}\left(\frac{R^2 - r^2}{4\mu}\right).$$

The volumetric flow rate is thus given by

$$Q = \int_A v_z(r) dA = \int_0^R 2\pi v_z r dr = -\frac{\pi R^4}{8\mu}\frac{dp}{dz}. \tag{3.22}$$

Since the pressure gradient is constant,

$$-\frac{dp}{dz} = \frac{\Delta p}{L}, \tag{3.23}$$

where $\Delta p$ is the pressure *drop* from inlet to outlet of the vessel, and $L$ is the length of the vessel.

Note that we can re-write Eq. (3.22) as

$$\Delta P = \frac{8\mu L}{\pi R^4} Q \tag{3.24}$$

and define the **resistance** $\mathcal{R}$ by

$$\mathcal{R} = \frac{8\mu L}{\pi R^4} \tag{3.25}$$

so that

$$\Delta P = Q\mathcal{R}\ . \tag{3.26}$$

This gives a mechanical equivalent to Ohm's Law–the electrical relation between voltage ($V$) and current ($I$):

$$V = I\mathcal{R}, \tag{3.27}$$

where flow rate $Q$ is analogous to current $I$ and pressure drop $\Delta P$ is analogous to voltage $V$.

Consider a free body diagram of the vessel. Recall that power is force $\times$ velocity (if the flow is steady). Due to the no-slip condition on the walls, the only work done is at the inlet and outlet. Since the velocity profile is the same at the inlet and outlet, work is due to the difference in pressure. That is,

$$\dot{W}_p = P_p = \frac{\Delta p}{A}\bar{v} = \Delta p \frac{\bar{v}}{A} = \Delta p Q \tag{3.28}$$

where $\bar{v}$ denotes the average of the velocity over the cross-section and the subscript $p$ denotes that this is work to overcome pressure difference. Next, assume that the rate of metabolic energy consumption needed to pump blood is proportional to the amount of the blood pumped, i.e. $\dot{W}_m = bV$, where $b$ is the proportionality constant. Therefore, we have

1. The power required to maintain the blood flow: $\Delta p Q = \frac{Q^2 8\mu L}{\pi R^4}$
2. The power required for blood maintenance: $b\cdot$ Volume $= bL\pi R^2$

where we have combined Eqs. (3.22) and (3.28).

Assume the total power to pump blood comes from the two contributions above,

$$\dot{W} = \frac{Q^2 8\mu l}{\pi R^4} + bl\pi R^2 \tag{3.29}$$

Our goal is to determine the optimal vessel radius, or more precisely the branching pattern to minimize the body's power consumption. With that in mind, a necessary condition for minimum power consumption is

$$\frac{d\dot{W}}{dR} = 0, \tag{3.30}$$

thus we require

$$\frac{d\dot{W}}{dR} = -\frac{4Q^2 8\mu L}{\pi R^5} + 2bL\pi R = 0. \tag{3.31}$$

We have treated $Q$ as constant because we have already used its dependence on R in deriving Eq. (3.29). The flow rate at this potentially optimal state

is given by

$$Q = \underbrace{\sqrt{\frac{\pi^2 b}{16\mu}}}_{=\text{constant}} R^3 = KR^3, \tag{3.32}$$

where we have defined the constant $K$. Next, let us see what this implies at vessel bifurcations.

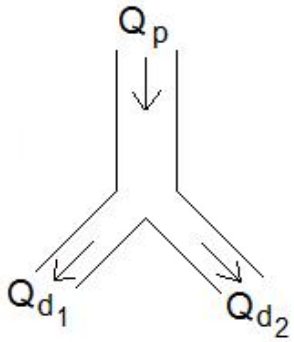


Figure 3.4: Flow rates at bifuraction

By conservation of mass, at a vessel bifurcation

$$Q_p = Q_{d_1} + Q_{d_2}. \tag{3.33}$$

Using Eq. (3.32) this implies

$$K{R_p}^3 = K{R_{d_1}}^3 + K{R_{d_2}}^3. \tag{3.34}$$

Canceling the common constant, $K$, yields **Murray's Law** for two branches:

$$\boxed{{R_p}^3 = {R_{d_1}}^3 + {R_{d_2}}^3}. \tag{3.35}$$

It is important to note that the law rests on two assumptions: (1) that the flow under consideration is a steady Poiseuille flow, and (2) that branching is meant to minimize the total rate of energy expenditure to balance viscous losses against metabolic demands of the body.

If the bifurcation is symmetric ($R_{d_1} = R_{d_2} = R_d$), we can write

$${R_p}^3 = 2{R_d}^3 \Rightarrow R_d = 0.8R_p. \tag{3.36}$$

| **Artery** | **Diameter (cm)** | $\alpha$ |
|---|---|---|
| Large Arteries | .2-.5 | 2.4-2.65 |
| Small Arteries | .025-.05 | 2.65-2.9 |
| Arterioles | .0005-.025 | 2.75-3 |
| Capillaries | .0003-.0005 | 3 |

Table 3.1: List of various arteries and corresponding $\alpha$ value ranges

For repeated symmetric bifurcations, we can write

$$R_d^i = 2^{-i/3} R_p \tag{3.37}$$

where $R_d^i$ is the radius at the $i$th generation of the tree.

In general, we can characterize bifurcations in the cardiovascular system by the relation

$$r_0{}^\alpha = r_1{}^\alpha + r_2{}^\alpha \ . \tag{3.38}$$

Murray's law determined an optimal value of $\alpha = 3$. However, in the body, there is actually a range of observed $\alpha$ values. Typically, smaller blood vessels tend to obey Murray's law more closely than larger ones. This should seem reasonable since flow is mostly steady, 1D and fully developed (assumptions used to derive Murray's Law) in the distal circulation. Table 3.1 is a list of various sized arteries and their corresponding approximate $\alpha$ values.

To better discuss the effects of various $\alpha$ values, it is useful to first define the area ratio, $\beta$, as

$$\beta = \frac{r_1{}^2 + r_2{}^2}{r_0{}^2} \tag{3.39}$$

$\beta$, is the ratio of combined cross-sectional area of the two daughter vessels over that of the parent vessel. Therefore, it follows that values of $\beta > 1$ (typically observed in the human body) produce an expansion in total cross-sectional area as flow progresses from parent to daughter blood vessels. There are three possible value ranges for the exponent $\alpha$ from equation (11):

1. $\alpha < 2 \Rightarrow \beta < 1 \Rightarrow$ Area contraction
2. $\alpha = 2 \Rightarrow \beta = 1 \Rightarrow$ Area preservation

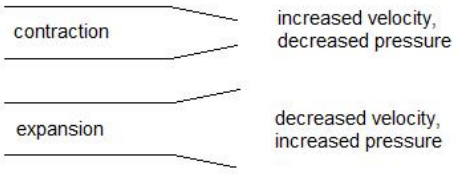


Figure 3.5: Flow rates at bifurcation

3. $\alpha > 2 \Rightarrow \beta > 1 \Rightarrow$ Area expansion

The case of ($\beta < 1$) results in an increasing flow velocity and a decrease in pressure as blood moves downstream. The case of ($\beta > 1$) results in a decreasing flow velocity and an increase in pressure as blood moves downstream. In the case of area preservation ($\beta = 1$), there is minimal wave reflection and thus maximum wave transmission.

For the parabolic velocity profile and flow rate described previously, namely,

$$v_z(r) = -\frac{dp}{dz}\left(\frac{R^2 - r^2}{4\mu}\right) \tag{3.40}$$

and

$$Q = \frac{\pi R^4}{8\mu}\left(-\frac{dp}{dz}\right), \tag{3.41}$$

we can calculate the shear stress at the wall as

$$\tau_w = \mu \frac{dv_z}{dr}\bigg|_{r=R} = -\frac{dp}{dz}\frac{R}{2}. \tag{3.42}$$

Combining these two equations we find

$$\tau_w = \frac{4Q\mu}{\pi R^3}. \tag{3.43}$$

Thus, the shear stress acting on the wall of the parent vessel is

$$\tau_{wp} = \frac{4Q_p\mu}{\pi {R_p}^3}. \tag{3.44}$$

For a symmetric bifurcation, conservation of mass gives $Q_p$=$2Q_d$, and the Murray's Law relationship gives ${R_p}^3 = 2{R_d}^3$, so we can rewrite this as

$$\tau_{wp} = \frac{4(2Q_d)\mu}{\pi(2{R_d}^3)} = \frac{4Q_d\mu}{\pi {R_d}^3} \tag{3.45}$$

, which is equal to the wall shear stress of the daughter vessels. Thus,

$$\boxed{\tau_{wp} = \tau_{wd}} \tag{3.46}$$

This tells us that vessel wall shear stress is constant throughout a symmetric bifurcating system if Murray's Law is satisfied. It also suggests that shear stress is likely an important biomechanical parameter used to regulate vessel caliber. For example, if instead of Murray's Law $Q \propto R^3$, flow rate varied in accordance to a square law or quartic law, then shear stress would be proportional to $1/R$ or $R$ respectively. Therefore, since vessel size varies 4 orders of magnitude, then shear stress in this hypothetical scenario would vary over 4 orders of magnitude in the cardiovascular system.

## 3.4 Problems

- It was shown in § 3.2 that flow occurs in the opposite direction of the pressure gradient, alternatively fluid flows from higher pressure to lower pressure. Is it possible to have fluid flow from a lower pressure to higher pressure? If so, under what conditions might this occur?
- Derive Eq. (3.22).

# Chapter 4

# Scaling Laws and Design Principles

In this chapter, we consider the scaling relationships of structure, physiology, and function in the cardiovascular system. The main function of the cardiovascular system is to transport blood, containing nutrients, oxygen, hormons and other factors, to the various organs and tissues of the body. The physics of these transport mechanisms may change in different species and at different length scales. This leads us to consider a variety of competing "design principles" that are at play and whether unifying mathematical relationships can be developed to relate quantities across multiple scales.

There is tremendous diversity of cardiovascular structure and function in the animal kingdom. Across different animal sizes, cardiovascular structure and function can vary tremendously, often arising from differences in the physics of transport processes at different scales. Mammals range in size from the tiny tree shrew to the blue whale. Anatomy also varies considerably across species of different clasifications. While most vertebrates, including humans and other mammals, have a four chambered heart, other animals, such as insects and amphibians, may have different cardiac structures and blood delivery systems, if they have them at all! For example, frogs have two atria but only one ventricle, owing to supplemental oxygen diffusion through their skin. Cephalopods, including octopus and squid, have three hearts. Two brachial hearts on either side of the cephalopod's body oxygenate blood by

pumping it through the blood vessels of the gills, and the systemic heart in the center of the body pumps oxygenated blood from the gills through the rest of the organism. Cockroaches have an open circulatory system with no blood at all. Roaches and other insects breathe through spiracles (surface openings) in their bodies instead of lungs, so the blood doesnt need to carry oxygen from one place to another.

The study of allometry allows us to express generalized scaling principles of cardiovascular structure and function across different species and body sizes. It is used to define unifying scaling principles for physiologic parameters like heart rate or blood pressure or structural quantities like vessel size across species and size. Allometric scaling typically uses a power law to relate a given quantity to body mass. These laws will be discussed in detail below.

There are numerous practical and clinical reasons for needing allometry. These include the need to extrapolate results from animal studies to humans, correct drug dosing estimates, and comparison and normalization of data across human patients of different size and age. In pediatrics, allometry is particularly useful for defining "normal" metrics for cardiac function in patients who are growing.

## 4.1 Design Principles

We start with a brief discussion of cardiovascular design principles that should be considered in comparisons across species and body size. The first of these considerations is the need for bulk transport of fluids to the end organs and tissues. Bulk fluid flow is necessary because diffusion is inadequate for sufficient delivery of blood to these locations. Diffusion of a substance across a surface of area $A$ can be described by the following relationship,

$$\frac{dS}{dt} = -DA\frac{dC}{dx}, \tag{4.1}$$

where $dS/dt$ is the flux of substance through area $A$, which is proportional to the concentration gradient $dC/dx$. The proportionality constant is the diffusivity or diffusion coefficient $D$. For small spherical particles, the Einstein-

Stokes equation can be used

$$D = \frac{k_b T}{6\pi\mu r}$$

where $k_b$ is Boltzmann's constant (Gas constant divided by Avogadro's constant), $T$ is temperature, $\mu$ is viscosity and $r$ is the particle radius. In this expression, diffusion is inversely proportional to distance, and thus we see that it is ineffective at transport over large distances. The diffusion coefficient of platelets is estimated to be on the order of $10^{-6} - 10^{-7} cm^2/s$. This is clearly too small to achieve effective transport of blood through diffusion alone.

The need for bulk transport over large distances together with the need for evenly distributed delivery within a given organ system, has therefore resulted in a hierarchical vessel structure, in which large vessels transport blood over large distances, and smaller vessels, in a bifurcating tree structure, deliver blood to the tissues in each individual organ.

We have introduced an important principle of vascular structural relationships with Murray's law in the previous chapter. We recall that resistance is inversely proportional to $r^4$, where $r$ is the vessel radius. An optimal delivery system therefore requires that multiple vessels "share" the workload of small scale delivery by using a bifurcating vascular tree. We also recall that at a bifurcation, $r_p = 2r_d^\alpha$ and area preserving $\alpha = 2$ results in maximal wave transmission. However, minimum work results in $\alpha = 3$. Therefore, we find area-preserving large branches with Murray's law exponents closer to $\alpha = 2$ and area-increasing small branches with Murray's law exponents closer to $\alpha = 3$.

We have also seen that (for small vessels) vessel size is regulated by wall shear stress. But how does wall shear stress vary across species? What about vessel thickness? These and other questions can be examined with allometric scaling.

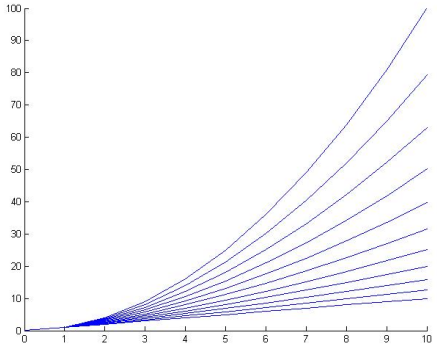


Figure 4.1: A generic family of power law relationships with varying exponential values

## 4.2 Allometric Scaling

Allometry is the study of the relationship of body mass to shape, anatomy, physiology, and behavior. This concept was introduced by Snell in 1892. Through years of biological data gathering, these relationships can be often be shown to obey "power laws." That is, the (nonlinear) relationship between body mass and an observed property can be modeled using

$$Y = Y_0 M^b \tag{4.2}$$

where $Y$ is the property, $Y_0$ is the reference value, $M$ is the body mass, and $b$ is an exponential constant that varies depending on the property. A range of generic power law relationships is shown in Figure 4.1. However, these laws are typically plotted on a log-log scale such that the allometric relationship appears as a straight line. The value of the exponential constant $b$ is typically found empirically.

Before proceding, we define two standard measures of cardiac function:

**Stroke Volume:** The volume of blood pumped from one ventricle in a cardiac cycle.

**Cardiac Output:** The volume of blood pumped by a ventricle in a unit of time, typically in units of $L/min$.

**Ejection Fraction:** Fraction of blood leaving the ventricule during each contraction.

Further, cardiac output can be found by multiplying stroke volume by heart rate:

$$CO = SV \times HR.$$

We also note that the cardiac index is often used to normalize cardiac output across patients of varying size. Cardiac index is defined by normalizing cardiac output with body surface area (BSA).

The following are allometric relationships for common properties that can be modeled using Eq. (4.2).

- Heart Rate $\sim M^{-1/4}$
- Stroke Volume $\sim M^{1}$
- Aortic Pressure $\sim M^{0}$
- Cardiac Output $\sim M^{3/4}$
- Total peripheral resistance $\sim M^{-3/4}$
- Metabolic Rate $\sim M^{3/4}$
- Blood Vessel Diameter $d \sim M^{\frac{3}{8}}$

Relationships for cardiac output, vessel diameter, and blood pressure are shown in Figures 4.2, 4.3 and 4.4, respectively. Some typical values of cardiac output derived from this relationship are provided for several species in Table 4.1. We note from these relationships that heart rate increases with decreasing body size, that stroke volume varies linearly with body mass, and, perhaps most interestingly, that blood pressure is constant across species.

We can now use these relationships to derive additional allometric relationships for which we may not have empirical data. In particular, we ask the question, "Is shear stress invariant across species?" Recall that for Poiseuille flow, wall shear stress is

$$\tau_w = \frac{4Q\mu}{\pi r^3} = \frac{32Q\mu}{\pi d^3} \, .$$

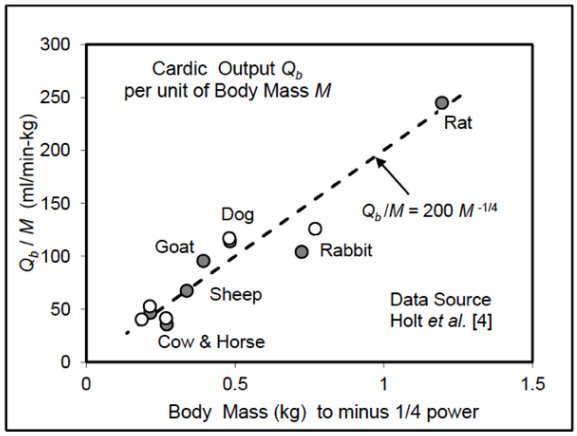


Figure 4.2: Allometric relationship between cardiac output per unit mass and body mass to the minus 1/4 power for mammalian species.

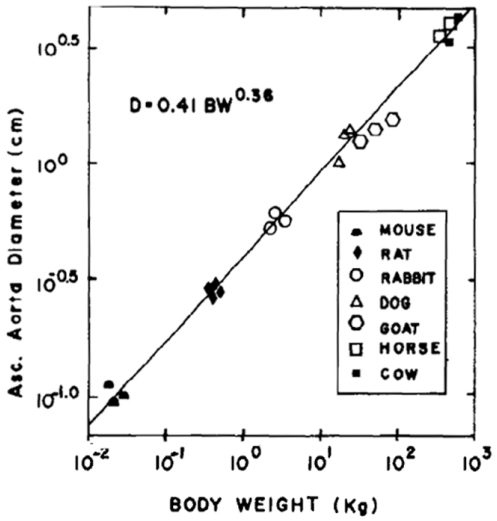


Figure 4.3: Allometric relationship between aortic diameter and body weight for mammalian species.

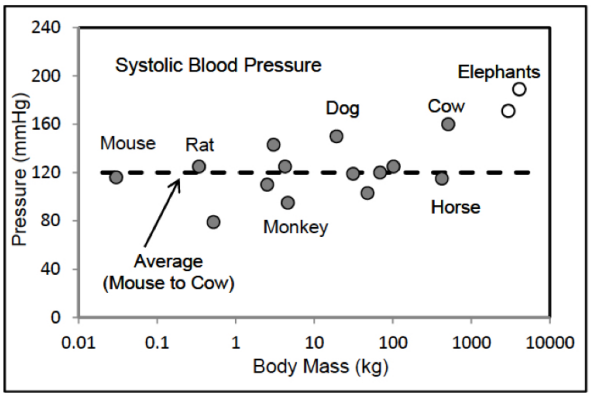


Figure 4.4: Allometric relationship between blood pressure and body mass for mammalian species, showing that blood pressure is constant across species of different sizes.

| **Species** | **Body Mass (kg)** | **Cardiac Output (L/min)** |
|---|---|---|
| Elephant | 2000 | 67 |
| Horse | 400 | 19 |
| Man | 70 | 5 |
| Dog | 20 | 1.8 |
| Rabbit | 3.5 | 0.5 |
| Mouse | 0.25 | 0.06 |
| Tree Shrew | 0.005 | 0.003 |

Table 4.1: Typical values of body mass and cardiac output for a range of mammalian species from allometric scaling.

Therefore, by substituting the relationships for volumetric flow rate ($Q$) and blood vessel diameter ($d$) into the expression for shear stress( $\tau$) one can obtain the relationship

$$\tau \sim \frac{Q}{d^3} = \frac{M^{\frac{3}{4}}}{M^{\frac{9}{8}}} = M^{-\frac{3}{8}} \ . \tag{4.3}$$

This relationship tells us that shear stress decreases with increasing body mass. Therefore, shear stress is not invariant across species.

## 4.3 Experimental Verification of Allometric Scaling

A literature search of relevant work relating allometric scaling of body mass with respect to multiple quantities discussed above reveals convincing correlations between theoretical and observed values. Kleiber's Law, also known as the 3/4 Power Law, is the observation that an animal's metabolic rate scales to the 3/4 power of the animal's mass. The data shown in Figure 4.5 confirms this relationship in over 20 orders of magnitude, from the smallest microbes to the largest mammals.

Additionally, experimental work done by Greve J. M. et al. shows a strong correlation of experimental wall shear stress values with the theoretical wall shear stress relationship developed in the previous section. Figure 4.6, illustrates this correlation across different animal species.

We can also use allometry to think about tensile stress autoregulation of vessel thickness. Since we know that diameter of blood vessels increases with increasing body size, and that blood pressure is invariant across species, wall tension $T = pR$ must also increase with increasing body size. This is confirmed by the empirical data shown in Figure 4.7.

In summary, we have discussed the following global design principles related to cardiovascular structure and function. These relationships will prove important as we think about appropriate mathematical models to choose at different scales in subsequent chapters.

Basic Design Principles:

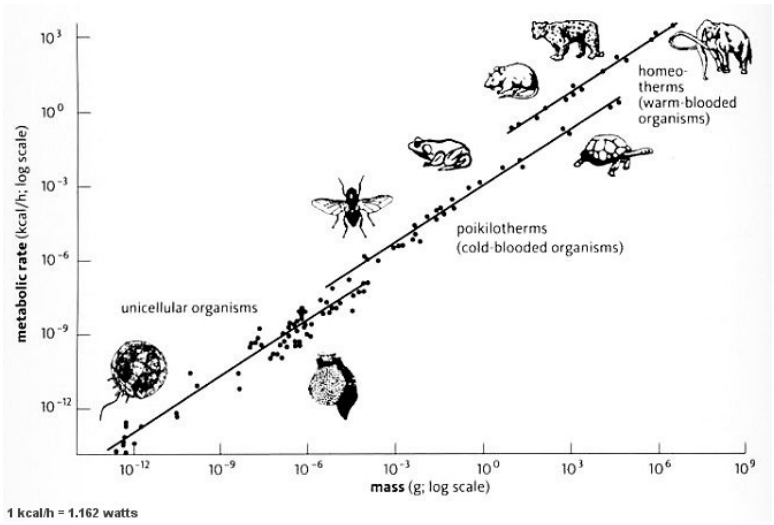


Figure 4.5: Metabolic rate (in Kcal/hr) for a series of organisms ranging from the smallest microbes to the largest mammals as a function of mass (in g), exemplifying the persistence of the $\frac{3}{4}$ power scaling law (the solid lines) over 20 orders of magnitude.

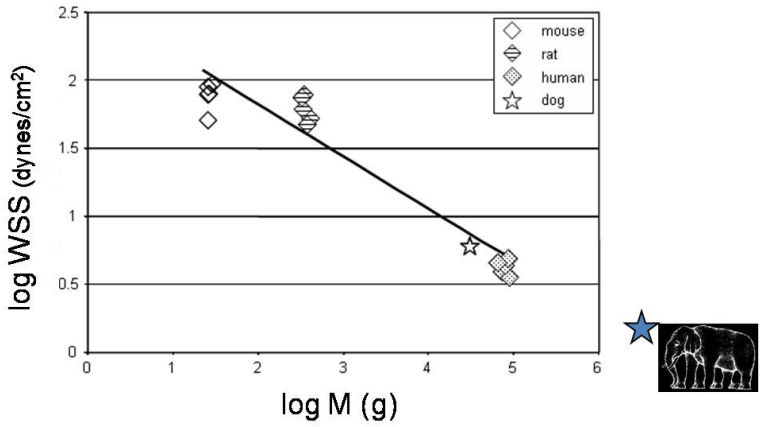


Figure 4.6: Wall shear stress comparison across various species from Greve et al.

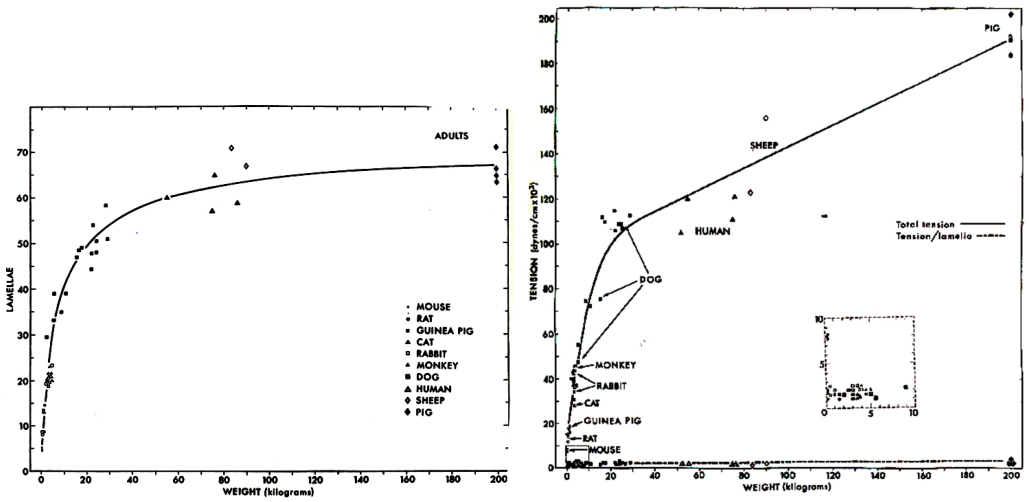


Figure 4.7: Vessel wall thickness (left) and tension (right) vs. body weight for a range of mammalian species.

- Bulk Flow of Fluids
- Hierarchy of vessel sizes
- Area preserving large branches area increasing small branches
- Shear stress autoregulation of vessel diameter
- Tensile stress autoregulation of vessel thickness

## 4.4 Non-dimensional Parameters of Relevance to Blood Flow

Finally, we briefly list several non-dimensional parameters of fluid mechanics that are relevant to the study of blood flow in cardiovascular modeling and experiments.

Reynolds Number:

$$Re = \frac{\text{intertial forces}}{\text{viscous forces}} = \frac{\rho U L}{\mu}$$

Peclet Number:

$$Pe = \frac{\text{advective transport rate}}{\text{diffusive transport rate}} = \frac{LU}{D}$$

Schmidt Number:

$$Sch = \frac{\text{viscous diffusion rate}}{\text{molecular diffusion rate}} = \frac{\nu}{D}$$

Womersley Number:

$$\alpha^2 = \frac{\text{transient inertial force}}{\text{viscous force}} = \frac{\omega L^2}{\nu}$$

## 4.5 Literature Scan

A quick literature scan shows a few interesting papers relating to this topic:

1. Greve, J. M., Les, A. S., Tang, B. T., Blomme, M. T. D., Wilson, N. M., Dalman, R. L., et al. (2006). Allometric scaling of wall shear stress from mice to humans: quantification using cine phase-contrast MRI and computational fluid dynamics. American Journal of Physiology. 291 (4), H1700-H1708.

2. West, G. B., Brown, J. H., & Enquist, B. J. (1997). A General Model for the Origin of Allometric Scaling Laws in Biology. Science. 276 (5309), 122.

3. Small, C. G. (1996). The statistical theory of shape. Springer series in statistics. New York: Springer. item Kleiber, M. (1932). Body size and metabolism. Hilgardia, vol. 6, nr. 11. Berkeley, Calif: Univ. of Calif.

4. Zamir, M. (2000). The physics of pulsatile flow. Biological physics series. New York: AIP Press. 49-57.

# Chapter 5

# Lumped Parameter Modeling

## 5.1 Electrical Analogy

Starting in the 1960s, lumped parameter models of the circulatory system were developed by analogy to electrical circuits. These models have the advantage that they are governed by ordinary differential equations and can be readily solved in near real time on a desktop computer. While they do not provide spatial information, they can be quite complex, providing a surprisingly realistic representation of circulatory dynamics and cardiac function. Lumped parameter models can be used indpenedently or, more commonly, as boundary conditions for 1-D or 3-D simulations.

In this chapter we "lump" the resistive, elastic and inertial properties of blood flow through vessels into electrical elements. Therefore, our circulation circuit becomes analogous to an electric circuit. We then solve the associated set of ordinary differential equations (ODEs) governing the electrical circuit. The values of circuit elements are tuned to match physiologically realistic values for flow, pressure, and other quantities.

We use the basic circuit element relations defining a resistor, capacitor and

inductor, with appropriate analogies to fluid dynamics, as follows:

$$V = IR \quad \Rightarrow \quad \Delta P = QR \tag{5.1}$$

$$V = \frac{d}{dt}LI \quad \Rightarrow \quad \Delta P = \frac{d}{dt}LQ \tag{5.2}$$

$$I = \frac{d}{dt}CV \quad \Rightarrow \quad Q = \frac{d}{dt}CP\ . \tag{5.3}$$

The viscous nature of blood resists flow rate over a given pressure drop. More precisely, from above

$$Q = \frac{\Delta P}{R}\ ,$$

hence increasing resistance leads to a lower flow rate for a fixed pressure gradient. Recall that for Poiseuille flow,

$$R = \frac{8\mu l}{\pi a^4}\ ,$$

where $a$ is the vessel radius and $l$ is the vessel length, so that resistance drops dramatically with increasing vessel radius. Next, the elastic nature of blood vessels, represented by a capacitor, helps to damp out pressure fluctuations. That is

$$\frac{d}{dt}P = \frac{Q}{C}$$

so that the rate of change of pressure becomes smaller as $C$ becomes larger for a fixed flow rate. Likewise, the inertia of blood, represented by an inductor, resist changes of momentum, or alternatively flow rate, since

$$\frac{dQ}{dt} = \frac{\Delta P}{L}$$

so that rate of change of flow rate becomes small as $L$ becomes larger for a fixed pressure gradient.

## 5.2 Windkessel Models

### 5.2.1 2-Element Windkessel model

Windkessel in German means "air chamber," but is generally taken to imply an elastic reservoir. In the realm of the cardiovascular system, the vessels

act as this elastic reservoir. The most basic Windkessel model contains a capacitor and a resistor in parallel. This model accounts for the energy loss due to viscosity and energy storage due to vessel distensibility of the vasculature.

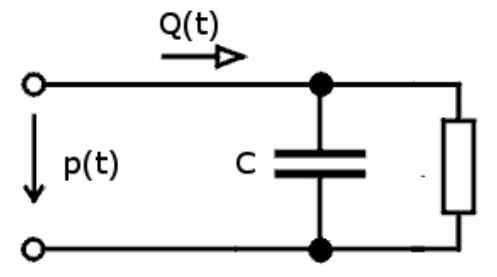


Figure 5.1: Two element Windkessel model

In this case, using Kirchhof's current law (conservation of mass) we have

$$Q = Q_C + Q_R$$

in addition to the element equations

$$Q_C = C\frac{dP}{dt}$$

and

$$p = Q_R R \, .$$

Thus combining the element equations into conservation of mass we have

$$Q = C\frac{dp}{dt} + \frac{p}{R} \, , \tag{5.4}$$

or

$$\frac{dp}{dt} + \frac{p}{RC} = \frac{Q}{C} \, . \tag{5.5}$$

This is an inhomogeneous linear first order ODE. If we ignore the forcing term, the homogeneous equation is

$$\frac{dp}{dt} + \frac{p}{RC} = 0 \tag{5.6}$$

with solution

$$p(t) = p(0)e^{\frac{-t}{RC}} \, .$$

Thus pressure is damped exponentially in time, with "time constant" $\tau = RC$. This is applicable during diastole when $Q = 0$. Consulting most any introductory ODE textbook reveals that a general first order equation

$$\frac{dy}{dx} + P(x)y = S(x)$$

has the unique solution

$$y(x) = e^{-\int P(x)dx} \left[ \int S(x) e^{\int P(x)dx} dx + C \right] . \tag{5.7}$$

For the two element Windkessel model, this implies

$$p(t) = e^{\frac{-t}{RC}} \left[ \int_0^t \frac{Q(s)}{C} e^{\frac{s}{RC}} ds + p(0) \right] .$$

## 5.3 3-Element Windkessel

The 3-element Windkessel model (RCR circuit), is probably most common for its balance of simplicity and accuracy. Note, in this case we have again accounted for the viscous nature of the flow and the elastic nature of the vessels. However, we have added a proximal pressure drop due to a proximal resistance $r$.

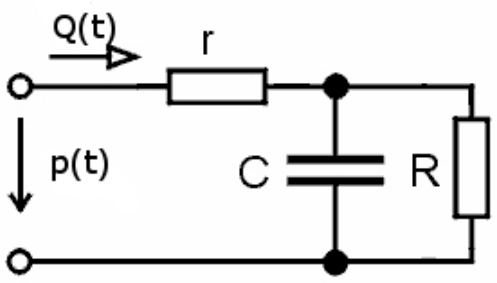


Figure 5.2: Three element Windkessel model

Conservation of mass for this circuit implies

$$Q = Q_r = Q_C + Q_R \tag{5.8}$$

and the element relations are given as

$$Q_C = C\frac{dp_d}{dt} \ , \tag{5.9}$$

$$p - p_d = Q_r r \ , \tag{5.10}$$

and

$$p_d = Q_R R \ , \tag{5.11}$$

where $p - p_d$ is the pressure drop across the proximal resistor.

We can combine these relations into a single ODE. Combing Eqs. (5.9) and (5.10) we obtain

$$Q_C = C\frac{d}{dt}(p - Q_r r) \tag{5.12}$$

Using conservation of mass, Eq. (5.8), this equation becomes

$$Q - Q_R = C\frac{d}{dt}(p - Qr) = C\frac{dp}{dt} - Cr\frac{dQ}{dt} \ . \tag{5.13}$$

Now incorporate Eq. (5.11) to obtain

$$Q - \frac{p_d}{R} = C\frac{dp}{dt} - Cr\frac{dQ}{dt} \tag{5.14}$$

Use again Eq. (5.10) to obtain

$$Q - \frac{p - Qr}{R} = C\frac{dp}{dt} - Cr\frac{dQ}{dt} \ . \tag{5.15}$$

Rearranging we have,

$$\frac{dp}{dt} + \frac{p}{CR} = Q\left[\frac{1}{C} + \frac{r}{CR}\right] + r\frac{dQ}{dt} \ . \tag{5.16}$$

Defining the time constant $\tau = RC$, gives

$$\frac{dp}{dt} + p\frac{1}{\tau} = r\frac{dQ}{dt} + \frac{1}{\tau}(r + R)Q \ . \tag{5.17}$$

By Eq. (5.7), our solution takes the form

$$p(t) = e^{-t/\tau}\left[\int_0^t e^{s/\tau}\left[r\frac{dQ(s)}{ds} + \frac{1}{\tau}(r + R)Q(s)\right]ds + p(0)\right] \ . \tag{5.18}$$

## 5.4 4-Element Windkessel

The four element Windkessel model incorporates the inertia of blood in the proximal circulation by adding a proximal inductor to the 3 element model to model interial effects of the blood.

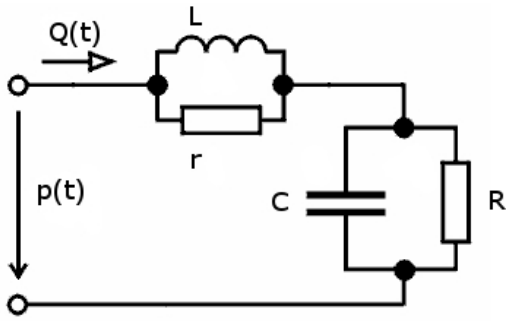


Figure 5.3: Four element Windkessel model

Conservation of mass for this circuit implies

$$Q = Q_r + Q_L = Q_C + Q_R \tag{5.19}$$

and the element relations are given as

$$p - p_d = L\frac{dQ_L}{dt} \,, \tag{5.20}$$

$$p - p_d = Q_r r \,, \tag{5.21}$$

$$Q_C = C\frac{dp_d}{dt} \,, \tag{5.22}$$

$$p_d = Q_R R \,, \tag{5.23}$$

where $p - p_d$ is the pressure drop across the proximal resistor and inductor. Continuity combined with the first two element relations provides the ODE

$$\frac{dQ_L}{dt} + \frac{r}{L}Q_L = \frac{r}{L}Q. \tag{5.24}$$

Continuity combined with the last two element relations provides the ODE

$$\frac{dp_d}{dt} + \frac{p_d}{RC} = \frac{Q}{C} \,. \tag{5.25}$$

These two first order equations are not coupled. Thus each can be solved independently by employing the result of Eq. (5.7). Once those solutions are obtained, $p$, $Q_r$, $Q_R$ or $Q_C$ can be solved easily by the element relations above.

## 5.5 Impedance of the RCR circuit

Since the RCR circuit is common, it is often useful to know the impedance of this circuit. To calculate impedance, $Q$ and $p$ are assumed periodic. Let

$$\omega_k = \frac{2\pi k}{T}, \tag{5.26}$$

where $T$ is the period of heart beat and $k \in \mathbb{N}$. We can therefore represent any periodic $p(t)$ and $Q(t)$ by Fourier series

$$p(t) = \sum_{k=-\infty}^{\infty} p_k e^{i\omega_k t} \tag{5.27}$$

$$Q(t) = \sum_{k=-\infty}^{\infty} Q_k e^{i\omega_k t} \, . \tag{5.28}$$

where $p_k = f(\omega_k)$ and $Q_k = f(\omega_k)$.

Inserting these into our ODE (Eq. 5.17) we have

$$\sum_{k=-\infty}^{\infty} \left\{ i\omega_k p_k + \frac{1}{\tau} p_k - i\omega_k r Q_k - \frac{1}{\tau}(r+R) Q_k \right\} e^{i\omega_k t} = 0 \tag{5.29}$$

Eq. (5.29) holds for all $t$ and $\omega$. That is, you can always find a time and frequency where $e^{i\omega_k t}$ is nonzero. Therefore, the bracketed expression must be zero, i.e.

$$i\omega_k p_k + \frac{1}{\tau} p_k - i\omega_k r Q_k - \frac{1}{\tau}(r+R) Q_k = 0 \tag{5.30}$$

Impedance is defined by the relations $p = ZQ$. With this in mind, we rewrite Eq. (5.30) as

$$p_k \left[ i\omega_k + \frac{1}{\tau} \right] = Q_k \left[ i\omega_k r + \frac{1}{\tau}(r+R) \right] \tag{5.31}$$

and therefore,

$$Z_k = \frac{p_k}{Q_k} \tag{5.32}$$

$$= \frac{i\omega_k r + \frac{1}{\tau}(r+R)}{i\omega_k + \frac{1}{\tau}} \tag{5.33}$$

$$= \frac{i\omega_k rRC + (r+R)}{i\omega_k RC + 1} \tag{5.34}$$

As expected, $Z_k$ is complex and thus we can write as $Z_k = |Z(\omega_k)|\, e^{i\theta(\omega_k)}$ so that

$$|Z(\omega_k)| = \sqrt{\frac{(r+R)^2 + \omega_k^2 (rRC)^2}{1 + \omega_k^2 (RC)^2}}, \tag{5.35}$$

and

$$\theta = \arctan\left(\frac{\omega_k rRC}{r+R}\right) - \arctan\left(\omega_k RC\right) \tag{5.36}$$

$$= \arctan\left(\frac{-CR^2\omega_k}{R + r(C^2R^2\omega_k^2 + 1)}\right). \tag{5.37}$$

Recall that the arctan function is s-shaped and asymptotes to $\pi/2$ on the right and $-\pi/2$ on the left. We can make the following conclusions:

1. $\omega \to 0$ (steady flow)
   $|Z| \to r + R$ two resistors in series
   $\theta \to 0$ pressure and flow in phase

2. $\omega \to \infty$
   $|Z| \to r$
   $\theta \to 0$

3. $0 < \omega < \infty$
   $r \leq |Z| \leq r + R$
   $\theta < 0$

## 5.6 A sample heart model

In this section we derive the equations for a simple one-chambered heart model of the mitral valve and left ventricle.

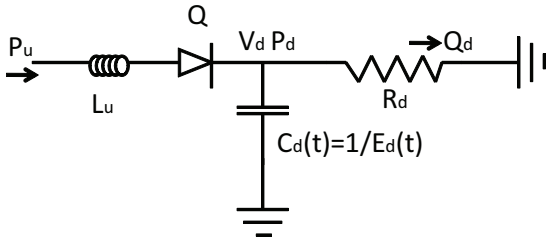


Figure 5.4: Simple heart model

We first define the following variables for use in this model. $P$: pressure, $Q$: flow, $V$: volume, $L$: inductance, $C$: capacitance, $E$: elastance, $R$: resistance

We also assume that values of $P_u$, $L_u$, $R_d$, $E_d$ and $V_{d0}$ are known. The subscript $u$ refers to locations upstream of the valve (in the left atrium) and subscript $d$ refers to locations downstreatm of the valve in the left ventricle. The inductor in this model represents the inertial effects of the blood leaving the left atrium so that

$$\frac{\mathrm{d}Q_v}{\mathrm{d}t} = \frac{1}{L_u}(P_u - P_d). \tag{5.38}$$

The mitral valve is represented by a diode, through which flow goes only in one direction. The atrial pressure must exceed the ventricular pressure so that $P_u > P_d$ for the valve to be open, else the valve is closed.

The capacitor models ventricular filling, relating ventricular pressure and volume through the relationship $P_d = \frac{1}{C_d}(V_d - V_{d0})$, where $V_{d0}$ is the volume of the ventricular chamber at zero pressure. We often refer to the elastance function $E$ as the inverse of capacitance so that $E = 1/C$.

The resistor is modeled as $P_d = Q_d R_d$ and represents viscous losses of blood leaving the left ventricle.

We wish to identify an ODE of the form $\frac{\mathrm{d}y}{\mathrm{d}t} = f(y,t))$. We let our vector of unknowns be

$$y = \begin{Bmatrix} Q_v \\ V_d \end{Bmatrix}. \tag{5.39}$$

Thus we have

$$\frac{\mathrm{d}Q_v}{\mathrm{d}t} = f(Q_v, V_d, t) \tag{5.40}$$

$$\frac{\mathrm{d}V_d}{\mathrm{d}t} = f(Q_v, V_d, t) \tag{5.41}$$

We relate pressure to elastance

$$P_d = E_d(t)\left[V_d - V_{d0}\right]. \tag{5.42}$$

Substituting Eqn.5.42 into Eqn.5.38, we have

$$\frac{\mathrm{d}Q_v}{\mathrm{d}t} = \frac{1}{L_u}\left\{P_u - E_d(t)\left[V_d - V_{d0}\right]\right\} \tag{5.43}$$

for the inductor.

And for the resistor we have

$$Q_d = \frac{P_d}{R_d} = \frac{E_d\left[V_d - V_{d0}\right]}{R_d}. \tag{5.44}$$

Expressing everything in terms of our unknown variables, we have

$$\frac{\mathrm{d}V_d}{\mathrm{d}t} = Q_v - Q_d \longleftarrow \text{diff. in flow thru. valve and downstream} \tag{5.45}$$

$$= Q_v - \frac{E_d(V_d - V_{d0})}{R_d}. \tag{5.46}$$

$$\tag{5.47}$$

And finally we have a set of two ODEs describing our heart model

$$\frac{\mathrm{d}Q_v}{\mathrm{d}t} = \frac{1}{L_u}\left\{P_u - E_d\left[V_d - V_{d0}\right]\right\} \tag{5.48}$$

$$\frac{\mathrm{d}V_d}{\mathrm{d}t} = Q_v - \frac{E_d(V_d - V_{d0})}{R_d}. \tag{5.49}$$

We will solve this system for two cases representing the open and closed states of the mitral valve

1. valve closed
   $Q_v < 0$
   $\rightarrow Q_v = 0$ ($\frac{\mathrm{d}Q}{\mathrm{d}t} = 0$) until valve open
2. valve open
   $P_u > P_d$
   $\rightarrow$ evaluate $Q_v$ until valve close

Numerical solutions for this and more complex LPN models can be obtained using a standard time-integration scheme such as a Runge Kutta method.

Some notes on lumped parameter models:

1. Inductance effects are important in large arteries
2. In general, when resistive losses in large vessels are low, inductance is high, and vice versa.
3. Resistance of vessels can change due to stimuli, leading to contraction or relaxation of smooth muscle cells in the media. One should therefore consider this in model, and incorporate variable resistors depending on external factors. The result may be non-linear circuit equations that should be solved numerically.
4. Pros of lumped parameter modeling include: 1) ODE's in time can be easily solved analytically or numerically. 2) Given appropriate physical parameters, these models have the potential to calculate pressure and flow in real time for clinical application. 3) Can model cardiac function and include large portions of CV system and multiple organs.

5. Cons of lumped parameter modeling include: 1) There is a tenuous relationship between anatomy, fluid and vessel characteristics and lumped parameters constants. 2) Because there is no space variable, there is no wave propagation or reflection, so wave propagation speeds are infinite. 3) Not guaranteed to satisfy conservation of momentum

# Chapter 6

# One dimensional pulsatile flow in deformable vessels

While the lumped parameter models studied in the previous chapter offer an efficient, and often realistic, means to reproduce basic elements of circulatory physiology, there are several drawbacks that call for the use of higher order methods. While lumped models are based on a convenient analogy to electrical circuits, they are not derived from the fundamental conservation equations of mass and momentum used in fluid mechanics. By deriving simple models from these fundamental physical principles, we can capture additional features important to circulatory physiology. Perhaps the most important of these is wave propagation. In this chapter, we derive the one-dimensional equations of fluid flow in deformable vessels. These equations, though more complex to solve than lumped parameter models, offer a relatively efficient means to reproduce realistic wave propagation phenomemon in vascular networks. We note that they can be coupled to both 0D lumped parameter models, and to more complex 3D flow simulations as boundary conditions. Additionally, by linearizing these equations, impedance of vascular networks can be determined.

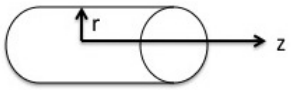


Figure 6.1: Blood vessel modeled as an elastic circular cylindrical pipe

## 6.1 Derivation of the 1-D equations

We begin our derivation of the 1-D equations with the general equations of continuity and momentum conservation of blood flow in cylindrical coordinates, the incompressible Navier-Stokes equations (Equation 2.17), in the axisymmetric tube-shaped geometry shown in Figure 6.1.

Written in cylindrical coordinates, the continuity equation is

$$\frac{\partial u_z}{\partial z} + \frac{1}{r}\frac{\partial}{\partial r}(ru_r) + \frac{1}{r}\frac{\partial}{\partial \theta}(u_\theta) = 0, \tag{6.1}$$

and the axial component ($z$-component) of the momentum equation is

$$\frac{\partial u_z}{\partial t} + u_z\frac{\partial u_z}{\partial z} + u_r\frac{\partial u_z}{\partial r} + \frac{u_\theta}{r}\frac{\partial u_z}{\partial \theta} + \frac{1}{\rho}\frac{\partial p}{\partial z} = \frac{\nu}{r}\frac{\partial}{\partial r}(r\frac{\partial u_z}{\partial r}) + \nu\frac{\partial^2 u_z}{\partial z^2} + \frac{\nu}{r^2}\frac{\partial^2 u_z}{\partial \theta^2}. \tag{6.2}$$

Since the flow is axisymmetic, $u_\theta = 0$ and $\frac{\partial}{\partial \theta} = 0$, so the continuity equation can be simplified to

$$\frac{\partial u_z}{\partial z} + \frac{1}{r}\frac{\partial}{\partial r}(ru_r) = 0. \tag{6.3}$$

And the axial momentum equation becomes

$$\frac{\partial u_z}{\partial t} + u_z\frac{\partial u_z}{\partial z} + u_r\frac{\partial u_z}{\partial r} + \frac{1}{\rho}\frac{\partial p}{\partial z} = \frac{\nu}{r}\frac{\partial}{\partial r}(r\frac{\partial u_z}{\partial r}) + \nu\frac{\partial^2 u_z}{\partial z^2}. \tag{6.4}$$

We note that we do not make a rigid wall assumption, and the blood vessels are assumed to be elastic tubes. We wish to derive a reduced set of 1-D equations in which we solve for the flow rate $Q(z,t)$ and the cross sectional area $A(z,t)$ as a function of one spatial variable $z$ and time $t$. To derive these equations we begin with the following considerations:


Figure 6.2: Cross-sectional area narrowing due to stenosis. These changes may lead to additional pressure losses that may cause deviations from the parabolic flow assumption used in the 1-D equations, and can be accounted for by empirical loss coefficients.

- The 3-D equations are integrated over the vessel cross section.
- We assume the pressure $p(z,t)$ is uniform over the cross section.
- Only axial component of the velocity is considered by assuming a known velocity profile (e.g. parabolic velocity profile).
- The mean flow rate $Q$ and area $A$ are the unknowns.

We note here that in reality the area $A$ may change due to:

- Stenosis: abnormal narrowing in a blood vessel (Figure 6.2.)
- Taper
- Aneurysm: localized, blood-filled dilation of a blood vessel caused by disease or weakening of the vessel wall (Figure 6.3.)
- Changes in elastic properties.

These factors may lead to deviations from the assumed (e.g. parabolic) velocity profile, causing additional pressure losses. We will later revisit modifications of the equations that can account for these factors.

We next consider the boundary conditions at the vessel wall. First, we impose a no slip (zero axial velocity) boundary condition at $r = R$ so that

$$u_z(r = R) = 0. \tag{6.5}$$

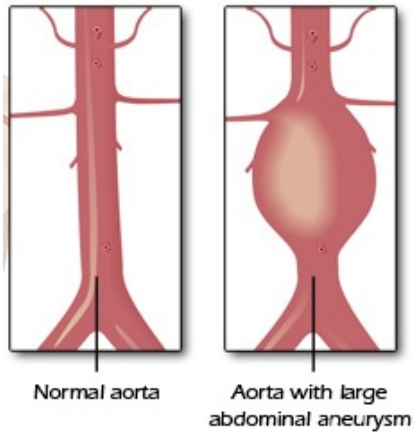


Figure 6.3: Example of cross sectional area changes to do an abdominal aortic aneurysm. These changes may lead to additional pressure losses that may cause deviations from the parabolic flow assumption used in the 1-D equations, and can be accounted for by empirical loss coefficients.

Second, because the walls are elastic, we impose a matching condition and require the radial velocity to be equal to the wall velocity, $\frac{\partial r}{\partial t}|_{r=R}$, giving

$$u_r(r = R) = \frac{\partial r}{\partial t}|_{r=R}. \tag{6.6}$$

Before proceeding further, we recall that integration of the velocity over the vessl cross-section yields the volumetric flow rate

$$Q = 2\pi \int_0^R u_z r dr. \tag{6.7}$$

And, the cross sectional area is $A = \pi R^2$.

To derive the 1-D equations, we integrate Equations 6.3 and 6.4 over the cross-sectional area of the vessel. Our goal is a set of equations in terms of only $Q$ and $A$. We start by integrating the continuity equation. Note that to integrate over the cross section, we must multiply by $2\pi r$, such that

$$\underbrace{2\pi \int_0^R \frac{\partial u_z}{\partial z} r dr}_{1} + \underbrace{2\pi \int_0^R \frac{1}{r}\frac{\partial}{\partial r}(r u_r) r dr}_{2} = 0. \tag{6.8}$$

The individual terms in this equation can be written in terms of flow rate $Q$ and area $A$ as follows:

1. The first term becomes

$$2\pi \int_0^R \frac{\partial u_z}{\partial z} r dr = \frac{\partial}{\partial z} (\underbrace{2\pi \int_0^R u_z r dr}_{Q}) = \frac{\partial Q}{\partial z}. \tag{6.9}$$

2. The second term becomes

$$\begin{aligned} 2\pi \int_0^R \frac{1}{r} \frac{\partial}{\partial r} (r u_r) r dr &= 2\pi \int_0^R \frac{\partial}{\partial r} (r u_r) dr && (6.10)\\ &= 2\pi r u_r \,|_0^R && (6.11)\\ &= 2\pi R \frac{\partial R}{\partial t} && (6.12)\\ &= \frac{\partial}{\partial t} (\pi R^2) && (6.13)\\ &= \frac{\partial A}{\partial t}. && (6.14) \end{aligned}$$

So the final 1-D equation for conservation of mass of the blood flow written in terms of flow rate and area is

$$\frac{\partial A}{\partial t} + \frac{\partial Q}{\partial z} = 0. \tag{6.15}$$

The second relation between flow rate and cross sectional area comes from the integration of the axial momentum equation multiplied by $2\pi r$,

$$\underbrace{2\pi \int_0^R \frac{\partial u_z}{\partial t} r dr}_{1} + \underbrace{2\pi \int_0^R u_z \frac{\partial u_z}{\partial z} r dr}_{2} + \underbrace{2\pi \int_0^R u_r \frac{\partial u_z}{\partial r} r dr}_{3} \tag{6.16}$$

$$+ \underbrace{2\pi \int_0^R \frac{1}{\rho} \frac{\partial p}{\partial z} r dr}_{4} = \underbrace{2\pi \int_0^R \frac{\nu}{r} \frac{\partial}{\partial r} (r \frac{\partial u_z}{\partial r}) r dr}_{5} + \underbrace{2\pi \int_0^R \nu \frac{\partial^2 u_z}{\partial z^2} r dr}_{6}. \tag{6.17}$$

We now integrate each individual term in the above equation:

1. The first term gives

$$2\pi \int_0^R \frac{\partial u_z}{\partial t} r dr = \frac{\partial}{\partial t}\left(2\pi \int_0^R u_z dr\right) \tag{6.18}$$

$$= \frac{\partial Q}{\partial t}. \tag{6.19}$$

2. The second term gives

$$2\pi \int_0^R u_z \frac{\partial u_z}{\partial z} r dr = \pi \int_0^R \frac{\partial ({u_z}^2)}{\partial z} r dr \tag{6.20}$$

   For now we leave this term in this form.

3. To re-write the third term in the same for as the rest of the equation, and to later simplify the momentum equation, we use the chain rule:

$$\frac{\partial}{\partial r}\left(r u_r u_z\right) = r u_r \frac{\partial u_z}{\partial r} + u_z \frac{\partial (r u_r)}{\partial r}. \tag{6.21}$$

   Therefore, the term we are considering can be written as follows:

$$r u_r \frac{\partial u_z}{\partial r} = \frac{\partial}{\partial r}(r u_r u_z) - u_z \frac{\partial (r u_r)}{\partial r}. \tag{6.22}$$

   Now using the continuity equation,

$$\frac{\partial u_z}{\partial z} + \frac{1}{r}\frac{\partial r u_r}{\partial r} = 0, \tag{6.23}$$

   and substituting, we obtain

$$r u_r \frac{\partial u_z}{\partial r} = \frac{\partial}{\partial r}(r u_r u_z) + u_z r \frac{\partial u_z}{\partial z}. \tag{6.24}$$

   With this, we can now write the third term as

$$2\pi \int_0^R u_r \frac{\partial u_z}{\partial r} r dr = 2\pi \int_0^R \frac{\partial r u_r u_z}{\partial r} dr + 2\pi \int_0^R u_z r \frac{\partial u_z}{\partial z} dr \tag{6.25}$$

$$= \underbrace{2\pi r u_r u_z|_0^R}_{=0} + \pi \int_0^R \frac{\partial (u_z)^2}{\partial z} r dr. \tag{6.26}$$

Applying the no slip boundary condition, $u_z(r = R) = 0$, the first term in the above expression is

$$2\pi r u_r u_z|_0^R = 2\pi R u_r(r = R)u_z(r = R) - 0 = 0, \tag{6.27}$$

and we now have

$$2\pi \int_0^R u_r \frac{\partial u_z}{\partial r} r dr = \pi \int_0^R \frac{\partial (u_z)^2}{\partial z} r dr, \tag{6.28}$$

which matches what we obtained for the second term.

4. The pressure is assumed to be constant across the vessel cross-section, therefore we consider the mean pressure $P$. Then the fourth term can be written as follows:

$$\begin{aligned} 2\pi \int_0^R \frac{1}{\rho}\frac{\partial P}{\partial z} r dr &= \frac{1}{\rho}\frac{\partial P}{\partial z} \underbrace{2\pi \int_0^R r dr}_{A} && (6.29) \\ &= \frac{A}{\rho}\frac{\partial P}{\partial z}. && (6.30) \end{aligned}$$

5. The fifth term now becomes

$$\begin{aligned} 2\pi \int_0^R \frac{\nu}{r}\frac{\partial}{\partial r}(r\frac{\partial u_z}{\partial r}) r dr &= 2\pi\nu \left[ r\frac{\partial u_z}{\partial r} \right]_0^R && (6.31) \\ &= 2\pi\nu R \frac{\partial u_z}{\partial r}\bigg|_{r=R}, && (6.32) \end{aligned}$$

which we leave in this form for now.

6. Finally, the sixth term is

$$\begin{aligned} 2\pi \int_0^R \nu \frac{\partial^2 u_z}{\partial z^2} r dr &= \nu 2\pi \frac{\partial^2}{\partial z^2} \int_0^R u_z r dr && (6.33) \\ &= \nu \frac{\partial^2 Q}{\partial z^2}. && (6.34) \end{aligned}$$

Putting together all six terms above, we obtain the following expression

$$\underbrace{\frac{\partial Q}{\partial t}}_{1} + \underbrace{2\pi\frac{\partial}{\partial z}\int_0^R {u_z}^2 r dr}_{2+3} + \underbrace{\frac{A}{\rho}\frac{\partial P}{\partial z}}_{4} = \underbrace{2\pi\nu R\frac{\partial u_z}{\partial r}\bigg|_{r=R}}_{5} + \underbrace{\nu\frac{\partial^2 Q}{\partial z^2}}_{6}. \tag{6.35}$$

We note that the above expression still contains two terms that depend on $u_z$. To obtain a final set of equations in terms of only $Q$ and $A$, we must now assume a velocity profile.

## 6.2 Assumption of a parabolic velocity profile

We have now arrived at an expression for the momentum equation, but there are remaining terms containing velocity. To obtain an equation in terms of only $Q$ and $A$, we now assume a parabolic velocity profile, using the Poiseuille solution for fully developed pipe flow derived in Section 3.2. A general parabolic velocity profile can be written as

$$u_z = c_1 r^2 + c_2 r + c_3. \tag{6.36}$$

We apply two boundary conditions:

1. No-slip boundary condition: $u_z = 0$ at $r = R$.
2. Maximum velocity at the center of the vessel: $\frac{\partial u_z}{\partial r} = 0$ at $r = 0$.

Applying these boundary conditions, we solve for the constants contained in the above expression for axial velocity. From the second boundary condition we have

$$\frac{\partial u_z}{\partial r} = 2c_1 r + c_2|_{r=0} = 0 \Rightarrow c_2 = 0. \tag{6.37}$$

The first boundary condition gives

$$u_z|_{r=R} = c_1 R^2 + c_2 R + c_3 = 0,$$

and knowing that $c_2 = 0$ we have

$$\Rightarrow c_3 = -c_1 R^2. \tag{6.38}$$

Combining these results, we can write $u_z$ in terms of $c_1$ as

$$u_z = -c_1(R^2 - r^2). \tag{6.39}$$

We recall the flow rate

$$Q = 2\pi \int_0^R u_z r dr. \tag{6.40}$$

Substituting the expression of the velocity as a function of $c_1$ we have

$$\begin{aligned} Q &= 2\pi \int_0^R -c_1(R^2 - r^2) r dr = -2\pi c_1 (R^2 \frac{r^2}{2} + c_1 \frac{r^4}{4}) \Big|_0^R & (6.41) \\ &= 2\pi(-c_1 \frac{R^4}{2} + c_1 \frac{R^4}{4}) = -2\pi c_1 \frac{R^4}{4}, & (6.42) \end{aligned}$$

and recalling that $A = \pi R^2$ we have

$$Q = -\frac{c_1 A R^2}{2}. \tag{6.43}$$

Therefore we can relate velocity $u_z$ to flow rate $Q$ by

$$u_z = \frac{2Q}{AR^2}(R^2 - r^2). \tag{6.44}$$

We now revisit terms 2 and 3 in our 1-D momentum equation, and rewrite them in terms of $Q$ and $A$, giving

$$\begin{aligned} 2\pi \frac{\partial}{\partial z} \int_0^R u_z^2 r dr &= 2\pi \frac{\partial}{\partial z} \int_0^R \left( \frac{2Q}{AR^2} \right)^2 (R^2 - r^2)^2 r dr & (6.45) \\ &= 2\pi \frac{\partial}{\partial z} \int_0^R \left( \frac{2Q}{AR^2} \right)^2 (R^4 - 2R^2 r^2 + r^4) r dr. & (6.46) \end{aligned}$$

Evaluating the above integral we have,

$$\begin{aligned} 2\pi \frac{\partial}{\partial z} \int_0^R u_z^2 r dr &= \frac{8\pi}{A^2 R^4} Q^2 \frac{\partial}{\partial z} (\frac{R^6}{2} - 2\frac{R^6}{4} + \frac{R^6}{6}) & (6.47) \\ &= \frac{\partial}{\partial z} \left( \frac{8\pi Q^2 R^6}{6A^2 R^4} \right) & (6.48) \\ &= \frac{\partial}{\partial z} \left( \frac{4Q^2}{3A} \right). & (6.49) \end{aligned}$$

We also revisit term 5 from our 1-D momentum equation, and rewrite it in terms of $Q$ and $A$, giving

$$2\pi\nu\left(r\frac{\partial u_z}{\partial r}\right)\Big|_{r=R} = 2\pi\nu R\frac{2Q}{AR^2}(-2R) \tag{6.50}$$

$$= -8\pi\nu\frac{Q}{A}. \tag{6.51}$$

Finally, combining the above terms, we obtain the final form of the 1-D equations for conservation of mass and momentum in terms of flow rate and area, with an assumed parabolic flow profile, as follows.

Conservation of mass equation:

$$\frac{\partial A}{\partial t} + \frac{\partial Q}{\partial z} = 0. \tag{6.52}$$

Conservation of momentum equation:

$$\frac{\partial Q}{\partial t} + \frac{\partial}{\partial z}\left(\frac{4}{3}\frac{Q^2}{A}\right) + \frac{A}{\rho}\frac{\partial P}{\partial z} = -8\pi\nu\frac{Q}{A} + \nu\frac{\partial^2 Q}{\partial z^2}. \tag{6.53}$$

The above equations contain three unknown variables: $Q$, $A$ and $P$. So, we have two equations and three unknowns. To close this system, we need a constitutive relation between pressure and wall deformation. There are several options for constitutive relationships that have been reported in the literature. We list two examples below:

1. Olufsen Model. This model, described by Olufsen in [54], can be derived from Laplace's law, which gives us an expression for the circumferential stress

$$\tau_\theta = \frac{R(P - P_0)}{h} = \frac{E_\theta}{1 - \sigma_x\sigma_\theta}\frac{R - R_0}{R_0}, \tag{6.54}$$

where $E_\theta$ is the Young's modulus in the circumferential direction and $\sigma_\theta$ and $\sigma_x$ are the Poisson ratios in the circumferential and longitudinal directions, both equal to 0.5 for an incompressible material. Note that here we have assumed the arterial vessel is circular, the walls are thin

$(h/r \ll 1)$, the loading and deformation are axisymmetric, and the vessel is tethered in the longitudinal direction. Solving for excess pressure $P - P_0$, dropping the subscript on $E_\theta$, and using $A_0 = \pi r_0^2$ then yields

$$P - P_0 = \frac{4}{3}\frac{Eh}{R_0}\left(1 - \sqrt{\frac{A_0}{A}}\right). \tag{6.55}$$

where $P_0$ is the pressure in the reference state, $E$ is the Young's modulus of the vessel wall, $h_0$ is the wall thickness in the reference state, $R_0$ is the radius of the blood vessel in the reference state, and $A_0$ is the vessel cross sectional area in the reference state. We note that in this equation the area $A$ becomes infinite at a finite transmural pressure. Real arteries resist this tendency by having a nonlinear Young's modulus that increases with increasing strain. An empirical relation to determine $\frac{Eh}{R_0}$ as a function of the radius in the reference state can be determined from experiemntal data as

$$\frac{Eh}{R_0} = k_1 e^{k_2 R_0} + k_3 \tag{6.56}$$

where data from Westerhof [69], Stergiopulos [61], and Segers [59] has been used to determine the constants $k_1 = 2.00 \times 10^7 \mathrm{g} \cdot \mathrm{s}^{-2} \cdot \mathrm{cm}^{-1}$, $k_2 = -22.53 \mathrm{cm}^{-1}$, and $k_3 = 8.65 \times 10^5 \mathrm{g} \cdot \mathrm{s}^{-2} \cdot \mathrm{cm}^{-1}$.

2. Kassab A similar derivation from Laplace's law is described by Huo and Kassab [28]. Beginning again with Laplace's law and time time assuming a linear stress strain relationship gives

$$P - P_0 = \frac{Eh_0}{R_0}\left(\frac{A}{A_0} - 1\right). \tag{6.57}$$

The above constitutive laws relate the change in cross sectional area of the vessel in response to changing pressure loads, which depends on the material properties, including modulus and thickness, of the vessel wall. These expressions will be used to determine wave propagation speeds in the next chapter.

### 6.2.1 Generalization to other profile functions

While our derivation assumed a parabolic velocity profile, we can generalize the 1-D equations to allow for a general family of velocity profiles following the original derivation of Hughes and Lubliner (1973) [26]. We start with the equation for conservation of mass, and allowing for mass flux across the porous walls $\psi$, we have

$$\frac{\partial A}{\partial t} + \frac{\partial}{\partial z}(Q) + \psi = 0. \tag{6.58}$$

We assume a general profile function

$$u_z = \phi \bar{u}, \tag{6.59}$$

where $\bar{u}$ is the unknown mean velocity, We can also generalize the equation for conservation of momentum to give

$$\frac{\partial Q}{\partial t} + \frac{\partial}{\partial z}\left((1+\delta)\frac{Q^2}{A}\right) + \frac{A}{\rho}\frac{\partial P}{\partial z} = Af + N\frac{Q}{A} + \nu\frac{\partial^2 Q}{\partial z^2}, \tag{6.60}$$

where $N$ simplifies to $N = -8\pi\nu$ for parabolic flow, and $f$ is a body force.

We define a general velocity profile function $\phi$ that depends on the radius of the wall and an order $n$ as

$$\phi = \left(\frac{n+2}{n}\right)\left(1 - (r')^n\right), \tag{6.61}$$

and an equation for $\delta$ as

$$\delta = \frac{1}{A}\int_A (\phi^2 - 1)da \rightarrow \delta = \frac{1}{n+1}. \tag{6.62}$$

For the case of a parabolic profile, in which $n = 2$, the general 1-D equations simplify to Equations 6.53 and 6.52. These equations can be solved numerically using standard approaches, including finite difference methods, finite element methods, discontinuous Galerkin methods, or the method of characteristics. Because they have been greatly simplified to include only one spatial dimension, they can be solved efficiently in near-real time. In addition, we note that these equations offer a nice model problem for the full 3-D equations, capturing much of the interesting non-linearity and wave propagation phenomena found in the full equations. Similar equations have been derived in other fields of fluid mechanics involving flow in networks of pipes or cracks.

# Chapter 7

# Impedance of vascular networks

In the previous chapter, we derived the 1-D equations governing blood flow in an elastic vessel. We now linearize these equations to study wave propagation, and introduce the concepts of resistance and impedance. This will be useful for determining the impedance of networks of vessels and vascular trees. First, we observe the following properties of the 1-D equations that motivate our further developments. First, the full 1-D equations are non-linear and must be solved numerically. Second, they are useful for investigating pulse propagation in a single tube. We note that these equations do not produced local details of the flow field such as recirculation patters, but that they could be coupled to 3-D simulations as a boundary condition.

If we want to understand flow in a network of vessels, it is often desirable to further simplify the 1-D equations to consider the bulk effect of wave propagation. The linearization of the 1-D equations results in a simplified relation between flow and pressure that can be used to understand wave propagation in a network of vessels. This process also produces bulk resistance and impedance properties of trees that are useful as boundary conditions for full 3-D or 1-D simulations. In this chapter, we will derive this simplified expression, and demonstrate its application to vascular networks.

## 7.1 Linearization of the 1-D equations

To arrive at a simplified set of 1-D equations, we will perform a scaling analysis, starting with the Navier-Stokes equations in cylindrical coordinates and neglecting the $\theta$ components (e.g. assuming symmetry) and gravity. The continuity equation (Eq. 3.2) in cylindrical coordinates (Eq. 2.24) is given by

$$\frac{1}{r}\frac{\partial}{\partial r}\left(rv_r\right) + \frac{\partial}{\partial z}\left(v_z\right) = 0. \tag{7.1}$$

The $r$ and $z$ components of the momentum equation written in cylindrical coordinates are
$r$-component:

$$\frac{\partial v_r}{\partial t} + v_r\frac{\partial v_r}{\partial r} + v_z\frac{\partial v_r}{\partial z} = -\frac{1}{\rho}\frac{\partial p}{\partial r} + \nu\left(\frac{\partial}{\partial r}\left(\frac{1}{r}\frac{\partial}{\partial r}(rv_r)\right) + \frac{\partial^2 v_r}{\partial z^2}\right) \tag{7.2}$$

$z$-component:

$$\frac{\partial v_z}{\partial t} + v_r\frac{\partial v_z}{\partial r} + v_z\frac{\partial v_z}{\partial z} = -\frac{1}{\rho}\frac{\partial p}{\partial z} + \nu\left(\frac{1}{r}\frac{\partial}{\partial r}\left(r\frac{\partial v_z}{\partial r}\right) + \frac{\partial^2 v_z}{\partial z^2}\right). \tag{7.3}$$

We will now perform a scaling analysis by non-dimensionalizing these equations using appropriate time and length scales for all variables in the equations above. We make the following choices for non-dimensionalization:

$$\begin{aligned} r^* &= \frac{r}{R_0} \\ z^* &= zk_r \\ v_z^* &= \frac{v_z}{V} \\ t^* &= k_r ct \\ P^* &= \frac{P}{\rho V c} \end{aligned}$$

where $k_r$ is the real part of the wavenumber, $V$ is a characteristic mean axial velocity, and c is the wavespeed. Then from continuity we find a normalization for radial velocity

$$v_r^* = \left(\frac{v_r}{V}\right)\left(\frac{1}{k_r R_0}\right). \tag{7.5}$$

Substitution of all normalized variable definitions into equations yields non-dimensional conservation of mass equation

$$\frac{1}{r^*}\frac{\partial}{\partial r^*}\left(r^* v_r^*\right) + \frac{\partial}{\partial z^*}\left(v_z^*\right) = 0. \tag{7.6}$$

and non-dimensional conservation of momentum equations for the $r$-component

$$\frac{\partial v_r^*}{\partial t^*} + \frac{V}{c}\left(v_r^*\frac{\partial v_r^*}{\partial r^*} + v_z^*\frac{\partial v_r^*}{\partial z^*}\right) = -\frac{1}{k_r^2 R_0^2}\frac{\partial p^*}{\partial r^*} + \frac{1}{\alpha^2}\left(\frac{\partial}{\partial r^*}\left(\frac{1}{r^*}\frac{\partial}{\partial r^*}(r^* v_r^*)\right) + k_r^2 R_0^2 \frac{\partial^2 v_r^*}{\partial z^{*2}}\right) \tag{7.7}$$

and the $z$-component

$$\frac{\partial v_z^*}{\partial t^*} + \frac{V}{c}\left(v_r^*\frac{\partial v_z^*}{\partial r^*} + v_z^*\frac{\partial v_z^*}{\partial z^*}\right) = -\frac{\partial p^*}{\partial z^*} + \frac{1}{\alpha^2}\left(\frac{1}{r^*}\frac{\partial}{\partial r^*}\left(r^*\frac{\partial v_z^*}{\partial r^*}\right) + R_0^2 k_r^2 \frac{\partial^2 v_z^*}{\partial z^{*2}}\right). \tag{7.8}$$

From the above equations, we can define the following non-dimensional quantities that have emerged

$$\alpha = R_0\sqrt{\omega/\nu} \tag{7.9}$$

$$S = V/c \tag{7.10}$$

$$G = R_0 k_r = 2\pi R_0/\lambda \tag{7.11}$$

where $\lambda$ is a wavelength equal to $2\pi/k_r$. We now assume that the wavespeed $c$ is much faster than the flow velocity $V$ so that

$$S = V/c \ll 1. \tag{7.12}$$

We also assume that the wavelength $\lambda$ is much larger than the vessel radius $R_0$ so that

$$G^2 = (2\pi R_0/\lambda)^2 \ll 1, \tag{7.13}$$

With these assumptions from our scaling analysis, we are able to neglect several terms in the Navier stokes equations. Then putting the equations back into dimensional form we have a reduced set of equations

$$\frac{\partial p}{\partial r} = 0 \tag{7.14}$$

$$\frac{\partial v_z}{\partial t} = -\frac{1}{\rho}\frac{\partial p}{\partial z} + \nu\frac{1}{r}\frac{\partial}{\partial r}\left(r\frac{\partial v_z}{\partial r}\right) \tag{7.15}$$

$$\frac{1}{r}\frac{\partial}{\partial r}(rv_r) + \frac{\partial v_z}{\partial z} = 0. \tag{7.16}$$

Integrating the above reduced equations across the vessel cross-section following the method in the previous chapter, we arrive at the linearized continuity equation

$$\frac{\partial A}{\partial t} + \frac{\partial Q}{\partial z} = 0, \tag{7.17}$$

and momentum equation

$$\frac{\partial Q}{\partial t} + \frac{A_0}{\rho}\frac{\partial P}{\partial z} = N\frac{Q}{A_0}\ . \tag{7.18}$$

where $N = -8\pi\nu$ for the case of a parabolic profile assumption. We note that this linearization is valid when the wave speed, defined below, is much greater than the mean velocity, as is typically the case in the vascular system.

We will now show that the continuity and momentum equations combine to form the classic (damped) wave equation. With this in mind, we define the wave speed, $c_0$, by

$$c_0^2 = \frac{A_0}{\rho}\frac{\partial P}{\partial A}. \tag{7.19}$$

By the chain rule and Eq. (7.19),

$$\frac{\partial A}{\partial t} = \frac{\partial A}{\partial P}\frac{\partial P}{\partial t} = \frac{A_0}{\rho c_0^2}\frac{\partial P}{\partial t}. \tag{7.20}$$

The continuity equation can then be written as

$$\frac{\partial P}{\partial t} + \frac{\rho c_0^2}{A_0}\frac{\partial Q}{\partial z} = 0. \tag{7.21}$$

Now, we differentiate Eqns. (7.18) and (7.21) as follows

$$\frac{\partial}{\partial z}(7.21): \qquad \tfrac{\partial^2 P}{\partial t\partial z} + \tfrac{\rho c_0^2}{A_0}\tfrac{\partial^2 Q}{\partial z^2} = 0 \tag{7.22}$$

$$\frac{\partial}{\partial t}(7.18): \quad \tfrac{\partial^2 Q}{\partial t^2} + \tfrac{A_0}{\rho}\tfrac{\partial^2 P}{\partial t\partial z} - \tfrac{N}{A_0}\tfrac{\partial Q}{\partial t} = 0. \tag{7.23}$$

Combining these, we obtain

$$\frac{\partial^2 Q}{\partial t^2} = c_0^2 \frac{\partial^2 Q}{\partial z^2} + \frac{N}{A_0}\frac{\partial Q}{\partial t}. \tag{7.24}$$

This is the classic homogeneous damped wave equation, which we can re-write as

$$\frac{\partial^2 Q}{\partial t^2} = c_0^2 \frac{\partial^2 Q}{\partial z^2} - f_0 \frac{\partial Q}{\partial t}, \tag{7.25}$$

where

$$f_0 = \frac{-N}{A_0} = \frac{8\pi\nu}{A_0}$$

for a parabolic profile. Note, if $\nu = 0$, we have no viscosity and hence no damping.

Because the wave equation is linear, we can now assume periodic solutions in time of the form

$$P(z,t) = P_1(z)e^{i\omega t} \tag{7.26}$$

$$Q(z,t) = Q_1(z)e^{i\omega t}\ . \tag{7.27}$$

We note that it may appear we haven't allowed for a phase difference between pressure and flow rate. However, if we let $Q_1(z)$ (and/or $P_1(z)$) be complex, then phase differences can be accounted for.

Plugging $Q(z,t)$ this into the wave equation, and canceling the common factor $e^{i\omega t}$, we have

$$(i\omega)^2 Q_1(z) = c_0^2 Q_1''(z) - i\omega f_0 Q_1(z), \tag{7.28}$$

or upon reordering terms

$$Q_1''(z) - \frac{1}{c_0^2}(i\omega f_0 - \omega^2)Q_1(z) = 0. \tag{7.29}$$

We now let

$$\lambda^2 = \frac{1}{c_0^2}(i\omega f_0 - \omega^2) \tag{7.30}$$

so that we obtain a second order ordinary differential equation

$$Q_1''(z) - \lambda^2 Q_1(z) = 0. \tag{7.31}$$

This is a classic eigenvalue problem, with eigenvalue $\lambda$. The general solution is:

$$Q_1(z) = C_1 e^{-\lambda z} + C_2 e^{\lambda z}. \tag{7.32}$$

From continuity, Eq. (7.21), we can also obtain an expression for the pressure

$$P_1(z) i\omega e^{i\omega t} + \frac{\rho c_o^2}{A_0} e^{i\omega t} \lambda(-C_1 e^{-\lambda z} + C_2 e^{\lambda z}) = 0, \tag{7.33}$$

or upon rearranging,

$$P_1(z) = -\frac{\rho {c_0}^2 \lambda}{i\omega A_0}(-C_1 e^{-\lambda z} + C_2 e^{\lambda z}). \tag{7.34}$$

Now let us consider flow through a vessel of length $L$ where we assume the inflow rate and outflow impedance are known, so the boundary conditions are

$$Q_1(0) = Q_0, \tag{7.35}$$

$$P(L) - Z_T Q(L) = 0, \tag{7.36}$$

where

$$Z_T = \text{terminal impedance} = \frac{P(L)}{Q(L)}. \tag{7.37}$$

We can think of the impedance is the opposition (or resistance) to flow as a function of frequency. Since we assumed $Q_1(z)$ (and/or $P_1(z)$) can be complex, then so can the impedance.

To find $C_1$ and $C_2$ we apply the boundary conditions to obtain

$$Q(0) = Q_0 = C_1 + C_2, \tag{7.38}$$

$$P(L) - Z_T \cdot Q(L) = 0, \tag{7.39}$$

where

$$P(L) = -\frac{\rho {c_0}^2 \lambda}{i\omega A_0}(-C_1 e^{-\lambda L} + C_2 e^{\lambda L}), \tag{7.40}$$

$$Q(L) = C_1 e^{-\lambda L} + C_2 e^{\lambda L}. \tag{7.41}$$

We now define the characteristic impedance as

$$Z_0 = \frac{\rho c_0^2 \lambda}{i\omega A_0}, \tag{7.42}$$

so

$$\left.\begin{array}{l} P(L) = Z_0(C_1 e^{-\lambda L} - C_2 e^{\lambda L}) \\ P(L) - Z_T Q(L) = 0 \end{array}\right\} \Rightarrow Z_0(C_1 e^{-\lambda L} - C_2 e^{\lambda L}) - Z_T(C_1 e^{-\lambda L} + C_2 e^{\lambda L}) = 0. \tag{7.43}$$

Combining terms we obtain

$$(Z_0 - Z_T)C_1 e^{-\lambda L} - (Z_0 + Z_T)C_2 e^{\lambda L} = 0. \tag{7.44}$$

We now define the reflection coefficient as

$$\Gamma = \frac{Z_0 - Z_T}{Z_0 + Z_T}. \tag{7.45}$$

The reflection coefficient shows the influence on the reflection of traveling waves such that

- If $Z_{\mathrm{T}} = Z_0 \Rightarrow \Gamma = 0 \Rightarrow$ No reflection.
- If $\Gamma = 1 \Rightarrow$ Complete reflection (tube with a closed end).

Now we have two equations for $C_1$ and $C_2$:

$$Q_0 = C_1 + C_2, \tag{7.46}$$

$$\Gamma C_1 e^{-\lambda L} - C_2 e^{\lambda L} = 0, \tag{7.47}$$

which we can write as a system of equations

$$\left[\begin{array}{cc} 1 & 1 \\ \Gamma e^{-\lambda L} & -e^{\lambda L} \end{array}\right] \cdot \left\{\begin{array}{c} C_1 \\ C_2 \end{array}\right\} = \left\{\begin{array}{c} Q_0 \\ 0 \end{array}\right\}, \tag{7.48}$$

and invert to obtain

$$\left\{\begin{array}{c} C_1 \\ C_2 \end{array}\right\} = \frac{Q_0}{1 + \Gamma e^{-2\lambda L}} \cdot \left\{\begin{array}{c} 1 \\ \Gamma e^{-2\lambda L} \end{array}\right\} \tag{7.49}$$

such that the solution for flow and pressure amplitude becomes

$$Q(z) = \frac{Q_0}{1 + \Gamma e^{-2\lambda L}} \cdot [e^{-\lambda z} + \Gamma e^{\lambda(z-2L)}] \tag{7.50}$$

$$P(z) = \frac{Z_0 Q_0}{1 + \Gamma e^{-2\lambda L}} \cdot [e^{-\lambda z} - \Gamma e^{\lambda(z-2L)}]. \tag{7.51}$$

Finally, we define the input impedance (at z = 0) as

$$Z_i = \frac{P(0)}{Q(0)} = Z_0 \cdot \frac{1 - \Gamma e^{-2\lambda L}}{1 + \Gamma e^{-2\lambda L}}. \tag{7.52}$$

## 7.2 Impedance of Vascular networks

We now wish to use the linearized 1-D equations to determine the impedance (and hence the wave propagation characteristics) of a network of vessels. We are interested in solving the following problem.

Given the terminal impedance, $Z_T$, at the end points of the tree, and the characteristic impedance, $Z_0$, for each vessel, we want to find the input impedance of the tree.

We will illustrate this problem using a simple vessel bifurcation, which can later be extended to larger vascular networks. Recall that the input impedance is

$$Z_0 = \frac{\rho c_0^2 \lambda}{i\omega A_0} \tag{7.53}$$

where the eigenvalue of our system was

$$\lambda^2 = \frac{1}{c_0^2} \cdot (i\omega f_0 - \omega^2). \tag{7.54}$$

Also recall that for inviscid flow, $f_0 = 0$. Thus if we ignore viscosity, we have a dominant eigenvalue given by

$$\lambda^2 = -\frac{\omega^2}{c_0^2}, \tag{7.55}$$

and characteristic impedance

$$Z_0 = \frac{\rho c_0}{A}. \tag{7.56}$$

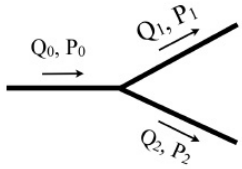


Figure 7.1: Parent branch separating into two child branches (bifurcation)

In practice, the solution of these equations requires conditions to be satisfied at a bifurcation, as shown in Figure 7.1. When we reach a junction, where the blood vessel bifurcates into two child branches, we apply conservation of mass so that

$$Q_0 = Q_1 + Q_2, \tag{7.57}$$

and continuity of pressure so that

$$P_0 = P_1 = P_2. \tag{7.58}$$

A time-dependent inflow boundary condition can be represented by:

$$Q(z_{in}, t) = Q^{in}(t) \tag{7.59}$$

We also recall the concept of Ohm's Law, in which we make an analogy to electrical circuits. The equation for resistance is:

$$R = \frac{P(t)}{Q(t)}, \tag{7.60}$$

which is analogous to the electrical circuit equivalent relating current $I$ and voltage drop $V$,

$$V - IR = 0. \tag{7.61}$$

The expression for outlet resistance is

$$p(z_{out}, t) - Q(z, t)R = 0. \tag{7.62}$$

To compute the resistance of a bifurcation, we can add the resistances of the daughter branches in parallel and then add this in series to the segment resistance of the parent. We will make the same analogy with impedance in the following section.

### 7.2.1 Impedance of a vessel bifurcation

Pressure at time $t$ depends not only on the flow at that time, but also on the flow history because of inertia, distensibility, wave reflections, etc. Resistance is essentially a steady flow phenomenon, while impedance is an oscillatory flow phenomenon. Impedance is defined as

$$\tilde{Z}(\omega) = \frac{\tilde{P}(\omega)}{\tilde{Q}(\omega}, \tag{7.63}$$

which can be represented as a measure of opposition to flow at a specific wave number

$$P(t) = \frac{1}{T}\int_{t-T}^{t} Q(\tau)z(t-\tau)d\tau, \tag{7.64}$$

where $z(t)$ is an inverse discrete Fourier transform of $\tilde{Z}(\omega)$.

We now proceed to calculate the impedance of the simple vessel bifurcation shown in Figure 7.2, and subsequently, the impedance of a bifurcating vascular tree. In the previous section we derived the equations needed to find the impedance in one segment. Recall that input impedance ($Z_i$) for a vessel of length L is given by

$$Z_i = \frac{P(0)}{Q(0)} = Z_0\frac{1-\Gamma e^{-2\lambda L}}{1+\Gamma e^{-2\lambda L}}, \tag{7.65}$$

where

$$\underbrace{Z_0}_{\text{Characteristic impedance}} = \frac{\rho C_0^2 \lambda}{i\omega A} \tag{7.66}$$

$$\underbrace{\Gamma}_{\text{Refection Coefficient}} = \frac{Z_0 - Z_T}{Z_0 + Z_T} \tag{7.67}$$

$$\lambda^2 = \frac{1}{C_0^2}(-\omega^2 + i\omega f_0). \tag{7.68}$$

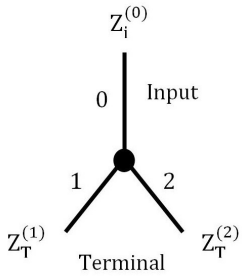


Figure 7.2: Bifurcation

Now we can proceed to calculate impedance for each branch, giving

$$Z_i^{(1)} = Z_0^{(1)} \frac{1 - \Gamma^{(1)} e^{-2\lambda(1)L(1)}}{1 + \Gamma^{(1)} e^{-2\lambda(1)L(1)}}, \tag{7.69}$$

$$Z_i^{(2)} = Z_0^{(2)} \frac{1 - \Gamma^{(2)} e^{-2\lambda(2)L(2)}}{1 + \Gamma^{(2)} e^{-2\lambda(2)L(2)}}. \tag{7.70}$$

$$\tag{7.71}$$

At the bifurcation, we enforce conservation of mass and continuity of pressure, giving

$$Q^{(0)} L^{(0)} = Q^{(1)}(0) + Q^{(2)}(0), \tag{7.72}$$

$$P^{(0)} L^{(0)} = P^{(1)}(0) = P^{(2)}(0). \tag{7.73}$$

Terminal impedance of the parent is then given by

$$Z_T^{(0)} = \frac{P^{(0)} L^{(0)}}{Q^{(0)} L^{(0)}} = \frac{P^{(1)}(0)}{Q^{(1)}(0) + Q^{(2)}(0)} \tag{7.74}$$

$$\Rightarrow \frac{1}{Z_T^{(0)}} = \frac{Q^{(1)}(0)}{P^{(1)}(0)} + \frac{Q^{(2)}(0)}{P^{(2)}(0)} = \frac{1}{Z_i^{(1)}} + \frac{1}{Z_i^{(2)}} \tag{7.75}$$

$$\therefore Z_T^{(0)} = \frac{Z_i^1 Z_i^2}{Z_i^1 + Z_i^2}. \tag{7.76}$$

Now we can use this to find the reflection coefficient of the parent vessel

$$\Gamma^{(0)} = \frac{Z_0^{(0)} - Z_T^{(0)}}{Z_0^{(0)} + Z_T^{(0)}}, \tag{7.77}$$

leading to the input impedance of the parent vessel,

$$Z_i^{(0)} = Z_0^{(0)} \frac{1 - \Gamma^{(0)} e^{-2\lambda^{(0)} L^{(0)}}}{1 + \Gamma^{(0)} e^{-2\lambda^{(0)} L^{(0)}}}. \tag{7.78}$$

We can now use the parent vessel impedance to calculate pressure if the inlet flow rate is known, so that

$$P^{(0)}(0) = Z_i^{(0)} Q^{(0)}(0). \tag{7.79}$$

Now we can use the assumed solutions for $P(z)$ and $Q(z)$ to compute the solution over the entire length of the parent vessel:

$$Q(z) = \frac{Q_0}{1 + \Gamma e^{-2\lambda L}} [e^{-\lambda z} + \Gamma e^{\lambda(z-2L)}] \tag{7.80}$$

$$P(z) = \frac{Z_0 Q_0}{1 + \Gamma e^{-2\lambda L}} [e^{-\lambda z} - \Gamma e^{\lambda(Z-2L)}] \tag{7.81}$$

$$\tag{7.82}$$

And finally, we can obtain the spatial and time-dependent solutions for flow and pressure as,

$$\mathbf{Q}(\mathbf{z}, \mathbf{t}) = Q(z) e^{(i\omega t)}, \tag{7.83}$$

$$\mathbf{P}(\mathbf{z}, \mathbf{t}) = P(z) e^{(i\omega t)}. \tag{7.84}$$

$$\tag{7.85}$$

A typical impedance curve is shown in Figure 7.3. We observe high modulus of impedance at low frequencies, which drops as frequency increases. The phase drops from zero, becoming more negative and indicating flow leading pressure, before rising above zero at higher frequencies. A zero value indicates flow and pressure are in phase.

### 7.2.2 Procedure for solving a system of bifurcations:

Finally, we can summarize our algorithm for extending the above procedure for a single bifurcation, to computing the impedance of an entire vascular tree as follows:

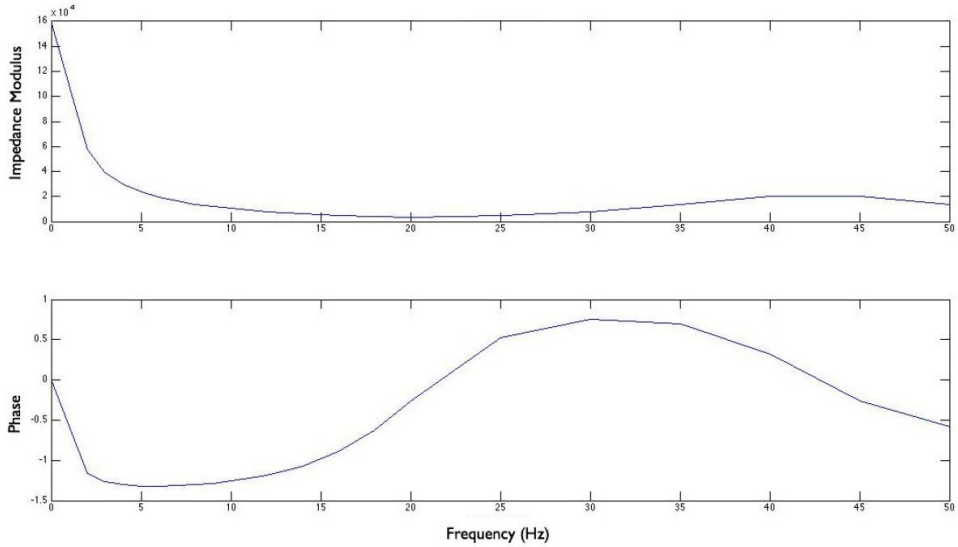


Figure 7.3: Impedance Curve

1. Given terminal impedance

2. Find reflection coefficients of child vessels, (1) and (2)

3. Plug in to find $Z_i^{(1)}$ and $Z_i^{(1)}$

4. Plug in to find $Z_T^{(0)}$

5. Plug in to find $\Gamma^{(0)}$

6. Plug in to find $Z_i^{(0)}$ and march up from the end points

### 7.2.3 Remarks

1. Once Q and P are computed in the parent vessel we can compute total flow into the child vessels and the pressure at the junction:

$$Z_i^{(1)} = \frac{P^{(1)}(0)}{Q^{(1)}(0)} \Rightarrow Q^{(1)}(0) = \frac{P^{(0)}(L^{(0)})}{Z_i^{(1)}} \tag{7.86}$$

$$Z_i^{(2)} = \frac{P^{(2)}(0)}{Q^{(2)}(0)} \Rightarrow Q^{(2)}(0) = \frac{P^{(0)}(L^{(0)})}{Z_i^{(2)}} \tag{7.87}$$

2. Complete analysis of the tree can be conducted using only input flow of the most proximal vessel (parent) and the terminal impedance of distal vessels. If we choose to generate the tree all the way down to the capillary level then we can set $Z_T = 0$ and $\Gamma = 1$.

3. Linearization was done about a zero mean velocity and constant pressure. Therefore we need to include a steady solution to obtain a net flow.

4. We can use a different approach for computing $Z_0$ (ex., Womerseley's elastic tube theory) keeping the rest of the procedure the same.

5. Recall that 1D theory assumes a known velocity profile and further that this profile will not change over the cardiac cycle.

### 7.2.4 Example: Calculating wave propagation speed

Given a constitutive relationship between pressure and radius (or area), we now determine typical values of wave propagation speed. Using the Olufsen relationship, we have

$$P = P_0 + \frac{4}{3}\frac{Eh}{r_0}\left(\frac{r - r_0}{r}\right), \tag{7.88}$$

where

$P_0$ is the reference pressure

$r_0$ is the reference radius

$E$ is the Young's Modulus

and

$h$ is the wall thickness.

We can rewrite the above expression in terms of the cross sectional area where $(A)$ is assumed to be circular so $A = \pi r^2$, giving

$$P = P_0 + \frac{4}{3}\frac{Eh\sqrt{\pi}}{\sqrt{A_0}}\left(1 - \frac{\sqrt{A_0}}{\sqrt{A}}\right) \tag{7.89}$$

And this allows us to compute the wave speed (defined earlier in Equation 7.19), as

$$c_0 = \sqrt{\frac{A}{\rho}\frac{\partial P}{\partial A}} = \sqrt{\frac{A}{\rho}\frac{2}{3}Eh\sqrt{\pi}A^{\frac{-3}{2}}} = \sqrt{\frac{2}{3}\frac{\sqrt{\pi}}{\rho}\frac{Eh}{\sqrt{A}}}. \tag{7.90}$$

Now we use an empirical formula to find Young's modulus:

$$\frac{Eh}{r_0} = k_1 e^{k_2 r_0} + k_3, \tag{7.91}$$

where we have the following values $\rho = 1.06\frac{g}{cc}$, $k_1 = 2 \times 10^7 \frac{gr}{cms^2}$, $k_2 = -22.53\frac{1}{cm}$ and $k_3 = 8.65 \times 10^5 \frac{g}{cms^2}$. Assuming $A \approx A_0$, the wave speed is approximated by

$$c_0 = \sqrt{\frac{2}{3\rho}(k_1 e^{k_2 r_0} + k_3)}, \tag{7.92}$$

which is plotted as a function of radius in Figure 7.4.

We observe that as vessel radius decreases wave speed increases substantially. This is consistent with experimental and clinical observations that smaller vessels are less compliant. In the most extreme case, rigid tubes in fact have infinite wave propagation velocity.

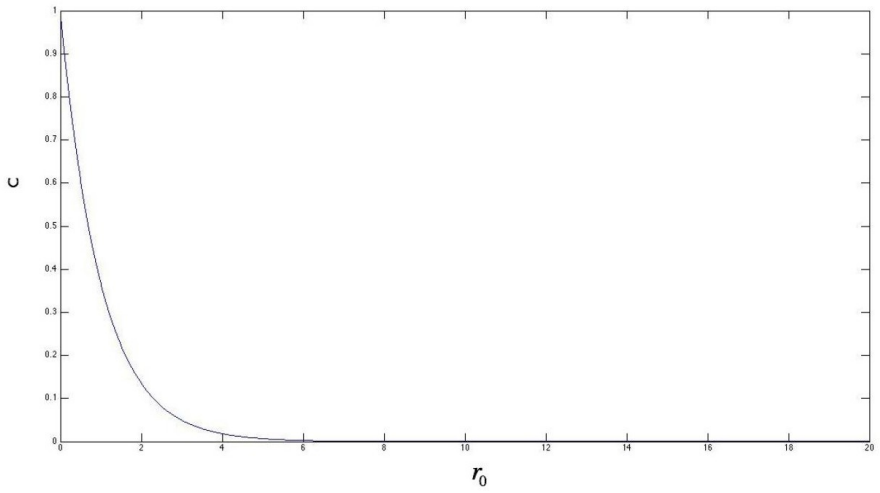


Figure 7.4: Wave propagation speed in vessels

# Chapter 8

# Womersley Theory: Oscillating Flow in a Rigid Vessel

## 8.1 Velocity Profile for a single frequency

In this Chapter, we derive the equations from Womersley's theory of pulsatile flow in rigid tubes, which will be extended to the deformable case in the next chapter. Our presentation closely follows *The Physics of Pulsatile Flow* by Mair Zamir. The derivation is one of the known analytical solutions to the Navier Stokes equations, and gives rise to an important new non-dimensional number that is relevant to cardiovascular blood flow simulations.

We begin by obtaining the simplified equations governing pulsatile blood-flow through an artery using the following assumptions:

1. The flow is fully developed, i.e. edge effects are negligible because the artery is a sufficiently long.
2. Gradients in the azimuthal direction can be ignored because the artery is axisymmetric.
3. Pressure gradients, local artery radii, and resulting velocity profiles are not dependent on the longitudinal coordinate because the walls are rigid.

Simplifying the full Navier Stokes equations, the resulting momentum equation in the axial direction is

$$\frac{\partial v_z}{\partial t} = -\frac{1}{\rho}\frac{\partial P}{\partial z} + \nu\left(\frac{\partial^2 v_z}{\partial r^2} + \frac{1}{r}\frac{\partial v_z}{\partial r}\right). \tag{8.1}$$

$$\tag{8.2}$$

The velocity profile governed by this (now) linear equation can be expressed as the superposition of a steady state and oscillatory solution. The steady-state solution was derived previously and results in the Poiseuille solution, such that axial flow is described by a parabolic function of radius. The oscillatory flow will result in a velocity profile that, when averaged over one period, results in no net fluid flow. To obtain the oscillatory solution, the pressure gradient must be given as a function of time. The simplest oscillating pressure gradient is the sinusoidal function, which we assume to be

$$-\frac{\partial P}{\partial z} = Ae^{i\omega t} = A(\cos(\omega t) + i\sin(\omega t)). \tag{8.3}$$

Note that again due to superposition, this is like solving for the set of solutions of individual modes $A(\cos(\omega t))$ and $A(\sin(\omega t))$.

Under these conditions, the fluid velocity oscillates in bulk as a result of the imposed oscillatory pressure gradient, with a phase difference increasing at high frequencies due to the inertia of the fluid (as we will demonstrate). Because the governing equation is linear, we can assume the following form for the velocity profile, comprised of amplitude and frequency components

$$v_z(r,t) = u(r)e^{i\omega t}. \tag{8.4}$$

We note that a phase difference is allowed in the case when $u(r)$ is complex.

Substituting this expression into the momentum equation we obtain

$$i\omega u e^{i\omega t} = \frac{A}{\rho}e^{i\omega t} + \nu e^{i\omega t}\left(u'' + \frac{1}{r}u'\right), \tag{8.5}$$

which simplifies to

$$u'' + \frac{1}{r}u' - \frac{i\omega}{\nu}u = \frac{-A}{\mu}, \tag{8.6}$$

or

$$r^2u'' + ru' - \frac{i\omega r^2}{\nu}u = \frac{-Ar^2}{\mu}. \tag{8.7}$$

Making a clever change of variables we have

$$x^2 = -ir^2\frac{\omega}{\nu} \Rightarrow x = i^{\frac{3}{2}}r\sqrt{\frac{\omega}{\nu}}, \tag{8.8}$$

with the intermediate steps, applying the chain rule,

$$\begin{aligned} ru' &= r\frac{\partial u}{\partial x}\frac{\partial x}{\partial r} && (8.9)\\ &= ri^{\frac{3}{2}}\sqrt{\frac{\omega}{\nu}}\frac{\partial u}{\partial x} && (8.10)\\ &= x\frac{\partial u}{\partial x} && (8.11) \end{aligned}$$

and

$$\begin{aligned} r^2u'' &= r^2\frac{\partial^2 u}{\partial x^2}\frac{\partial x}{\partial r}\frac{\partial x}{\partial r} && (8.12)\\ &= i^3r^2\frac{\omega}{\nu}\frac{\partial^2 u}{\partial x^2} && (8.13)\\ &= x^2\frac{\partial^2 u}{\partial x^2}, && (8.14) \end{aligned}$$

the equation simplifies to

$$\begin{aligned} x^2\frac{\partial^2 u}{\partial x^2} + x\frac{\partial u}{\partial x} + x^2u &= \frac{x^2A\nu}{i\omega\mu} && (8.15)\\ &= \frac{x^2A}{i\rho\omega}. && (8.16) \end{aligned}$$

where $\rho = \frac{\mu}{\nu}$, in other words, density, $\rho$, is the ratio between the dynamic viscosity, $\mu$, and the kinematic viscosity, $\nu$

With a second clever change of variables

$$y = u - \frac{A}{i\rho\omega} \Rightarrow \frac{\partial y}{\partial x} = \frac{\partial u}{\partial x}\,, \tag{8.17}$$

the equation reduces to

$$x^2y'' + xy' + x^2y = 0\,. \tag{8.18}$$

We now recognize this equation as a *Bessel Equation of order 0*, the solution to which is

$$y = c_1J_0(x) + c_2Y_0(x). \tag{8.19}$$

### 8.1.1 Boundary Conditions

The following boundary conditions are used to determine the constants in Eq. (8.19):

1. The velocity must not diverge at the center of the pipe. Since $Y_0(x) \to -\infty$ as $x \to 0$, this implies $C_2 = 0$ for a physical solution.

2. The velocity is zero at the walls as a result of the no-slip condition, i.e. $u(R) = 0$. Therefore,

$$\begin{aligned} y(x)|_{r=R} &= y\left(i^{\frac{3}{2}} R\sqrt{\frac{\omega}{\nu}}\right) && (8.20)\\ &= c_1 J_0\left(R\sqrt{\frac{\omega}{\nu}} i^{\frac{3}{2}}\right) && (8.21)\\ &= \frac{-A}{i\rho\omega}\,, && (8.22) \end{aligned}$$

and

$$c_1 = \frac{Ai}{\rho\omega J_0\left(R\sqrt{\frac{\omega}{\nu}} i^{\frac{3}{2}}\right)}. \qquad (8.23)$$

Inserting the constants $C_1$ and $C_2$ into Eq. 8.19 we have

$$y(x) = \frac{-A}{i\rho\omega J_0\left(R\sqrt{\frac{\omega}{\nu}} i^{\frac{3}{2}}\right)} J_0(x). \qquad (8.24)$$

The final solution for the profile is then

$$u\left(r\right) = \frac{A}{i\rho\omega}\left[1 - \frac{J_0\left(i^{\frac{3}{2}} r\sqrt{\frac{\omega}{\nu}}\right)}{J_0\left(R\sqrt{\frac{\omega}{\nu}} i^{\frac{3}{2}}\right)}\right] \qquad (8.25)$$

and thus the periodic velocity field in a straight, rigid vessel is given by

$$v_z(r,t) = \frac{A}{i\rho\omega}\left[1 - \frac{J_0\left(i^{\frac{3}{2}} r\sqrt{\frac{\omega}{\nu}}\right)}{J_0\left(R\sqrt{\frac{\omega}{\nu}} i^{\frac{3}{2}}\right)}\right] e^{i\omega t}. \qquad (8.26)$$

## 8.2 Generalized Velocity Profile

In the vasculature, the pressure gradients are (in general) periodic but cannot be modeled by the overly simplified, sinusoidal function considered in the previous section. A more general periodic pressure gradient can instead be expressed as a Fourier series

$$-\frac{\partial p}{\partial z} = \sum_{n=0}^{N} A_n e^{in\omega t}. \tag{8.27}$$

In practice, a truncated series of ten modes or less is usually sufficient to represent physiological pressure gradients.

Because the Fourier series is a linear combination of sinusoidal waves of various frequencies, each mode of the Fourier series must independently satisfy the momentum conservation equation. As a result, the velocity profile is simply the linear combination of these solutions, so that

$$v_z = \sum_{n=0}^{N} v_z^n. \tag{8.28}$$

Recall that for $\omega = 0$ (i.e. $n = 0$) we must have Poiseuille's solution

$$v_z^0 = \frac{A_0 R^2}{4\mu}\left(1 - \left(\frac{r}{R}\right)^2\right). \tag{8.29}$$

For the other modes in the solution, $n = 1, 2, 3, \ldots$ we have

$$v_z^n = \frac{A_n}{i\rho n\omega}\left[1 - \frac{J_0\left(R\sqrt{\frac{n\omega}{\nu}}\frac{r}{R}i^{\frac{3}{2}}\right)}{J_0\left(R\sqrt{\frac{n\omega}{\nu}}i^{\frac{3}{2}}\right)}\right] e^{in\omega t}. \tag{8.30}$$

## 8.3 Womersley Number

We now observe that the velocity profile is dependent on the non-dimensional parameter

$$\alpha_n = R\sqrt{\frac{n\omega}{\nu}} \quad n = 1, 2, ..., N. \tag{8.31}$$

This number, $\alpha_n$, is called the *Womersley number*, which describes the ratio between the pulsatile flow frequency (or transient inertial force) and the viscous effects

$$\alpha^2 = \frac{\text{Transient inertial force}}{\text{Viscous force}} = \frac{\omega L^2}{\nu}. \tag{8.32}$$

We note that the Stokes number, which is commonly encountered in fluid mechanics, and the Womersley number are related by

$$\text{Stokes Number} = (\text{Womersley Number})^2. \tag{8.33}$$

Also from Eq. (8.32), note that $\omega L \sim v$ and hence we see a close, but distinct relation with the Reynolds number,

$$Re = \frac{vL}{\nu}\ , \tag{8.34}$$

which is another non-dimensional measure relating inertial to viscous forces.

Using the definition of Womersley number, the axial velocity profile becomes

$$v_z = \sum_{n=0}^{N} v_z^n, \tag{8.35}$$

where

$$v_z^0 = \frac{A_0 R^2}{4\mu}\left(1 - \left(\frac{r}{R}\right)^2\right), \tag{8.36}$$

and

$$v_z^n = \frac{A_n R^2}{i\mu\alpha_n^2}\left[1 - \frac{J_0\left(\alpha_n \frac{r}{R} i^{\frac{3}{2}}\right)}{J_0\left(\alpha_n i^{\frac{3}{2}}\right)}\right] e^{in\omega t}. \tag{8.37}$$

We observe that when the Womersley number is smaller than one, the frequency is low enough that the velocity profile oscillates in phase with the pressure gradient. As a result, a parabolic profile develops.

Large $\alpha \Rightarrow$ Oscillatory inertia force dominate.

At Womersley numbers larger than ten, the boundary layer does not have time to propagate into the center of the pipe. As a result, the velocity profile

| | Womersley Number | Reynold's Number |
|---|---|---|
| Ascending Aorta | 13.2 | 4500 |
| Abdominal Aorta | 8 | 1250 |
| Arteriole | 0.04 | 0.09 |
| IVC | 8.8 | 700 |
| Main P.A. | 15 | 3000 |

Figure 8.1: Womersley Numbers of Typical Vessels (Frequency of 2 Hz)

becomes plug-like. Inertial effects cause the velocity profile to lag the pressure gradient by approximately 90 degrees.

Small $\alpha \Rightarrow$ Viscous force dominates.

Typical Womersely numbers for a pulsatile frequency of 2 Hertz are reported in Figure 8.1. The Womersley number gets smaller as we go down in the arterial tree. As a general trend, as the radii decreases, the velocity profile becomes more parabolic and steady.

## 8.4 Oscillatory flow rate and shear stress

Computing the flow rate using the Wormersley solution, we integrate as follows

$$
\begin{aligned}
Q(t) &= 2\pi \int_0^R v_z(r,t) r dr && (8.38)\\
&= 2\pi \int_0^R \frac{A}{i\rho\omega}\left[1 - \frac{J_0(\alpha \frac{r}{R} i^{\frac{3}{2}})}{J_0(\alpha i^{\frac{3}{2}})}\right] e^{i\omega t} r dr && (8.39)\\
&= \frac{2\pi A}{i\rho\omega} e^{i\omega t}\left[\int_0^R r dr - \frac{1}{J_0(\alpha i^{\frac{3}{2}})}\int_0^R J_0(\alpha \frac{r}{R} i^{\frac{3}{2}}) r dr\right]. && (8.40)
\end{aligned}
$$

We can reformat the second integration term

$$= \frac{2\pi A}{i\rho\omega} e^{i\omega t} \left[ \int_0^R r dr - \frac{iR^2}{\alpha^2 J_0(\alpha i^{\frac{3}{2}})} \int_0^R i^{\frac{3}{2}} \alpha \frac{r}{R} J_0(\alpha \frac{r}{R} i^{\frac{3}{2}}) i^{\frac{3}{2}} \alpha \frac{1}{R} dr \right] \tag{8.41}$$

Note the added terms cancel out,

$$\frac{iR^2}{\alpha^2} \cdot i^{\frac{3}{2}} \alpha \frac{1}{R} \cdot i^{\frac{3}{2}} \alpha \frac{1}{R} = 1 \tag{8.42}$$

making this an equivalent expression. We can now use integration by substitution for the second integration term using the relationship

$$\int_a^b f(g(r)) g'(r) dr = \int_{g(a)}^{g(b)} f(u) du, \quad u = g(r) \tag{8.43}$$

where $g(r) = i^{\frac{3}{2}} \alpha \frac{r}{R}$, $f(g(r)) = g(r) J_0(g(r))$, and $g'(r) = i^{\frac{3}{2}} \alpha \frac{1}{R}$

Now

$$= \frac{2\pi A}{i\rho\omega} e^{i\omega t} \left[ \int_0^R r dr - \frac{iR^2}{\alpha^2 J_0(\alpha i^{\frac{3}{2}})} \int_0^{i^{\frac{3}{2}}\alpha} u J_0(u) du \right] \tag{8.44}$$

With the relationship

$$\int_0^x u J_0(u) du = x J_1(x), \tag{8.45}$$

where $J_1(x)$ is a Bessel function of the first kind, we have

$$= \frac{2\pi A}{i\rho\omega} e^{i\omega t} \left[ \int_0^R r dr - \frac{iR^2}{\alpha^2 J_0(\alpha i^{\frac{3}{2}})} [i^{\frac{3}{2}} \alpha J_1(i^{\frac{3}{2}} \alpha) \right] \tag{8.46}$$

$$Q(t) = \frac{\pi A R^2}{i\rho\omega} e^{i\omega t} \left[ 1 - \frac{2 J_1(\alpha i^{\frac{3}{2}})}{J_0(\alpha i^{\frac{3}{2}}) \alpha i^{\frac{3}{2}}} \right]. \tag{8.47}$$

**Computing the flow velocity given the pressure gradient** In cases that the flow rate $Q(t)$ is given instead of $\frac{\partial P}{\partial z}$ (e.g. when we know the flow rate from phase contrast MRI data), we can compute $v_z(r,t)$ via the following steps:

a) Fourier Transform $Q(t)$:
$Q(t) = \sum_{n=0}^{N} B_n e^{in\omega t}$

b) Equate $2\pi \int_0^R v_z(r,t) r dr$ with $\sum_{n=0}^{N} B_n e^{in\omega t}$ to express $A_n$ in terms of $B_n$

c) Substitute results from part b into equation for $v_z(r,t)$.

i.e. FFT $Q(t) \Rightarrow B_n$
then $A_0 = f(B_0)$
$A_n = f(B_n)$

**Calculate velocity profile given centerline velocity** When the centerline velcocity is known (e.g. if velocity is obtained from echocardiography data), then we have

$$v_z(0,t) = \sum_{n=0}^{N} C_n e^{in\omega t}.$$

In this case, we can obtain $A_n$ in terms of $C_n$

i.e. FFT $v_z(t) \Rightarrow C_n$
then $A_0 = f(C_0)$
$A_n = f(C_n)$

**Calculating the shear stress** Finally, we can compute wall shear stress from the velocity profile by starting with

$$\tau_w(t) = \mu \frac{\partial v_z}{\partial r}|_{r=R}. \tag{8.48}$$

We now use the relationship:

$$\frac{d}{dx}J_0(x) = -J_1(x) \tag{8.49}$$

so that

$$\frac{\partial v_z}{\partial r} = \frac{-A_0 r}{2\mu} + \sum_{n=1}^{N} \frac{A_n}{i\rho n\omega}(\frac{\alpha_n i^{\frac{3}{2}}}{R})\frac{J_1(\alpha_n \frac{r}{R} i^{\frac{3}{2}})}{J_0(\alpha_n i^{\frac{3}{2}})} e^{in\omega t}. \tag{8.50}$$

Simplifying, we have

$$\tau_w = \frac{-A_0 R}{2} + \sum_{n=1}^{N} \frac{R A_n i^{\frac{1}{2}}}{\alpha_n} \frac{J_1(\alpha_n i^{\frac{3}{2}})}{J_0(\alpha_n i^{\frac{3}{2}})} e^{in\omega t}. \tag{8.51}$$

We note that to find $i^{\frac{1}{2}}$ we use the relations

$$i = e^{i\frac{\pi}{2}} = \underbrace{cos\frac{\pi}{2}}_{0} + i \underbrace{sin\frac{\pi}{2}}_{1} \tag{8.52}$$

and

$$i^{\frac{1}{2}} = e^{i\frac{\pi}{4}} = cos\frac{\pi}{4} + sin\frac{\pi}{4} = \frac{\sqrt{2}}{2}(i+1). \tag{8.53}$$

## 8.5 A brief review of Fourier Transforms

To find the velocity profile, flow rate, and shear stress we needed to use Fourier transforms. For completeness, we provide a brief review of Fourier theory below.

**Continuous Fourier Transform** Fourier Transform of $g(t)$:

$$G(f) = F(g(t)) = \int_{-\infty}^{+\infty} g(t)e^{-i2\pi ft} \tag{8.54}$$

$$\tag{8.55}$$

Inverse Fourier Transform:

$$g(t) = F^{-1}(G(f)) = \int_{-\infty}^{\infty} G(f)e^{i2\pi ft}df \tag{8.56}$$

$$\tag{8.57}$$

$$\omega = 2\pi f \tag{8.58}$$

$$f = \frac{\omega}{2\pi} = \frac{1}{T} = [\frac{\text{rad}}{\text{sec}}] \tag{8.59}$$

$G(f) \Rightarrow$ transforms g(t) into frequency space.

**Discrete Fourier Transform** Discrete Fourier Transform:

$$P(t) = \sum_{n=-\infty}^{n=+\infty} \alpha_n e^{in\omega t} \tag{8.60}$$

$$\tag{8.61}$$

Fourier Coefficients:

$$\alpha_n = \frac{1}{T}\int_{\frac{-T}{2}}^{\frac{T}{2}} P(t)e^{-i\frac{2\pi}{T}nT}dt \tag{8.62}$$

$$\tag{8.63}$$

# Chapter 9

# Womersley theory: Oscillating Flow in a Deformable Vessel

In this chapter, we extend the rigid wall derivation of Womersley's theory from the previous chapter to the case of pulsatile flow in an elastic tube. Before we begin with the derivation, we first need to understand the difference in physics between the rigid and elastic tube cases.

## 9.1 Comparison between Rigid and Elastic Case

For the rigid case we have

- Pressure gradient is a function of time only
- Velocity, w, of a function or r and t only, not z
- When oscillatory pressure gradient occurs velocity oscillates at the same frequency. The velocity is the same at every cross section, therefore fluid oscillates in bulk motion and there is no wave propagation as long as $\rho$ is constant.

For the elastic case we have

- The wall moves and therefore v is not equal to zero.
- $\frac{\partial p}{\partial z}$, w, v are function of z.
- The input oscillatory pressure propagates down the tube.
- Wave motion is present
- The speed of the wave motion depends on Young's Modulus, E. We define the wave speed is $c_0 = \sqrt{\frac{Eh}{\rho d}}$.
- Young's Modulus increases if the wall is more rigid.
- As the Young's Modulus approaches $\infty$, as it does in the rigid wall case, the wave travels at infinite speed and therefore a pressure change at one of the tube is transmitted instantaneously.

## 9.2 Derivation of oscillatory velocity profile for elastic wall case

The following steps are needed to derive the elastic wall solutions:

1. Equations of motion of the vessel wall.
2. Equations of motion of the fluid.
3. Determine boundary conditions at the fluid / solid interface.
4. Determine the solution.

### 9.2.1 Derivation of Vessel Wall Equations

We begin with the first step, determining the equations of motion of the vessel wall. To do this we must make two assumptions:

1. We must assume that the wall is thin and therefore can apply thin walled tube theory.
2. We assume linear elasticity.

The procedure is then as follows:

1. We consider two stress states: (i) internal pressure, no axial strain and (ii) axial force but no in plane deformation. We use superposition to obtain the stress - strain laws. The hoop stress we will find is

$$T_{\theta\theta} = B\Big[\frac{\xi}{R} + \sigma\frac{\partial\zeta}{\partial z}\Big] \tag{9.1}$$

and the axial stress we will find is

$$T_{zz} = B\Big[\sigma\frac{\xi}{R} + \frac{\partial\zeta}{\partial z}\Big]\,, \tag{9.2}$$

where $\sigma$ is the Poisson's ratio and $B = \frac{E}{1-\sigma^2}$ with $\xi$ being the radial displacement and $\zeta$ being the axial displacement.

2. Next we will use Cauchy's equations of motion for a solid

$$\rho\frac{\partial^2\mathbf{u}}{\partial t^2} = \mathbf{B_0} + \nabla\cdot\mathbf{T} \tag{9.3}$$

where $\rho$ is the wall density, $\mathbf{u}(\xi,\eta,\zeta)$ is the displacement vector, $\mathbf{B_0}$ is the body force per unit volume and $\mathbf{T}$ is the Cauchy stress tensor. We will obtain the equations for the wall by a momentum balance. The radial equation we will derive is

$$\frac{\partial^2\xi}{\partial t^2} = \frac{p}{\rho h} - \frac{B}{\rho}\Big[\frac{\xi}{R^2} + \frac{\sigma}{R}\frac{\partial\zeta}{\partial z}\Big] \tag{9.4}$$

and the axial equation is

$$\frac{\partial^2 \zeta}{\partial t^2} = \frac{\tau_w}{h\rho} + \frac{B}{\rho}\Big[\frac{\partial^2 \zeta}{\partial z^2} + \frac{\sigma}{R}\frac{\partial \xi}{\partial z}\Big], \tag{9.5}$$

where $p$ and $\tau_w$ are the fluid pressure and shear stress exerted by fluids, respectively.

(a) For the case of internal pressure with no axial strain we refer to Figure 9.1, where $\rho_0$ is the fluid density, $\mu$ is the viscosity of the fluid, and $\rho$ is the density of the wall.

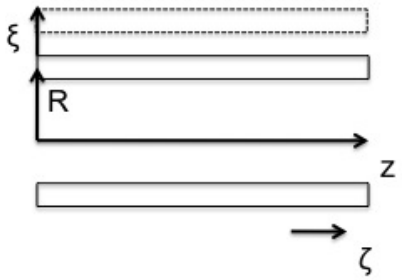


Figure 9.1: Internal pressure, with no axial strain

We then use the linear constitutive equation to relate stress and strain

$$\epsilon_{ij} = \frac{1}{E}[(1+\sigma)T_{ij} - \sigma T_{kk}\delta_{ij}] \tag{9.6}$$

where $T_{ij}$ is the stress tensor. Earlier we made the thin wall assumption, therefore we can say $T_{rr} << T_{\theta\theta}$. The axial strain is given by

$$\epsilon_{zz} = 0 = \frac{1}{E}[T_{zz} - \sigma(T_{\theta\theta} + T_{rr})]. \tag{9.7}$$

Neglecting $T_{rr}$, we have

$$T_{zz} = \sigma T_{\theta\theta}. \tag{9.8}$$

Similarly, the radial strain and stress is related by

$$\epsilon_{\theta\theta} = \frac{1}{E}[T_{\theta\theta} - \sigma(T_{zz} + T_{rr})]. \tag{9.9}$$

We radial strain is

$$\epsilon_{\theta\theta} = \frac{2\pi(R+\xi) - 2\pi R}{2\pi R} = \frac{\xi}{R} \tag{9.10}$$

Thus we have

$$\begin{aligned} \frac{E\xi}{R} &= [T_{\theta\theta} - \sigma(T_{zz} + T_{rr})] && (9.11)\\ &\approx T_{\theta\theta} - \sigma^2 T_{\theta\theta} && (9.12)\\ &= T_{\theta\theta}(1-\sigma^2). && (9.13) \end{aligned}$$

Therefore $T_{\theta\theta} = \frac{B\xi}{R}$ and $T_{zz} = \frac{\sigma B\xi}{R}$.

(b) Next we look at the axial force with no in-plane (i.e. radial expansion) deformation. We know that $\sigma_{\theta\theta} = 0$ and $T_{rr} << T_{zz}$. We then see

$$0 = \frac{1}{E}[T_{\theta\theta} - \sigma(T_{rr} + T_{zz})] \tag{9.14}$$

and

$$T_{\theta\theta} \approx \sigma T_{zz}. \tag{9.15}$$

We then define

$$\epsilon_{zz} = \frac{\partial\zeta}{\partial z} = \frac{1}{E}[T_{zz} - \sigma(T_{\theta\theta} + T_{rr}] \tag{9.16}$$

which reduces to

$$E\frac{\partial\zeta}{\partial z} = T_{zz}(1-\sigma^2)\ . \tag{9.17}$$

In summary, we note that $T_{zz} = B\frac{\partial\zeta}{\partial z}$ and $T_{\theta\theta} = \sigma B\frac{\partial\zeta}{\partial z}$. We can linearly combine the results for (a) and (b) and therefore we obtain

$$T_{\theta\theta} = B\Big[\frac{\xi}{R} + \sigma\frac{\partial\zeta}{\partial z}\Big] \tag{9.18}$$

$$T_{zz} = B\Big[\frac{\sigma\xi}{R} + \frac{\partial\zeta}{\partial z}\Big] \tag{9.19}$$

**Conservation of Momentum for a Continuum** We begin with Cauchy's equations for conservation of momentun in a continuum

$$\rho \frac{\partial^2 \mathbf{u}}{\partial t^2} = \mathbf{B_0} + \nabla \cdot \mathbf{T},$$

where $\rho$ is the density of the solid, $u = [\xi, 0, \zeta]'$ is the displacement vector and $T$ is the stress tensor.

The divergence of the stress tensor in cylindrical coordinates for the axisymmetric thin wall approximation (radius $r = R$) can be simplified as follows

$$(\nabla \cdot T)_r = \frac{\partial T_{rr}}{\partial r} + \frac{1}{r}\frac{\partial T_{r\theta}}{\partial \theta} + \frac{T_{rr} - T_{\theta\theta}}{r} + \frac{\partial T_{rz}}{\partial z} = \frac{T_{rr} - T_{\theta\theta}}{r}$$

$$(\nabla \cdot T)_z = \frac{\partial T_{zr}}{\partial r} + \frac{1}{r}\frac{\partial T_{z\theta}}{\partial \theta} + \frac{T_{zr}}{r} + \frac{\partial T_{zz}}{\partial z} = \frac{\partial T_{zz}}{\partial z}.$$

The radial and axial equations for conservation of momentum of the continuum are as follows:

Radial:

$$\rho \frac{\partial^2 \xi}{\partial t^2} = \frac{p}{h} - \frac{B}{R}(\frac{\xi}{R} + \sigma \frac{\partial \zeta}{\partial z})$$

Axial:

$$\rho \frac{\partial^2 \zeta}{\partial t^2} = B_z + B(\frac{\sigma}{R}\frac{\partial \xi}{\partial z} + \frac{\partial^2 \zeta}{\partial z^2})$$

**Origin of $B_z$** .

The term $B_z$ comes from the viscous forces from the fluid, $B_z = \tau_w/h$. It is the shear stress acting on the wall due to the fluid. The velocity vector for the fluid is defined as $[u, 0, w]'$. The shear stress on the fluid is

$$\tau_{rz} = \mu(\frac{\partial w}{\partial r} + \frac{\partial u}{\partial z}).$$

Thus the shear stress exerted by the fluid on the vessel wall is

$$\tau_w = -\tau_{rz} = -\mu(\frac{\partial w}{\partial r} + \frac{\partial u}{\partial z})|_{r=R}$$

The axial component of the momentum equation is then obtained

$$\rho\frac{\partial^2 \zeta}{\partial t^2} = -\frac{\mu}{h}(\frac{\partial w}{\partial r} + \frac{\partial u}{\partial z})|_{r=R} + B(\frac{\sigma}{R}\frac{\partial \xi}{\partial z} + \frac{\partial^2 \zeta}{\partial z^2})$$

Both the axial and radial equations will be coupled with the fluid mechanics equations through the pressure term $p$ and the fluid velocity at the wall.

### 9.2.2 Equations of Motion of a Fluid in a Pipe

We next derive the equations governing fluid flow in an elastic pipe.

**Assumptions:**

- velocity: radial $u$, axial $w$, and $v_\theta = 0$.
- axisymmetric flow $\partial/\partial\theta = 0$.
- $u = u(r, z, t)$, $w = w(r, z, t)$.

**Continuity:**

$$\nabla \cdot \mathbf{u} = \frac{\partial u}{\partial r} + \frac{u}{r} + \frac{\partial w}{\partial z} = 0$$

**Conservation of Momentum:** Radial component:

$$\frac{\partial u}{\partial t} + u\frac{\partial u}{\partial r} + w\frac{\partial u}{\partial z} = -\frac{1}{\rho_0}\frac{\partial p}{\partial r} + \nu(\frac{\partial^2 u}{\partial r^2} + \frac{1}{r}\frac{\partial u}{\partial r} + \frac{\partial^2 u}{\partial z^2} - \frac{u}{r^2}) \qquad (9.20)$$

Axial component:

$$\frac{\partial w}{\partial t} + u\frac{\partial w}{\partial r} + w\frac{\partial w}{\partial z} = -\frac{1}{\rho_0}\frac{\partial p}{\partial z} + \nu(\frac{\partial^2 w}{\partial r^2} + \frac{1}{r}\frac{\partial w}{\partial r} + \frac{\partial^2 w}{\partial z^2}) \tag{9.21}$$

Now we need to assume a solution of the form

$$u = u_1(r)e^{i\omega[t-z/c]}, \tag{9.22}$$

$$w = w_1(r)e^{i\omega[t-z/c]}, \tag{9.23}$$

$$p = p_1(r)e^{i\omega[t-z/c]}, \tag{9.24}$$

where $c$ is the wave speed.

**Long Wave Approximation and its Consequences.** Looking at realistic values of the Young's modulus ($E$), density($\rho$), thickness ($h$), and radius ($R$) of a vessel, and knowing that $c = \sqrt{\frac{Eh}{2\rho R}}$, we can conclude that the speed at which the waves propagate along the vessel is much higher that the mean velocity of the bloodstream. Therefore, if the wavelength of the propagating waves is $L$ and the diameter of the vessel is $D$, we are assuming that $L/D >> 1$.

With this approximation, we are assuming that locally the whole vessel expands only radially, resulting in an expansion motion that we call *BREATHING MODE*.

From this long wave approximation, the momentum equations may be further simplified using scaling analysis. First, let us calculate the derivatives of the velocity

$$\begin{aligned}
\frac{\partial u}{\partial t} &= i\omega u_1(r)e^{i\omega[t-z/c]}, \\
\frac{\partial u}{\partial r} &= \frac{du_1(r)}{dr}e^{i\omega[t-z/c]}, \\
\frac{\partial u}{\partial z} &= -i\frac{\omega}{c}u_1(r)e^{i\omega[t-z/c]}, \\
\frac{\partial w}{\partial z} &= -i\frac{\omega}{c}w_1(r)e^{i\omega[t-z/c]}.
\end{aligned}$$

Now let us compare the unsteady term with the convective term, which yields

$$\frac{\frac{\partial u}{\partial t}}{u\frac{\partial u}{\partial r}} \propto \frac{i\omega u_1(r)e^{i\omega[t-z/c]}}{u_1(r)e^{i\omega[t-z/c]}\frac{du_1(r)}{dr}e^{i\omega[t-z/c]}}.$$

But from continuity we also know that

$$\frac{\partial u}{\partial r} \propto \frac{\partial w}{\partial z}.$$

Hence,

$$\frac{\frac{\partial u}{\partial t}}{u\frac{\partial u}{\partial r}} \propto \frac{i\omega}{-i\frac{\omega}{c}w_1(r)} \propto \frac{c}{w_1} >> 1.$$

The long wave approximation stated that the average velocity of the blood in the vessel is much smaller than the wave speed. This means that the convective terms can be neglected from the radial momentum equations, compared to the unsteady term (periodic flow).

Similarly, it is trivially shown that the convective terms can also be neglected in the axial momentum equation.

**Finding the fluid equations from assumed solution.** Inserting the assumed solutions in the radial and axial momentum equations, as well as in the continuity equation, we obtain

Radial:

$$i\omega u_1 = -\frac{1}{\rho_0}\frac{dp_1}{dr} + \nu(\frac{d^2u_1}{dr^2} + \frac{1}{r}\frac{du_1}{dr} - \frac{u_1}{r^2})$$

Axial:

$$i\omega w_1 = \frac{i\omega}{\rho_0 c}p_1 + \nu(\frac{d^2w_1}{dr^2} + \frac{1}{r}\frac{dw_1}{dr})$$

Continuity:

$$\frac{du_1}{dr} + \frac{u_1}{r} - \frac{i\omega}{c} w_1 = 0$$

A further step must be made. We will assume a pressure of the form of:

$$p_1 = A_1 J_0(Ky),$$

where $J_0$ is the zero order Bessel function and $K$ is yet to be determined. Inserting this expression into the system of ODE's and solving for a homogeneous and the particular solutions, we obtain expressions for the amplitude of both the axial and radial velocities, as a function of $y$, where $y = r/R$

$$w_1 = c_1 J_0(\alpha i^{3/2} y) - \frac{i\omega R^2}{c\mu}\left(\frac{A_1}{i^3\alpha^2 - K^2}\right) J_0(Ky)$$

$$u_1 = c_2 J_1(\alpha i^{3/2} y) - \frac{RK}{\mu}\left(\frac{A_1}{i^3\alpha^2 - K^2}\right) J_1(Ky).$$

Inserting the above soluations for $u_1$ and $w_1$ into the continuity equation, and recalling that $\frac{d}{dx}(xJ_1(x)) = xJ_0(x)$ and $\frac{du_1}{dr} + \frac{u_1}{r} = \frac{1}{r}\frac{dru_1}{dr}$, we can re-express continuity as

$$0 = \underbrace{\left[\frac{\alpha i^{3/2} c_2}{R} - \frac{i\omega c_1}{c}\right]}_{=0} J_0(\alpha i^{3/2} y) - \underbrace{\frac{A_1}{\mu(i^3\alpha^2 - K^2)}\left[K^2 + \frac{\omega^2 R^2}{c^2}\right]}_{=0} J_0(Ky).$$

Note that only the terms in braces may be zero, since this equation must be satisfied for every position $y$, the Bessel function cannot be zero, unless at a particular $y$. We are then able to set to zero both of the terms under braces so that

$$\frac{\alpha i^{3/2} c_2}{R} - \frac{i\omega c_1}{c} = 0 \quad \rightarrow \quad \frac{c_2}{c_1} = \frac{i\omega R}{c\alpha i^{3/2}}$$

and

$$K^2 + \frac{\omega^2 R^2}{c^2} = 0 \quad \rightarrow \quad K = \frac{i\omega R}{c}.$$

Now returning to the expressions of the solutions for $u_1$ and $w_1$ and substituting $c_2$ as function of $c_1$, and K we have

$$w_1 = c_1 J_0(\alpha i^{3/2} y) - \frac{i\omega R^2}{c\mu}\left(\frac{A_1}{i^3\alpha^2 + \frac{\omega^2 R^2}{c^2}}\right) J_0(Ky)$$

and

$$u_1 = \frac{i\omega R}{c\alpha i^{3/2}} c_1 J_1(\alpha i^{3/2} y) - \frac{R}{\mu}\frac{i\omega R}{c}\left(\frac{A_1}{i^3\alpha^2 + \frac{\omega^2 R^2}{c^2}}\right) J_1(Ky),$$

with $A_1$ and $c_1$ constants.

**Specific Solution for radial velocity $u$ and axial velocity $w$** $J_1$ came from $\frac{dp}{dy}$. We can simplify further by assuming

$$\frac{\omega R}{c} \ll 1$$

By looking at typical values, we estimate the following

for humans

$$\omega = 2\pi, f = 1$$

for abdominal aorta

$$R \approx 1cm$$

$$C \approx 300 - 500 cm/s$$

Combining the above,

$$\frac{\omega R}{c} \sim \frac{2\pi}{300} \ll 1$$

.

Knowing that for small values of their arguments we have

$$J_0\left(\frac{i\omega R}{c} y\right) \approx 1$$

$$J_1\left(\frac{i\omega R}{c} y\right) \simeq \frac{1}{2}\frac{i\omega R}{c} y$$

and assuming pressure is constant across the vessel

$$p_1 = A_1$$

, we can now simplify further to

$$i^3\alpha^2 + \frac{\omega^2 R^2}{c^2} \approx i^3\alpha^2.$$

We now recall that

$$\alpha^2 = \frac{R^2\omega^2}{c^2} = \frac{\rho_0 R^2 \omega}{\mu},$$

so we have

$$w_1 = c_1 J_0(\alpha i^{3/2} y) - \frac{i\omega R^2 A_1}{c\mu i^3 \alpha^2}$$

$$w_1 = c_1 J_0(\alpha i^{3/2} y) + \frac{A_1}{\rho_0 c},$$

where $c_1$ is an arbitrary constant, which we now replace with $\frac{C_1}{J_0(\alpha i^{3/2})}$, so that

$$\boxed{w_1 = C_1 \frac{J_0(\alpha i^{3/2} y)}{J_0(\alpha i^{3/2})} + \frac{A_1}{\rho_0 c}}$$

and

$$u_1 = \frac{i\omega R}{c\alpha i^{3/2}} C_1 \frac{J_1(\alpha i^{3/2} y)}{J_0(\alpha i^{3/2})} - \frac{R}{\mu}(\frac{i\omega R}{c})\frac{A}{i^3\alpha^2}\frac{1}{2}\frac{i\omega R}{c} y$$

$$\boxed{u_1 = \frac{i\omega R}{2c}[C_1 \frac{2J_1(\alpha i^{3/2} y)}{\alpha i^{3/2} J_0(\alpha i^{3/2})} + y\frac{A_1}{\rho_0 c}]}.$$

We now have $u_1$, $w_1$ with unknown constants $A_1$ and $C_1$.

### 9.2.3 Couple fluid equations with vessel wall equations

We are now ready to couple the fluid and solid equations through their boundary conditions at the vessel wall interface. Recall that axial equation for the

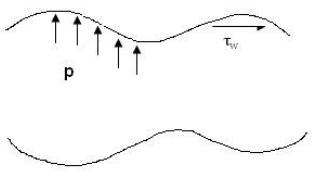


Figure 9.2: Pressure and shear stress applied on vessel wall

vessel wall is coupled to the fluid equations through the term $(\frac{1}{R}\frac{\partial w}{\partial y} + \frac{\delta u}{\delta z})_{y=1}$, and the radial equation of motion is coupled through the pressure $p$ and wall shear stress $\tau_w$.
We also have constraints that the fluid velocity must be the same as the wall velocity, so that

$$u = \frac{\partial \xi}{\partial t} \text{ at } y = 1, \text{ and} \tag{9.25}$$

$$w = \frac{\partial \zeta}{\partial t} \text{ at } y = 1 \tag{9.26}$$

We now calculate $\frac{\partial w}{\partial y}$ and $\frac{\partial u}{\partial z}$ at $y = 1$. Recall, $w = w_1 e^{i\omega(t-z/c)}$ so that

$$\frac{\partial w}{\partial y} = \frac{\partial w_1}{\partial y} e^{i\omega(t-z/c)} = \frac{C_1}{J_0(\alpha i^{3/2})} \frac{d}{dy}[J_0(\alpha i^{3/2} y)] e^{i\omega(t-z/c)} \tag{9.27}$$

$$= -\frac{C_1 \alpha i^{3/2}}{J_0(\alpha i^{3/2})} J_1(\alpha i^{3/2} y) e^{i\omega(t-z/c)} \tag{9.28}$$

For simplification, Womerseley defined the variable $F_{10}(\alpha) = \frac{2J_1(\alpha i^{3/2})}{\alpha i^{3/2} J_0(\alpha i^{3/2})}$, so we now have

$$\frac{\partial w}{\partial y}|_{y=1} = -\frac{C_1}{2} \alpha^2 i^3 F_{10}(\alpha) e^{i\omega(t-z/c)}. \tag{9.29}$$

Next, we need $\frac{\partial u}{\partial z}$, which we find from taking the derivative of

$$u = u_1 e^{i\omega(t-z/c)} \tag{9.30}$$

so that

$$\frac{\partial u}{\partial z} = u_1 (-\frac{i\omega}{c}) e^{i\omega(t-z/c)} \tag{9.31}$$

$$= -\frac{i\omega}{c}(\frac{i\omega R}{2c})[C_1\frac{2J_1(\alpha i^{3/2}y)}{\alpha i^{3/2}J_0(\alpha i^{3/2})} + y\frac{A_1}{\rho_0 c}]e^{i\omega(t-z/c)}. \tag{9.32}$$

Evaluating at $y = 1$

$$\frac{\partial u}{\partial z}|_{y=1} = \frac{\omega^2 R}{2c^2}[C_1 F_{10}(\alpha) + \frac{A_1}{\rho_0 c}]e^{i\omega(t-z/c)} \tag{9.33}$$

and combining with the above, we have

$$(\frac{1}{R}\frac{\partial w}{\partial y} + \frac{\partial u}{\partial z})|_{y=1} = [\frac{-C_1 F_{10}(\alpha)}{2R}(\alpha^2 i^3 - \frac{\omega^2 R^2}{c^2}) + \frac{\omega^2 R A_1}{2c^2\rho_0 c}]e^{i\omega(t-z/c)}. \tag{9.34}$$

Since $\frac{\omega R}{c} \ll 1$, we can neglect $\frac{\omega^2 R^2}{c^2}$ and $\frac{\omega^2 R}{c^3}$. Thus, we have

$$\left(\frac{1}{R}\frac{\partial w}{\partial y} + \frac{\partial u}{\partial z}\right)|_{y=1} = -\frac{C_1}{2R} i^3 \alpha^2 F_{10}(\alpha). \tag{9.35}$$

What about $u$ and $w$ at $y = 1$? We find these as follows

$$u|_{y=1} = u_1 e^{i\omega(t-z/c)} = \frac{i\omega R}{2c}[C_1 F_{10}(\alpha) + \frac{A_1}{\rho_0 c}]e^{i\omega(t-z/c)} \tag{9.36}$$

$$w|_{y=1} = w_1 e^{i\omega(t-z/c)} = (C_1 + \frac{A_1}{\rho_0 c})e^{i\omega(t-z/c)}. \tag{9.37}$$

Next we take the above expressions for $u|_{y=1}$ and $w|_{y=1}$ and set them equal to $\frac{\partial \xi}{\partial t}$ and $\frac{\partial \zeta}{\partial t}$ to couple the fluid and solid mechanics equations.

First, we assume solutions for the displacement variables of the form

$$\xi = D_1 e^{i\omega(t-\frac{z}{c})} \tag{9.38}$$

$$\zeta = E_1 e^{i\omega(t-\frac{z}{c})} \tag{9.39}$$

$$\frac{\partial \xi}{\partial t} = i\omega D_1 e^{i\omega(t-\frac{z}{c})} \tag{9.40}$$

$$\frac{\partial \zeta}{\partial t} = i\omega E_1 e^{i\omega(t-\frac{z}{c})}. \tag{9.41}$$

Enforcing kinematic constraints, we have

$$u = \frac{\partial \xi}{\partial t} \ , \ w = \frac{\partial \zeta}{\partial t} \ \ at \ y = 1 \tag{9.42}$$

for $u$:

$$\frac{i\omega R}{2c}\left[C_1 F_{10}(\alpha) + \frac{A_1}{\rho_0 c}\right] e^{i\omega(t-\frac{z}{c})} = i\omega D_1 e^{i\omega(t-\frac{z}{c})} \tag{9.43}$$

or

$$i\omega D_1 = \frac{1}{2}\frac{i\omega R}{c}\left[C_1 F_{10}(\alpha) + \frac{A_1}{\rho_0 c}\right] \tag{9.44}$$

and for $w$:

$$\left(C_1 + \frac{A_1}{\rho_0 c}\right) e^{i\omega(t-\frac{z}{c})} = i\omega E_1 e^{i\omega(t-\frac{z}{c})} \tag{9.45}$$

so

$$i\omega E_1 = C_1 + \frac{A_1}{\rho_0 c}. \tag{9.46}$$

We now insert the above expressions for $\xi$ and $\zeta$ into the governing equations for the vessel wall, which we recall as

$$\frac{\partial^2 \xi}{\partial t^2} = \frac{p}{\rho h} - \frac{B}{\rho}\left(\frac{\xi}{R^2} + \frac{\sigma}{R}\frac{\partial \zeta}{\partial z}\right) \tag{9.47}$$

$$\frac{\partial^2 \zeta}{\partial t^2} = -\frac{\mu}{\rho h}\left(\frac{1}{R}\frac{\partial w}{\partial y} + \frac{\partial u}{\partial z}\right)|_{y=1} + \frac{B}{\rho}\left(\frac{\partial^2 \zeta}{\partial z^2} + \frac{\sigma}{R}\frac{\partial \xi}{\partial z}\right), \tag{9.48}$$

yielding, for the radial equation

$$-\omega^2 D_1 = \frac{A_1}{\rho h} - \frac{B}{\rho}\left(\frac{D_1}{R^2} - \frac{\sigma}{R}\frac{i\omega}{c}E_1\right). \tag{9.49}$$

Rearraging the radial equation:

$$\frac{c^2}{R^2}(-\frac{\omega^2 R^2}{c^2} + \frac{B}{\rho c^2})D_1 = \frac{A_1}{\rho}h + \frac{B\sigma i\omega}{\rho R c}E_1. \tag{9.50}$$

We can simplify the radial equation by neglecting $\frac{\omega^2 R^2}{c^2}$:

$$\frac{B}{R^2\rho}D_1 = \frac{A_1}{\rho h} + \frac{B\sigma i\omega}{\rho R c}E_1. \tag{9.51}$$

For the axial equation:

$$-\omega^2 E_1 = -\frac{\mu}{\rho h}\left\{\frac{-C_1}{2R}i^3\alpha^2 F_{10}(\alpha) + \frac{1}{2}\frac{\omega^2 R}{c^2}\frac{A_1}{\rho_0 c}\right\} + \frac{B}{\rho}\left\{\left(\frac{i\omega}{c}\right)^2 E_1 + \frac{\sigma}{R}\left(\frac{-i\omega}{c}\right)D_1\right\}. \tag{9.52}$$

We now have 4 equations and 4 unknowns $A_1, C_1, D_1, E_1$. We still need the wave speed c. Putting the system into matrix form, we have

$$\begin{bmatrix} \frac{1}{\rho_0 c} & 1 & 0 & -i\omega \\ \frac{i\omega R}{2\rho_0 c^2} & \frac{i\omega R}{2c}F_{10}(\alpha) & -i\omega & 0 \\ \frac{1}{\rho h} & 0 & -\frac{B}{\rho R^2} & \frac{i\omega B\sigma}{\rho R c} \\ 0 & \frac{\mu i^3\alpha^2 F_{10}(\alpha)}{2R\rho h} & \frac{-i\omega\sigma B}{\rho R c} & \omega^2\left(1-\frac{B}{\rho c^2}\right) \end{bmatrix} \begin{bmatrix} A_1 \\ C_1 \\ D_1 \\ E_1 \end{bmatrix} = \begin{bmatrix} 0 \\ 0 \\ 0 \\ 0 \end{bmatrix}$$

For a non-trivial solution we must have det [ ]=0

This requirement yields the following equation that can be used to find the wave speed

$$\left[\left(F_{10}(\alpha)-1\right)\left(\sigma^2-1\right)\right]\eta^2 + \left[\frac{\rho h}{\rho_0 R}\left(F_{10}(\alpha)-1\right) + \left(2\sigma - \frac{1}{2}\right)F_{10}(\alpha) - 2\right]\eta + \frac{2\rho h}{\rho_0 R} + F_{10}(\alpha) = 0, \tag{9.53}$$

where

$$\eta = \frac{Bh}{\rho R c^2} \qquad F_{10} = \frac{2J_1\left(\alpha i^{3/2}\right)}{\alpha i^{3/2} J_0\left(\alpha i^{3/2}\right)} \qquad \Lambda = \alpha i^{3/2} \tag{9.54}$$

The frequency equation gives an expression for the wave speed as a function of material properties and frequency.

Recall for the inviscid case the wave speed was

$$c_0^2 = \frac{Eh}{2\rho_0 R}. \tag{9.55}$$

Then

$$\eta = \frac{Bh}{\rho R c^2} = \frac{2Eh}{2\left(1-\sigma^2\right)\rho_0 R c^2} = \frac{2}{\left(1-\sigma^2\right)}\frac{c_0^2}{c^2}. \tag{9.56}$$

The above equation has two solutions, and only one is physical so that

$$c = \sqrt{\frac{2}{\eta(1-\sigma^2)}}c_0. \tag{9.57}$$

Since c is complex (not a true physical speed), we decompose it into real and imaginary parts as

$$\frac{1}{c} = \frac{1}{c_R} + i\frac{1}{c_I} \tag{9.58}$$

or

$$e^{i\omega(t-\frac{z}{c})} = e^{i\omega(t-\frac{z}{c_R}-i\frac{z}{c_I})} = e^{\frac{\omega}{c_I}}e^{i\omega(t-\frac{z}{c_R})}. \tag{9.59}$$

In the above solution,

$e^{\frac{\omega}{c_I}}$ is the amplitude change from the imaginary part (attenuation) and is not present in the inviscid case, and

$e^{i\omega(t-\frac{z}{c_R})}$ is called the dispersion and is the phase change due to the real part.

### 9.2.4 Determining the final Womersley solution

The matrix equation we derived for the constants is rank 3. Once the wave speed is obtained, we then specify the value for one of the constants and then solve the matrix system to find the other three constants. We will choose to define the prescribed amplitude for the input oscillatory pressure ($A_1$), which enables us to then solve for $C_1$, $D_1$, $E_1$, and eliminate $A_1$.

The final expression for the axial velocity is then

$$w(r,z,t) = \frac{A_1}{\rho c}\left[1 - G\frac{J_0\left(\frac{\Lambda r}{R}\right)}{J_0(\Lambda)}\right] e^{i\omega(t-\frac{z}{c})}, \tag{9.60}$$

where $G$ is the elasticity factor defined by

$$G = \frac{2+\eta(2\sigma-1)}{\eta(2\sigma - F_{10})}. \tag{9.61}$$

We note that $G$ is a complex number, and that its real and Imaginary parts depend on frequency.

and the final expression for the radial velocity is

$$u(r,z,t) = \frac{A_1 i\omega R}{2\rho_0 c^2}\left[\frac{r}{R} - G\frac{2J_1\left(\frac{\Lambda r}{R}\right)}{\Lambda J_0(\Lambda)}\right] e^{i\omega(t-\frac{z}{c})}. \tag{9.62}$$

# Chapter 10

# Patient Specific Modeling

Cardiovascular blood flow simulations offer a powerful, non-invasive means to augment the knowledge gained from medical imaging and clinical measurements to positively impact clinical decision-making. Simulations fill several crucial gaps in current clinical capabilities. First, despite recent advances in medical imaging, leading to ever-increasing resolution, imaging is not a predictive tool. Simulations have potential to predict the outcome of treatments, enabling systematic testing, optimization, and personalization. Second, and perhaps equally importantly, simulations can be used to characterize the *in vivo* mechanical environment, providing missing data on hemodynamics and mechanical stimuli that are not directly attainable from medical imaging. These data are a key component of the mechanobiological puzzle relating mechanical environment to subsequent disease progression. Filling these gaps requires efficient and accurate multiscale numerical tools to solve the equations of blood flow, which may also be coupled to governing equations for physiology, vessel wall mechanics and biological processes.

Analysis and simulation of blood flow necessitates a combination of image analysis and model construction, boundary condition (BC) and material property selection, accurate solution of the governing equations, physiology models, and high-performance computing. Patient specific cardiovascular simulations typically begin with 3D reconstruction of a portion of the vascular anatomy from CT or MRI image data, and progress through stages of meshing, BC and parameter assignment, hemodynamic simulation and flow

analysis. This produces a wealth of data from which we aim to extract clinically relevant information to improve patient care. Since only a portion of a patient's anatomy can be included in the 3D model, both due to computational expense and limits of image resolution, BCs must be applied at inlets and outlets of the model to accurately represent the vascular network outside of the 3D domain.

Patient specific modeling has been applied to numerous cardiovascular diseases, with varying degrees of clinical impact. Recent applications have included new surgical designs for congenital heart disease [49, 45, 7, 12, 13, 42], risk assessment in coronary artery disease [53, 58], thrombotic risk stratification in Kawasaki disease [60], and cerebral and abdominal aneurysm rupture risk and treatment [44, 9]. Device simulations have included evaluation of wall shear stress patterns in stents [40, 41], stent optimization [23, 24], ventricular assist devices [47], device migration [16], and pacemaker lead placement [48]. Validation studies have demonstrated good agreement between simulations and in vitro models, including mock circulatory systems [38, 68]. However, validation against *in* vivo data remains sorely lacking in the literature. Barriers to further clinical adoption include a lack of validation and uncertainty quantification, the need for large scale clinical trials to demonstrate reliability and improved outcomes, and the need for more efficient modeling and simulation methods.

Numerical simulations in cardiovascular disease present a number of important challenges, necessitating specialized algorithm development to maintain solver performance and numerical stability. First, multiscale modeling methods incorporating dynamic coupling between local hemodynamics and circulatory physiology result in ill-conditioned systems dominated by a few eigenvalues coming from the coupled boundaries. These systems must be handled carefully to maintain numerical stability with reasonable computational cost. Second, computational expense becomes increasingly important when coupling simulations to optimization and uncertainty quantification, when numerous simulations are required, and with fluid structure interaction. Third, high aspect ratio complex geometries and coupled boundaries present a challenge for conventional linear solvers due to ill conditioning and convergence challenges. We focus this review on recent developments in numerical algorithms that address these three key challenges.

Blood flow is governed by the incompressible Naiver-Stokes equations

$$\rho \dot{\boldsymbol{u}} + \rho \boldsymbol{u} \cdot \nabla \boldsymbol{u} - \nabla \cdot \boldsymbol{T} = 0,$$

$$\nabla \cdot \boldsymbol{u} = 0, \tag{10.1}$$

where $\rho$, $\dot{\boldsymbol{u}}$, and $\boldsymbol{u}$ are the density, velocity time derivative, and velocity vector, respectively. Flow is typically modeled as an incompressible, Newtonian fluid in large vessels, in which the stress tensor, $\boldsymbol{T}$, is expressed by

$$\boldsymbol{T} = -p\boldsymbol{I} + \mu(\nabla \boldsymbol{u} + \nabla \boldsymbol{u}^{\mathrm{T}}), \tag{10.2}$$

where $p$ is the pressure. While blood is a non-Newtonian shear thinning fluid, a Newtonian assumption generally holds in large vessels, in which viscosity, $\mu$, is considered constant. The reader is referred to other relevant discussions of non-Newtonian effects in blood flow relevant in small vessels [22, 25].

## 10.1 Geometric Model Construction

Patient specific simulations are typically performed on three-dimensional models of vascular anatomy that are derived from patient image data. Depending on the disease application, either CT or MRI data is typically used. Image data may be segmented using 2D or 3D level set or thresholding methods. Common packages for image segmentation include open source packages such as Simvascular (simtk.org) or ITK-SNAP, or commercial packages such as Mimics (Materialise, Leuven, Belgium). The typical steps for model construction using 2D methods are 1) create paths along vessels of interest, 2) manually or automatically draw segmentations of the vessel lumen at discrete locations along the paths, 3) loft (interpolate) the segmentations together to create a 3D solid model, and 4) mesh the model for use with a CFD solver. Advantages of 2D methods are the ability to smoothly represent vascular tree-like branching patterns, such as occur in the pulmonary arteries. Advantages of 3D methods include the ability to more readily capture details of local complex geometry, particularly in aneurysms or complex surgical connections. Ultimately, a combination of both methods will likely prove most advantageous in many disease applications. While automated methods do exist for both 2D and 3D segmentation, noise in the image data often

leads to significant user intervention and the need for manual segmentation. Automated segmentation methods enhanced by machine learning algorithms have been shown to greatly improve efficiency, reduce user input, and enable high-throughput model construction for clinical applications.

## 10.2 Hemodynamics Simulations

Both finite element and finite volume methods have been used to solve the Navier-Stokes equations in cardiovascular applications. Finite element methods (FEM), which are most widely used, are well suited to complex geometries with unstructured meshes. Most recent work has used stabilized (SUPG) methods with linear elements, but higher order elements have also been employed. In the FEM approach, the weak form of the Navier-Stokes equations is solved. While commercial solvers can be used on a limited basis, custom solvers offer more flexibility and control over boundary condition implementation, which is essential for obtaining an accurate solution.

Immersed boundary methods, introduced by Peskin in the 1970s, offer an attractive alternative in many situations, and have been successfully applied to heart mechanics and device design. These methods offer the advantage of using structured grids for improved solver efficiency, but the disadvantage of limited mesh resolution in key areas such as near-wall boundary layers. They are particularly attractive for fluid-structure interaction problems. Unstructured finite volume methods also offer an attractive alternative to FEM methods, particularly with non-commercial codes that do not require additional stabilization terms. These methods have been shown to more accurately capture cycle to cycle variations in unsteady flow in aneurysms, showing surprising evidence of turbulence at low Reynolds numbers.

### 10.2.1 Boundary Condition Assignment

The choice of boundary conditions is of paramount importance in cardiovascular simulations, as the local flow dynamics are greatly influenced by conditions upstream and downstream of the 3D model. Numerous studies have demonstrated drastic differences in flow solutions, even with simple geome-

tries, and particularly in models with multiple outlets. Commonly used outlet boundary conditions such as zero-pressure or zero-traction, while easiest to implement, are well known to lead to unrealistic solutions, in part because of their inability to capture physiologic levels of pressure. These methods should not be used for fluid-structure interaction problems where the wall deformation depends directly on the pressure level in the vessel. Vascular resistance in arterioles and capillaries is largely responsible for determining blood pressure levels in large arteries. The same vascular resistances are also responsible for regulating the distribution of blood flow to different regions of the body. A fluid dynamic simulation of large arteries, without consideration of the smaller downstream vessels, neglects these important effects.

A typical choice of inlet BC is to impose a prescribed pressure or flow waveform. Typical choices for outlets are zero pressure or zero traction conditions, resistance or impedance conditions, reduced order models which can be open or closed loop, or reduced order one-dimensional wave propagation equations [66, 67, 19]. A closed-loop approach can also be taken, in which all boundaries of the 3D model are coupled to a lumped parameter network. These BCs are imposed on equation (10.1) via a Dirichlet condition

$$\boldsymbol{u} = \boldsymbol{g},\ \boldsymbol{x} \in \Gamma_{\mathrm{g}}, \tag{10.3}$$

or a Neumann condition

$$\boldsymbol{T} \cdot \boldsymbol{n} = \boldsymbol{h},\ \boldsymbol{x} \in \Gamma_{\mathrm{h}}, \tag{10.4}$$

in which $\Gamma_{\mathrm{g}}$ and $\Gamma_{\mathrm{h}}$ denote Dirichlet and Neumann boundaries, respectively. Note that $\boldsymbol{g}$ and $\boldsymbol{h}$ are a prescribed function of $\boldsymbol{x}$ and $t$ for uncoupled BCs (e.g. zero traction), whereas they are also a function of $\boldsymbol{u}$ and $p$ for complex reduced order models (e.g. closed-loop heart models).

### Inflow Boundaries

Inflow boundary conditions are typically enforced at the inlet of the 3D model, and three choices are commonly available. The simplest choice is to use a plug flow condition, applying a uniform velocity profile. However, this assumption is known to be invalid for flow in a pipe, particularly in unsteady flow. A more realistic choice is to impose a parabolic flow profile

using the Poiseuille solution for flow in a circular pipe, a well known analytical solution of the Navier-Stokes equations in cylindrical coordinates that was derived in Chapter 3

### Outflow Boundaries

To capture the interaction between the local 3D domain and the global circulation, the 3D Navier-Stokes solver must be coupled to a reduced order LPN model [17, 42]. In constructing the LPN, we make an analogy to electrical circuits, in which pressure drop is modeled with resistors, vessel distensibility is modeled with capacitors, and flow inertia is modeled with inductors. The RCR (Windkessel) circuit is commonly adopted as an outlet BC to model the distal vasculature with one capacitor modeling vessel compliance and two resistors modeling proximal and distal pressure drops (Figure 10.1) [67]. Diodes and other specialized components may also be included to model heart valves and elastance of heart chambers [1]. As some circuit components are time dependent, e.g. due to the presence of inductors and capacitors, the circuit is represented by a set of time dependent ordinary differential equations (ODE). Combining these equations produces a single ODE with order equal to the number of time dependent components in the circuit.

For simple circuits with low order ODE, an analytical solution can be obtained, as is the case with simple resistors, RCR (Windkessel) circuits, and coronary artery models [35, 36], which are commonly used as outlet BCs in an open-loop configuration. Models can be expanded to a full closed-loop networks that can then be coupled to the 3D domain [42, 11]. A closed-loop lumped-parameter model has the advantage that the effects from the global circulation are fully coupled to influence the overall simulated physiology. Figure 10.2 shows an example of closed-loop and open-loop multi-scale simulation setups.

In an open loop configuration, flow rate at the inlet is generally prescribed, and therefore must be available from clinical data. In a closed-loop configuration, however, the 3D domain inflow is not prescribed, but is extracted from the 0D domain ODE solution, incorporating the responses of the heart and global physiology to altered flow conditions at the 3D-0D interface. In a closed-loop scenario, the 3D domain presents itself to the 0D model as

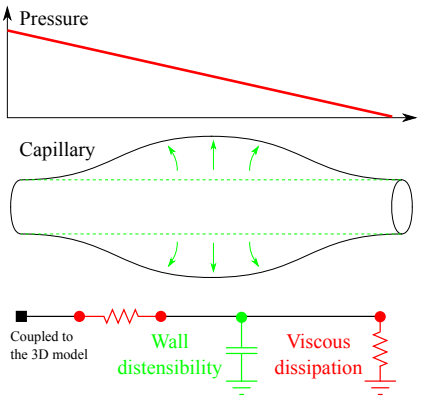


Figure 10.1: Schematic of a RCR (Windkessel) circuit for modeling the 0D domain vasculature. The wall distensibility is modeled by including a capacitor, which stores blood as pressure increases. Pressure drop due to viscous dissipation is modeled using two resistors to model the proximal and distal vessels.

a set of time-varying resistance, inductance, and capacitance (in the case of deformable wall simulation) that are functions of the 3D domain hemodynamics. The 0D model behavior is affected by this 3D model behavior, and thus provides BCs that are fully coupled to the 3D domain, forming a complete feedback loop.

Closed-loop multi-scale models have been particularly useful in modeling coronary flows, as well as complex surgeries in pediatric cardiology applications [50, 37, 58]. For example, the effects of a surgical shunt in single ventricle patients can be investigated using such a model, which enables considerations of how the shunt resistance influences the balance of blood flow through various pathways in light of systemic resistances and heart behavior [14].

### Coupled Boundaries

After defining the physics of the 3D and reduced-order domains, the coupled system must be solved by a numerical method that is both stable and modular. Stability is important, as these simulations are highly vulnerable to

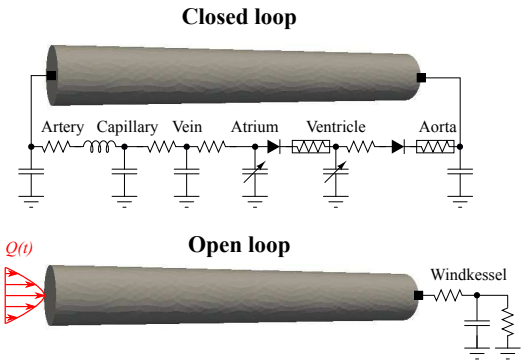


Figure 10.2: Comparison between a closed-loop and open-loop lumped-parameter model. A dirichlet BC is prescribed at the inlet in the open-loop configuration, fixing the flow rate to a user-defined value (or waveform in the case of unsteady flow), whereas flow rate dynamically changes depending on the coupled behavior of the 3D and 0D domains in the closed-loop configuration. With the closed-loop configuration, additional information, for example cardiac work load or pressure volume loops, can be extracted from the 0D domain.

rapid changes in flow conditions at the boundary interfaces and also to the unpredictable behavior of the two-way coupling. Reducing time step size to improve stability is not always a viable solution, as it significantly increases simulation cost. Modularity also becomes important when one wishes to consider a wide range of reduced order models that can be adopted by an end-user. The coupling framework must therefore be simple, practical, and universal, enabling the end-user to seamlessly couple any desired reduced-order domain to the 3D domain. Here, we focus on 0D LPN models as the choice of reduced-order model, since 0D models are widely adopted for their simpler construction from the available clinical data. However, we note that these methods can be extended to 1D models by replacing the ODE governing the 0D model with partial differential equations governing the 1D model, while keeping the coupling scheme unchanged.

Depending on the complexity and order of the ODE network governing the LPN, one may use either a monolithic or a coupled approach for solution of the 0D-3D coupled system. A monolithic approach can be used when the

analytical solution of the ODE of 0D model is known [66]. The analytic relationship between pressure and flow (i.e. the Dirichlet-to-Neumann map) is then implemented directly in the numerical solver and the entire problem, i.e. 3D and 0D together, is implemented in a single solver and solved simultaneously. The monolithic approach is now widely accepted with details described by Vignon-Clementel and others [66, 67]. The monolithic approach is best suited to simple models, at most containing few time dependent components, such as resistance and RCR circuits [67]. However, since the 0D model is hard coded inside the 3D solver in the monolithic approach, any alteration to the 0D circuit requires intrusive implementation in the 3D solver by the end-user, requiring intimate knowledge of the solver that may not be appropriate for all end-users. This approach may also produce an ill-conditioned numerical system in certain cases [64, 6].

For more complex circuit networks, obtaining the analytical solution of a high-order nonlinear ODE is not practical, and the system must be solved numerically to obtain the Dirichlet-to-Neumann relationship. Use of the monolithic approach is no longer practical in this case, and partitioned approaches have been introduced by several groups [51, 29, 39]. The key concept of the partitioned approach is to have a separate solver for the 0D domain that is coupled to the 3D solver through a well-defined interface. Separation of the two domains inherently removes the need for altering the 3D solver for different 0D models, hence existing 3D solvers can be used with a minimal one-time change. Numerical solution of the ODEs in the 0D solver, for example with a Runge Kutta time stepping scheme, enables simulation of circuits with multiple time-dependent and nonlinear components, and multiple organ blocks. The partitioned approach also allows flexibility in the choice of numerical schemes for the 3D and 0D solvers. Therefore, a wide variety of schemes, such as explicit [56], Gauss-Seidel with sub-iterations between the two domains [18, 64], and Newton's method with two nonlinear iteration loops [43] have been proposed in this context.

Here, we briefly describe a coupling method with several attractive properties of the partitioned approach. Numerical instability due to the separation of the 0D and 3D solvers, which is a concern in many partitioned approaches, is addressed by including the contribution of the 0D model in the 3D solver tangent matrix [51]. By improving stability, the limitation associated with restrictive time step choice is alleviated, thus combining attractive features

of both monolithic and partitioned approaches.

The velocity and pressure field in the 3D domain can be solved via equation (10.1) once the coupled boundaries $\boldsymbol{h}$ and $\boldsymbol{g}$ from equations (10.4) and (10.3), respectively, are known. Let us define the coupled Neumann and Dirichlet boundary indices as $\eta_{\mathrm{h}} = \{1, 2, ..., n_{\mathrm{h}}\}$ and $\eta_{\mathrm{g}} = \{1, 2, ..., n_{\mathrm{g}}\}$, where $n_{\mathrm{h}}$ and $n_{\mathrm{g}}$ are the number of coupled Neumann and Dirichlet boundaries, respectively. $\boldsymbol{h}$ and $\boldsymbol{g}$ for the coupled surfaces are defined as

$$\boldsymbol{h}(\boldsymbol{u}, p; \boldsymbol{x}, t) = -\mathcal{P}^i \boldsymbol{n},\ \boldsymbol{x} \in \Gamma^i,\ i \in \eta_{\mathrm{h}} \tag{10.5}$$

$$\boldsymbol{g}(\boldsymbol{u}, p; \boldsymbol{x}, t) = \left( \int_{\Gamma^i} \phi \mathrm{d}\Gamma \right)^{-1} \phi(\boldsymbol{x}, t) Q^i \boldsymbol{n},\ \boldsymbol{x} \in \Gamma^i,\ i \in \eta_{\mathrm{g}} \tag{10.6}$$

where $\Gamma^i$ is the boundary of surface $i$ and $\phi(\boldsymbol{x}, t)$ is a prescribed velocity profile. $\phi(\boldsymbol{x})$ with a flat or parabolic profile is among the popular choices. The flow rate, $Q^i,\ i \in \eta_{\mathrm{g}}$, and spatially averaged pressure, $\mathcal{P}^i,\ i \in \eta_{\mathrm{h}}$, of the coupled boundaries must be calculated by the 0D solver. In general an explicit function does not exist or must be solved numerically for these quantities by

$$\dot{\boldsymbol{\mathcal{X}}} = \boldsymbol{A}(Q^i, \mathcal{P}^j, t; \boldsymbol{\mathcal{X}}) \boldsymbol{\mathcal{X}} + \boldsymbol{b}(Q^i, \mathcal{P}^j, t),\ i \in \eta_{\mathrm{h}},\ j \in \eta_{\mathrm{g}}, \tag{10.7}$$

where $\boldsymbol{\mathcal{X}}$ are the unknowns in the 0D domain. Note that for lumped parameter models containing nonlinear components, $\boldsymbol{A}$ is a function of $\boldsymbol{\mathcal{X}}$. To solve equation (10.7), flow rates at the coupled Neumann boundaries, $Q^i,\ i \in \eta_{\mathrm{h}}$, and pressures at the coupled Dirichlet boundaries, $\mathcal{P}^i,\ i \in \eta_{\mathrm{g}}$, are needed. These values need to be passed from the 3D to the 0D solver. A variety of methods can be used to integrate $\boldsymbol{\mathcal{X}}$ in equation (10.7). Since this integration is cheap relative to the 3D domain calculations, each 3D time step can be divided into sub-time steps to increase accuracy and stability of the 0D calculations, facilitating the use of explicit methods such as Runge-Kutta. The pressure at coupled Neumann boundaries and flow rate at coupled Dirichlet boundaries can be directly extracted from $\boldsymbol{\mathcal{X}}$, once equation (10.7) is solved. The data exchange and time integration of the 3D and 0D domains is schematically shown in Figure 10.3. To ensure convergence of both domains simultaneously, data are exchanged iteratively at each Newton-Raphson iteration of the 3D solver. Having access to the interface flow and pressure at $n$ and $n+1$ allows for an implicit time-integration scheme in the 0D domain.

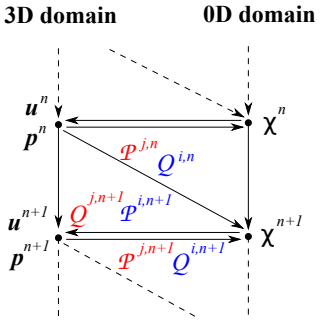


Figure 10.3: Schematic of time marching in the 3D and 0D domains. The 0D domain sends corrected $\mathcal{P}^{i,n+1}$ and $Q^{j,n+1}$ to the 3D domain and receives $Q^{i,n}$ and $\mathcal{P}^{j,n}$ and the corrected $Q^{i,n+1}$ and $\mathcal{P}^{j,n+1}$ values from the 3D domain. Simulation is performed iteratively and proceeds to the next time step only when the coupled system is converged. Neumann boundary ($i \in \eta_{\mathrm{h}}$) values are colored blue and Dirichlet boundary ($j \in \eta_{\mathrm{g}}$) values are colored red.

To avoid instabilities, it is essential to impose a Neumann boundary in the 3D domain if a capacitor is used at the 0D domain interface or a Dirichlet boundary if an inductance is used at the interface. Coupled Neumann boundary $i$ can have a contribution in the tangent matrix of the 3D domain if its pressure, $\mathcal{P}^i$, depends on its flow rate, $Q^i$. Neglecting this contribution, as is often the case in explicit methods, leads to instabilities. Defining $\boldsymbol{K}$ as a block of the tangent matrix that relates the momentum equation to the velocity, we calculate the contribution of the Neumann boundaries to $\boldsymbol{K}$, i.e. $\boldsymbol{K}_{\mathrm{BC}}$, to obtain an implicit scheme that is more robust. $\boldsymbol{K}_{\mathrm{BC}}$ is calculated using the Newton-Raphson method, in which the momentum residual vector, $\boldsymbol{R}_{\mathrm{m}}$, is differentiated with respect to the velocity solution

$$\boldsymbol{K}^{ab} = \boldsymbol{K}^{ab}_{\mathrm{3D}} + \boldsymbol{K}^{ab}_{\mathrm{BC}} = \boldsymbol{K}^{ab}_{\mathrm{3D}} + \frac{\partial \boldsymbol{R}^a_{\mathrm{m}}}{\partial \boldsymbol{y}^b_{\mathrm{u}}}, \tag{10.8}$$

where $\boldsymbol{y}_{\mathrm{u}}$ is the solution of the system of linear equations, which is proportional to the velocity correction, $a$ and $b$ are indices for mesh nodal points, and $\boldsymbol{K}_{\mathrm{3D}}$ is the 3D domain contribution to $\boldsymbol{K}$. We can then obtain

$$\boldsymbol{K}^{ab} = \boldsymbol{K}^{ab}_{\mathrm{3D}} + \gamma \Delta t M_{ij} \int_{\Gamma_i} N^a \boldsymbol{n} \mathrm{d}\Gamma \otimes \int_{\Gamma_j} N^b \boldsymbol{n} \mathrm{d}\Gamma, \tag{10.9}$$

in which $N^a(\boldsymbol{x})$ is the shape function for node $a$, $\gamma$ is a time integration constant, $\Delta t$ is the time step size, and $M^{ij}$ is an $n_\mathrm{h} \times n_\mathrm{h}$ resistance matrix. Since an analytical relation for $\mathcal{P}^i$ $i \in \eta_\mathrm{h}$ is not generally available, $\boldsymbol{M}$ must be approximated by

$$M^{ij} = \frac{\partial \mathcal{P}^{i,n+1}}{\partial Q^{j,n+1}} \approx \frac{\mathcal{P}^{i,n+1}(Q^{j,n+1} + \epsilon) - \mathcal{P}^{i,n+1}(Q^{j,n+1})}{\epsilon}, \tag{10.10}$$

with

$$\epsilon = \max\{\epsilon_\mathrm{abs}, \epsilon_\mathrm{rel} \left|Q^{j,n+1}\right|\}. \tag{10.11}$$

Generally, the off-diagonal entries of $M^{ij}$ are negligible compared to the diagonal terms and

$$\mathcal{R}^i = \gamma \Delta t M^{ii}, \tag{10.12}$$

can substitute for $\boldsymbol{M}$ in equation (10.9) as a good approximation. Physically, the added contribution to $\boldsymbol{K}$ in equation (10.8) allows the 3D domain to predict the 0D domain behavior, hence improving the stability of the entire scheme. While the presented coupling method enables construction of an iterative scheme, increasing the value of resistance $\mathcal{R}^i$ produces an ill-conditioned $\boldsymbol{K}$, leading to poor performance of the iterative linear solver.

### Fluid Structure Interaction

Deformation of the vessel walls can be included via fluid-structure interaction (FSI) simulations, in which the solid and fluid domain problems are solved simultaneously using either iterative coupling or strong coupling, as in arbitrary lagrangian-eulerian (ALE) methods. Strongly coupled methods are particularly attractive for large deformation problems, including membrane buckling, valves and ventricular mechanics. However, their computational cost can make them prohibitively expensive for some applications. Immersed boundary methods offer an attractive alternative, which allows for use of structured mesh solvers in problems with complex geometries. Other approaches to reduce computational cost include the coupled momentum method of Figueroa and Taylor, which relies on a small deformation approximation based on Womersley theory to impose forces on the fluid domain without requiring mesh motion.

Recent advances in FSI include the coupled momentum method [15, 72], which enables efficient simulations within the limit of small deformations and

a linear elastic material model, and the Arbitrary Lagrangian Eulerian (ALE) method allowing for large deformations, more complex material models, and mesh motion [5, 2]. ALE methods are particularly attractive for membrane buckling, valves and ventricular mechanics, but often incur higher computational cost. Immersed boundary methods, originally motivated by the need for methods to handle cardiac fluid mechanics, are also widely used for ventricular fluid mechanics, valve simulations, and medical device simulations [55]. Isogeometric methods also hold promise for integration of design and simulation in cardiovascular models [2, 4, 3].

# Bibliography


[1] R Balossino, G Pennati, Francesco Migliavacca, L Formaggia, A Veneziani, M Tuveri, and Gabriele Dubini. Computational models to predict stenosis growth in carotid arteries: Which is the role of boundary conditions? *Computer Methods in Biomechanics and Biomedical Engineering*, 12(1):113–123, February 2009.

[2] Y Bazilevs, V M Calo, T J R Hughes, and Y Zhang. Isogeometric fluid-structure interaction: theory, algorithms, and computations. *Computational Mechanics*, 43(1):3–37, December 2008.

[3] Y Bazilevs, VM Calo, Y Zhang, and Thomas JR Hughes. Isogeometric fluid–structure interaction analysis with applications to arterial blood flow. *Computational Mechanics*, 38(4-5):310–322, 2006.

[4] Y. Bazilevs, J.R. Gohean, T.J.R. Hughes, R.D. Moser, and Y. Zhang. Patient-specific isogeometric fluid-structure interaction analysis of thoracic aortic blood flow due to implantation of the Jarvik 2000 left ventricular assist device. *Computer Methods in Applied Mechanics and Engineering*, 198(45-46):3534–3550, 2009.

[5] Y. Bazilevs, M.C. Hsu, D.J. Benson S. Sankaran, and A.L. Marsden. Computational fluid–structure interaction: methods and application to a total cavopulmonary connection. *Computational Mechanics*, 45(1):77–89, 2009.

[6] P.J. Blanco, R.A. Feijoo, and S.A. Urquiza. A unified variational approach for coupling 3D-1D models and its blood flow applications. *Computer Methods in Applied Mechanics and Engineering*, 196(41-44):4391–4410, 2007.

[7] E.L. Bove, F. Migliavacca, M.R. de Leval, R. Balossino, G. Pennati, T.R. Lloyd, S. Khambadkone, T.Y. Hsia, and G. Dubini. Use of mathematic modeling to compare and predict hemodynamic effects of the modified blalock–taussig and right ventricle–pulmonary artery shunts for hypoplastic left heart syndrome. *The Journal of Thoracic and Cardiovascular Surgery*, 136(2):312–320, 2008.

[8] C. G. Caro, J. M. Fitz-Gerald, and R. C. Schroter. Atheroma and arterial wall shear: observation, correlation and proposal of a shear dependent mass transfer mechanism for atherogenesis. *Proceedings of the Royal Society of London Series B: Biological Sciences*, 177:109–159, 1971.

[9] M. A. Castro, C. M. Putman, and J. R. Cebral. Computational fluid dynamics modeling of intracranial aneurysms: effects of parent artery segmentation on intra-aneurysmal hemodynamics. *AJNR Am J Neuroradiol*, 27(8):1703–9, 2006.

[10] A. J. Chorin and J. E. Marsden. *A mathematical introduction to fluid mechanics*. Springer, 1993.

[11] C. Corsini, D. Cosentino, G. Pennati, G. Dubini, T.Y. Hsia, and F. Migliavacca. Multiscale models of the hybrid palliation for hypoplastic left heart syndrome. *Journal of Biomechanics*, 44(4):767–770, 2011.

[12] L.P. Dasi, K. Pekkan, H.D. Katajima, and A.P. Yoganathan. Functional analysis of Fontan energy dissipation. *Journal of Biomechanics*, 41(10):2246–2252, 2008.

[13] M. R. de Leval, P. Kilner, M. Gewillig, and C. Bull. Total cavopulmonary connection: a logical alternative to atriopulmonary connection for complex Fontan operations. experimental studies and early clinical experience. *J. Thorac. Cardiovasc. Surg.*, 96:682–695, 1988.

[14] Mahdi Esmaily Moghadam, Francesco Migliavacca, Irene E Vignon-Clementel, Tain-Yen Hsia, Alison L Marsden, and Modeling of Congenital Hearts Alliance (MOCHA) Investigators. Optimization of Shunt Placement for the Norwood Surgery Using Multi-Domain Modeling. *Journal of Biomechanical Engineering*, 134(5):051002, 2012.

[15] C. A. Figueroa, I. E. Vignon-Clementel, K. E. Jansen, T. J.R. Hughes, and C. A. Taylor. A coupled momentum method for modeling blood flow in three-dimensional deformable arteries. *Comput. Meth. Appl. Mech. Engrg.*, 195(41-43):5685–5706, 2006.

[16] C.A. Figueroa, C.A. Taylor, A.J. Chiou, V. Yeh, and C.K. Zarins. Magnitude and direction of pulsatile displacement forces acting on thoracic aortic endografts. *Journal of Endovascular Therapy.*, 16(3):350–358, 2009.

[17] L Formaggia, JF Gerbeau, F Nobile, and A Quarteroni. On the coupling of 3d and 1d navier-stokes equations for flow problems in compliant vessels. *Computer Methods in Applied Mechanics and Engineering*, 191(6-7):561–582, 2001.

[18] L. Formaggia, J.F. Gerbeau, F. Nobile, and A. Quarteroni. Numerical treatment of defective boundary conditions for the Navier-Stokes equations. *SIAM Journal on Numerical Analysis*, 40:376–401, 2002.

[19] L Formaggia, D Lamponi, and A Quarteroni. One-dimensional models for blood flow in arteries. *J Eng Math*, 47(3-4):251–276, 2003.

[20] M.H. Friedman, G. M. Hutchins, C. B. Bargeron, O.J. Daters, and F. F. Mark. Correlation between intimal thickness and fluid shear in human arteries. *Atherosclerosis*, 39:425–436, 1981.

[21] S. W. Galt, R.M. Zwolak, R.J. Wagner, and J.J. Gilbertson. Differential response of arteries and vein grafts to blood flow reduction. *Journal of Vascular Surgery*, 17:563–570, 1993.

[22] F J H Gijsen, E Allanic, F N Van de Vosse, and J D Janssen. The influence of the non-Newtonian properties of blood on the flow in large arteries: unsteady flow in a 90 ° curved tube. *Journal of Biomechanics*, 32(7):705–713, July 1999.

[23] T J Gundert, A L Marsden, Weiguang Yang, D S Marks, and J F LaDisa. Identification of Hemodynamically Optimal Coronary Stent Designs Based on Vessel Caliber. *Biomedical Engineering, IEEE Transactions on Biomedical Engineering*, 59(7), 2012.

[24] T.J. Gundert, A.L. Marsden, W. Yang, and J.F. LaDisa. Optimization of cardiovascular stent design using computational fluid dynamics. *Journal of Biomechanical Engineering, Transactions of the ASME.*, 134(1), 2012.

[25] Robert H Haynes and Alan C Burton. Role of the non-Newtonian behavior of blood in hemodynamics. *American Journal of Physiology*, 197:943–950, 1959.

[26] T.J.R. Hughes and J. Lubliner. On the 1 dimensional theory of blood flow in the larger vessels. *Mathematical Biosciences*, 18:161–170, 1973.

[27] JD Humphrey. Vascular adaptation and mechanical homeostasis at tissue, cellular, and sub-cellular levels. *Cell biochemistry and biophysics*, 50(2):53–78, 2008.

[28] Y. Huo and G.S. Kassab. A hybrid one-dimensional/womersley model of pulsatile blood flow in the entire coronary arterial tree. *Am J Physiol Heart Circ Physiol*, 291:H2623H2633, 2007.

[29] M. Ismail, V. Gravemeier, A. Comerford, and W.A. Wall. A stable approach for coupling multidimensional cardiovascular and pulmonary networks based on a novel pressure-flow rate or pressure-only neumann boundary condition formulation. *International Journal for Numerical Methods in Biomedical Engineering*, 30(4):447–469, 2013.

[30] J. E. Moore Jr, C. Xu, S. Glagov, C. K. Zarins, and D. N. Ku. Fluid wall shear stress measurements in a model of the human abdominal aorta: oscillatory behavior and relationship to atherosclerosis. *Atherosclerosis*, 110:225–240, 1994.

[31] J.E. Moore Jr and D. N. Ku. Pulsatile velocity measurements in a model of the human abdominal aorta under resting conditions. *Journal of Biomechanical Engineering*, 116:337–346, 1994.

[32] A. Kamiya and T. Togawa. Adaptive regulation of wall shear stress to flow change in the canine carotid artery. *American Journal of Physiology*, 239:H14–H21, 1980.

[33] K. Kardong. *Vertebrates: Comparative Anatomy, Function, Evolution.* 2002.

[34] I. Kay. *Introduction to Animal Physiology*. Springer-Verlag, 1998.

[35] H. J. Kim, I. E. Vignon-Clementel, C. A. Figueroa, J. F. LaDisa, K. E. Jansen, J. A. Feinstein, and C. A. Taylor. On Coupling a Lumped Parameter Heart Model and a Three-Dimensional Finite Element Aorta Model. *Ann. Biomed. Eng.*, 37(11):2153–2169, NOV 2009.

[36] H.J. Kim, I.E. Vignon-Clementel, J.S. Coogan, C.A. Figueroa, K.E. Jansen, and C.A. Taylor. Patient-specific modeling of blood flow and pressure in human coronary arteries. *Annals of Biomedical Engineering*, 38(10):3195–3209, 2010.

[37] E.O. Kung, A. Baretta, C. Baker, G. Arbia, G. Biglino, C. Corsini, S. Schievano, I.E. Vignon-Clementel, G. Dubini, G. Pennati, et al. Predictive modeling of the virtual hemi-fontan operation for second stage single ventricle palliation: Two patient-specific cases. *Journal of Biomechanics*, 46(2):423–429, 2013.

[38] E.O. Kung, A.L. Les, C.A. Figueroa, F. Medina, K. Arcaute, R.B. Wicker, M.V. McConnell, and C.A. Taylor. In vitro validation of finite element analysis of blood flow in deformable models. *Annals of Biomedical Engineering*, 39(7):1947–1960, 2011.

[39] A.P. Kuprat, S. Kabilan, J.P. Carson, R.A. Corley, and D.R. Einstein. A bidirectional coupling procedure applied to multiscale respiratory modeling. *Journal of Computational Physics*, 244:148–167, 2013.

[40] J. F. LaDisa, Jr., L.E. Olson, I. Guler, D.A. Hettrick, S.H. Audi, J.R. Kersten, D.C. Warltier, and P.S. Pagel. Stent design properties and deployment ratio influence indices of wall shear stress: a 3d computational fluid dynamics investigation within a normal artery. *J Appl Physiol*, 97(1):424–430, 2004.

[41] J. F. LaDisa, Jr., L.E. Olson, R.C. Molthen, D.A. Hettrick, M.D. Hardel, P.F. Pratt, J.R. Kersten, D.C. Warltier, and P.S. Pagel. Alterations in wall shear stress predict sites of neointimal hyperplasia after stent implantation in rabbit iliac arteries. *Am J Physiol Heart Circ Physiol*, 288(5):H2465–75, 2005.

[42] K. Lagana, G. Dubini, F. Migliavacca, R. Pietrabissa, G. Pennati, A. Veneziani, and A. Quarteroni. Multiscale modelling as a tool to prescribe realistic boundary conditions for the study of surgical procedures. *Biorheology*, 39:359–364, 2002.

[43] J.S. Leiva, P.J. Blanco, and G.C. Buscaglia. Iterative strong coupling of dimensionally-heterogeneous models. *Int J Num Meth Engng*, 81(12):1558–1580, 2010.

[44] A.S. Les, S.C. Shadden, C.A. Figueroa, J.M. Park, M.M. Tedesco, R.J. Herfkens, R.L. Dalman, and C.A. Taylor. Quantification of hemodynamics in abdominal aortic aneurysms during rest and exercise using magnetic resonance imaging and computational fluid dynamics. *Annals of Biomedical Engineering*, 38(4):1288–1313, 2010.

[45] M.R. De Leval, G. Dubini, et al. Use of computational fluid dynamics in the design of surgical procedures: application to the study of competitive flows in cavopulmonary connections. *The Journal of Thoracic and Cardiovascular Surgery*, 111(3):502–513, 1996.

[46] S.Q. Liu and Y.C. Fung. Relationship between hypertension, hypertrophy, and opening angle of zero-stress state of arteries following aortic constriction. *Journal of Biomechanical Engineering*, 111:325–335, 1989.

[47] C.C. Long, A.L. Marsden, and Y. Bazilevs. Fluid–structure interaction simulation of pulsatile ventricular assist devices. *Computational Mechanics*, 2013. DOI:10.1007/s00466-013-0858-3.

[48] Anna Lonyai, Anne M Dubin, Jeffrey A Feinstein, Charles A Taylor, and Shawn C Shadden. New insights into pacemaker lead-induced venous occlusion: simulation-based investigation of alterations in venous biomechanics. *Cardiovascular Engineering*, 10(2):84–90, 2010.

[49] A. L. Marsden, A. J. Bernstein, V. M. Reddy, S. Shadden, R. L. Spilker, F. P. Chan, C. A. Taylor, and J. A. Feinstein. Evaluation of a novel Y-shaped extracardiac Fontan baffle using computational fluid dynamics. *Journal of Thoracic and Cardiovascular Surgery.*, 137:394–403, 2009.

[50] F. Migliavacca, G. Dubini, E. L. Bove, and M. R. de Leval. Computational fluid dynamics simulations in realistic 3-D geometries of the total

cavopulmonary anastomosis: the influence of the inferior caval anastomosis. *J. Biomech. Eng.*, 125:805–813, 2003.

[51] M. Esmaily Moghadam, I.E. Vignon-Clementel, R. Figliola, and A.L. Marsden. A modular numerical method for implicit 0d/3d coupling in cardiovascular finite element simulations. *Journal of Computational Physics*, 244(1):63–79, 2013.

[52] C. D. Murray. The physiological principle of minimum work. I. the vascular system and the cost of blood volume. *P. Natl. Acad. Sci. USA*, 12:207–214, 1926.

[53] R. Nakazato, H.-B. Park, D. S. Berman, H. Gransar, B.-K. Koo, A. Erglis, F. Y. Lin, A. M. Dunning, M. J. Budoff, J. Malpeso, J. Leipsic, and J. K. Min. Fractional flow reserved derived from computed tomographic angiography (FFRCT) for intermediate severity coronary lesions: Results from the DeFACTO trial (determination of fractional flow reserve by anatomic computed tomographic angiography). *Journal of the American College of Cardiology.*, 60(17):B6–B6, 2012.

[54] M.S. Olufsen. Structured tree outflow condition for blood flow in larger systemic arteries. *Am J Physiol.*, 276(1):257–68, 1999.

[55] Charles S Peskin. Numerical analysis of blood flow in the heart. *Journal of computational physics*, 25(3):220–252, November 1977.

[56] A. Quarteroni, S. Ragni, and A. Veneziani. Coupling between lumped and distributed models for blood flow problems. *Computing and Visualization in Science*, 4:111–124, 2001.

[57] R. Ross. Atherosclerosis–an inflammatory disease. *New England Journal of Medicine*, 340:115–126, 1999.

[58] S. Sankaran, M.E. Moghadam, A.M. Kahn, E.E. Tseng, J. Guccione, and A.L. Marsden. Patient-specific multiscale modeling of blood flow for coronary artery bypass graft surgery. *Annals of Biomedical Engineering*, 40(10):2228–2242, 2012.

[59] P. Segers, F. Dubois, D. De Wachter, and P. Verdonck. Role and relevancy of a cardiovascular simulator. *J. Cardiovascular Engineering*, 3:48–56, 1998.

[60] D. Sengupta, A.M. Kahn, J.C. Burns, S. Sankaran, S.C. Shadden, and A.L. Marsden. Image-based modeling of hemodynamics and coronary artery aneurysms caused by Kawasaki disease. *Biomechanics and Modeling in Mechanobiology*, 11(6):915–932, 2012.

[61] N. Stergiopulos, D.F. Young, and T.R. Rogge. Computer simulation of arterial flow with applications to arterial and aortic stenosis. *J. Biomechanics*, 25:1477–1488, 1992.

[62] C. A. Taylor, C. P. Cheng, L. A. Espinosa, B. T. Tang, D. Parker, and R. J. Herfkens. In vivo quantification of blood flow and wall shear stress in the human abdominal aorta during lower limb exercise. *Ann. Biomed. Eng.*, pages 402–408, 2002.

[63] C. A. Taylor, T. J. R. Hughes, and C. K. Zarins. Finite element modeling of blood flow in arteries. *Comput. Meth. Appl. Mech. Engrg.*, 158:155–196, 1998.

[64] S.A. Urquiza, P.J. Blanco, M.J. Venere, and R.A. Feijoo. Multidimensional modelling for the carotid artery blood flow. *Computer Methods in Applied Mechanics and Engineering*, 195(33-36):4002–4017, 2006.

[65] A Valentín and J D Humphrey. Evaluation of fundamental hypotheses underlying constrained mixture models of arterial growth and remodelling. *Philosophical Transactions of the Royal Society A: Mathematical, Physical and Engineering Sciences*, 367(1902):3585–3606, August 2009.

[66] I. E. Vignon-Clementel, C. A. Figueroa, K. E. Jansen, and C. A. Taylor. Outflow boundary conditions for three-dimensional finite element modeling of blood flow and pressure in arteries. *Comput. Meth. Appl. Mech. Engrg.*, 195:3776–3796, 2006.

[67] I.E. Vignon-Clementel, C.A. Figueroa, K.E. Jansen, and C.A. Taylor. Outflow boundary conditions for three-dimensional simulations of non-periodic blood flow and pressure fields in deformable arteries. *Computer Methods in Biomechanics and Biomedical Engineering*, 13(5):625–640, 2010.

[68] M. Vukicevic, J. A. Chiulli, T. Conover, G. Pennati, T. Y. Hsia, and R. S. Figliola. Mock circulatory system of the fontan circulation to study

respiration effects on venous flow behavior. *Comput. Meth. Appl. Mech. Engrg.*, 59(3):253–60, 2013.

[69] N. Westerhof, F. Bosman, C. J. De Vries, and A. Noordergraaf. Analog studies of the human systemic arterial tree. *J. Biomech.*, 2:121–43, 1969.

[70] N. Westerhof, J. Lankhaar, and B. E. Westerhof. The arterial windkessel. *Med Biol Eng Comput*, 47(2):131–41, 2009.

[71] J. Womersley. An elastic tube theory of pulse transmission and oscillatory flow in mammalian arteries. Air research and development command, united states air force, Wright Air Development Center, Wright-Patterson Air Force Base, Ohio, 1957.

[72] G. Xiong, C.A. Figueroa, N. Xiao, and C.A. Taylor. Simulation of blood flow in deformable vessels using subject–specific geometry and spatially varying wall properties. *International Journal for Numerical Methods in Biomedical Engineering*, 27(7):1000–1016, 2011.

[73] C.K. Zarins, D.P. Giddens, B.K. Bharadvaj, V.S. Sottiurai, R.F. Mabon, and S. Glagov. Carotid bifurcation atherosclerosis. quantitative correlation of plaque localization with flow velocity profiles and wall shear stress. *Circulation Research*, 53(4):502–514, 1983.

[74] C.K. Zarins, M.A. Zatina, D. P. Giddens, D. N. Ku, and S. Glagov. Shear stress regulation of artery lumen diameter in experimental atherogenesis. *Journal of Vascular Surgery*, 5:413–420, 1987.